Numerical study of flow around bypass pigs

Xiaoyun Liang

Master of Science Thesis

TU Delft Delft University of Technology

Challenge the future

NUMERICAL STUDY OF FLOW AROUND BYPASS PIGS

by

Xiaoyun Liang

in partial fulfillment of the requirements for the degree of

Master of Science
in Mechanical Engineering

at the Delft University of Technology,
to be defended publicly on Tuesday November 17, 2015 at 14:00 PM.

Student number:	4328884
P & E report number:	2702
Supervisors:	Prof. Dr. Ir. R. A. W. M. Henkes
	Dr. Ir. W.-P. Breugem
	Ir. M. H. W. Hendrix
External Reviewer:	Dr. S. Kenjeres

TU Delft Delft University of Technology

ABSTRACT

In the oil and gas industry, pipeline networks are used to transport the production fluids from wells to production plants. During normal operation, the pipelines need regular cleaning and inspection. Typically, the pipeline maintenance is performed by pigging, which refers to using devices known as “pigs ”(Pipeline Inspection Gauges) to perform various maintenance operations of the pipeline.

In order to describe the motion of the pig in the pipeline, detailed understanding of the flow around the pig is required. In this research, a CFD (computational fluid dynamics) approach was applied to model fully turbulent flow ($Re \approx 10^7$) around various types of bypass pigs. We especially focused on the relation between the overall pressure drop, which was represented by a dimensionless pressure loss coefficient, and various dimensionless parameters describing the flow and the configuration. The pressure loss coefficient is caused by the fluid that passes through the bypass area. If the pressure loss coefficient is known, together with the friction between the moving pig and the pipe wall, the motion of the pig can be described. Moreover, often the flow in the pipeline is in multiphase (stratified flow) condition. Therefore, in this research the effect of multiphase flow around a bypass pig was also investigated.

For the single phase study, two types of bypass pigs were investigated: the disk pig and the complex bypass pig. The disk pig has a fixed and relatively simple geometry, and it is based on the conventional bypass pig, with a deflector plate in front of the pig body. The complex bypass pig geometry is based on the disk pig, though now the bypass area is created by holes which can be adjusted. In reality, for these complex bypass pigs, the bypass pig velocity is controlled by adjusting the bypass area.

For the conventional bypass pig, previous studies have shown that the Idelchik’s correlation for thick orifices can predict the pressure loss coefficient accurately. Thus a similar approach was applied in the disk pig study in order to obtain a theoretical correlation to predict the pressure loss coefficient for the disk pig. Indeed such a correlation was found which gives an accurate prediction for a certain parameter regime. In the complex bypass pig study, we mainly focused on the influence of the bypass area fraction on the pressure loss coefficient. Two correlations based on two approaches were suggested. It was found that these correlations can predict the overall pressure drop across the complex bypass pig accurately, especially when the opening fraction of the bypass adjusting holes was relatively large.

Furthermore, for the multiphase study, the simpler pig models were investigated. First of all, the flow in front of a pig without bypass region was investigated. One of the practical purposes of this study is that we want to investigate under which condition the full pipeline perimeter gets wetted with liquid. This is important for the distribution of corrosion inhibitors. Moreover, the multiphase flow around a (conventional) bypass pig was investigated, to obtain a better understanding of the multiphase flow behaviour for bypass pigs.

ACKNOWLEDGEMENTS

It is a great pleasure to acknowledge my deepest thanks and gratitude to Professor Ruud Henkes, for providing me this research opportunity, and for his kind supervision. It was a great honour to work under his supervision.

I also would like to express my deepest thanks and sincere appreciation to Dr. Wim-Paul Breugem, for his encouragement, as well as for comprehensive and creative advice during this research.

Furthermore I would like to express my extreme sincere gratitude and appreciation to Ir. Maurice Hendrix, for his kind endless help, and for his generous advice and support during this research.

I appreciate the time all three of my supervisors spent on reading and correcting the drafts of my thesis. Additionally, I would like to thank Dr. Sasa Kenjeres, for agreeing to join my graduation committee and for taking time to read my thesis.

I also would like to thank Dr. Mathieu Pourquie for his kindly help during this research.

It is regrettable that I only had nine months to work in the Laboratory of Aero & Hydrodynamics, but I will never forget this experience.

Finally, I would like to thank my parents, my family members and my friends. For me, it was not possible to finish my study program in TU Delft without their love and supports. This thesis is my best gift to them.

Xiaoyun Liang
Delft, November 2015

CONTENTS

List of Figures

List of Tables

LIST OF NOMENCLATURE

English notations:

Symbol	Units	Description
C_{tp}	–	Total pressure coefficient
C_{μ}	–	Constant used in the $k-\epsilon$ turbulence model
D	m	Diameter of the pipe
d	m	Diameter of the narrow pipe
El	–	Dimensionless entrance length
F	m^2	Area
H	m	Height of the disk
H_i	m	Diameter of the inner wall of the holes
h	m	Distance between the pig and the disk
I	–	Turbulence intensity
K	–	Pressure loss coefficient
k	m^2/s^2	Turbulent kinetic energy
L	m	Characteristic length
l	m	Length
m	kg	Mass
n	–	Number of opening holes
P	Pa	Pressure
P_t	Pa	Total pressure
Re	–	Reynolds number
r	m	Radius
t	m	Thickness of the disk
U	m/s	Mean velocity
U^+	–	Velocity in non-dimensional wall units
u	m/s	Velocity
u_τ	m/s	Friction velocity
u'	m/s	RMS of the fluctuating velocities
V	m/s	Average velocity
y	m	Distance from the pipe wall
$y+$	–	Distance from a wall in non-dimensional wall units
z	m	Distance in the x direction

Greek notations:

Symbol	**Units**	**Description**
α	–	volume fraction
δ_{ij}	–	Kronecker delta
ϵ	m^2/s^3	Turbulent kinetic energy dissipation rate
κ	–	Von Karman constant
ω	$^\circ$	Angle of opening holes
μ	kg/ms	Dynamic viscosity
ν	m^2/s	Kinematic viscosity
Π	–	Dimensionless parameters in the Buckingham Pi theorem
ρ	kg/m^3	Density
τ_w	kg/ms^2	Wall shear stress

1

INTRODUCTION

1.1. BACKGROUND

In the oil and gas industry, the production fluids are transported from wells to production plants by pipeline networks. As the wells are located in different positions, the pipelines could span an extremely long distance, for instance hundreds of kilometres. The pipelines need regular cleaning and inspection during normal operation, and ideally, these processes should interrupt the production flow as little as possible.

Typically, pipeline maintenance is performed by pigging, which refers to using devices known as "pigs" (Pipeline Inspection Gauge) to perform various maintenance operations of the pipeline. The pigging is accomplished by putting the pig into a pig launcher, which is an oversized section in the pipeline, reducing to the normal diameter. Then the launcher is closed and the production flow is used to push the pig along the downstream pipe, until it reaches the receiving station. One of the advantages of this approach is that the production is not interrupted when the maintenance operation is in process.

As the pig is driven by the fluids in the pipeline, and if the fluids cannot pass through the pig, it will move with the same velocity as the fluid for single phase flow and with the mixture velocity of the fluids for multiphase flow. However, ideally the pig should not move too fast. The pipeline cleaning and dewartering is most effective if the cleaning pig is moving at a velocity below 5 m/s [2]. Also, if the pig moves with a very high velocity, it could cause damage to the pipeline, or to the pig itself. In order to mitigate these risks, we could decrease the fluids' velocity; however, it means the production rate also has to be turned down. This situation can be improved by using bypass pigs. Figure 1.1 shows an example of a bypass pig. This bypass pig has an opening in the middle, through which the fluids can bypass the pig. Thus, the pig velocity can be decreased by adding a bypass region, without turning down the production rate.

Figure 1.1 shows a relatively simple bypass pig, which has a cylindrical hole in the middle, and the hole is oriented along the axis of the pig. Also, there are several different types of bypass pigs, and some of them have a very complex shape. Figure 1.2 shows two different types of bypass pigs.

Figure 1.1: An example of a bypass pig: conventional bypass pig, reproduced from [3]

(a) Intelligent pig, reproduced from [4]

(b) Cleaning pig, reproduced from [2]

Figure 1.2: Different types of bypass pigs

In general, there are two main purposes for pigs: inspection and pipeline cleaning.

- The intelligent pig is used for inspection of the pipelines[5]. Figure 1.2a shows an example of an intelligent pig. The inspection is performed by inserting the intelligent pig in the pipeline, and there are electronics and sensors inside of the intelligent pig. Thus, different types of data can be collected when the intelligent pig is moving inside the pipeline[4]. The intelligent pig has relatively complex geometry, as it contains the built-in equipment for collecting data.

- Pipeline cleaning is performed by another type of pig: the cleaning pig, which belongs to the utility pigs. Figure 1.2b shows an example of a cleaning pig. The purpose of the pipeline cleaning operation depends on the fluids' condition in the pipeline system. For oil dominated pipe flow, the wax formed on the pipe wall is the primary issue for the pipeline cleaning operation. The wax formed on the pipe wall can obstruct flow through the pipeline, thus reduce the transport efficiency. The wax deposits could be removed through pigging. However, the formation of wax plug in front of the pig could decrease the velocity of the pig, or even stall it completely[6]. This problem can be solved by introducing the bypass pig, as the wax can be removed by the fluids which pass through the bypass region[7]. On the other hand, for the gas phase dominated multiphase flow condition, the development of slugs of liquid in the lower region of pipe is the most common problem people faced. This situation can be improved through pigging, as the pig drives the liquid slug to the end of the pipeline, where it is received by a slug catcher[8]. In order to prevent the pipeline corrosion problem, the pipeline's internal wall can be protected by a protective layer, which is formed by corrosion inhibitors. In order to distribute the corrosion inhibitors on the internal wall of the pipeline, cleaning pigs

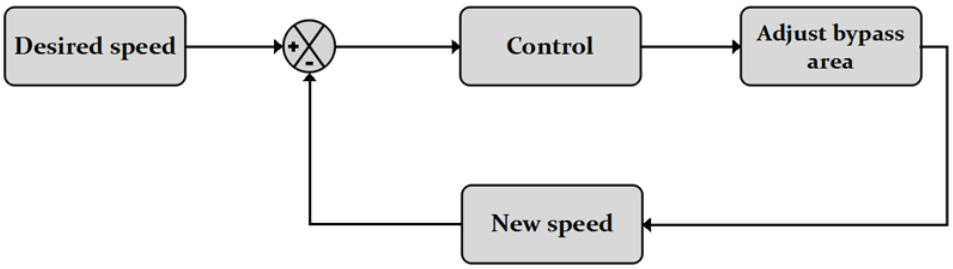

Figure 1.3: Schematic of the pig velocity close loop control system, reproduced from [2]

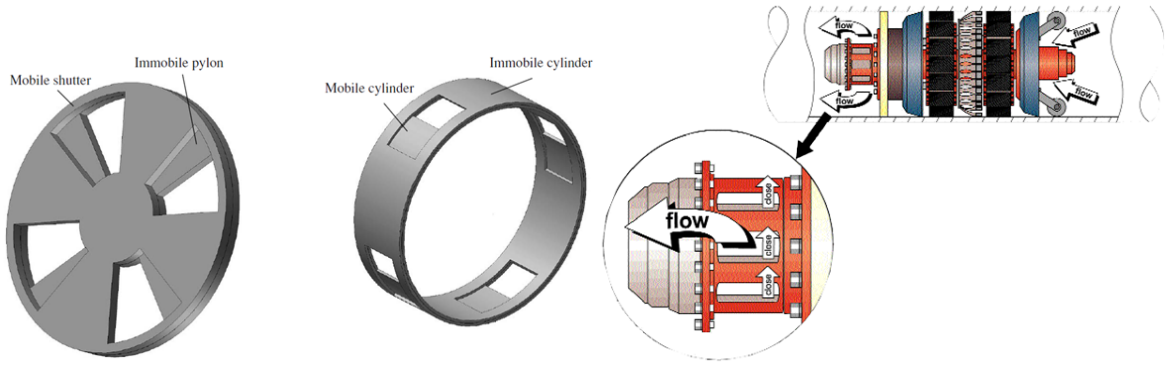

(a) Bypass control devices, reproduced from [2]

(b) A bypass pig with the bypass adjusting device, made by the Rosen group, reproduced from [12]

Figure 1.4: Bypass control devices and an example of a bypass pig with the bypass adjusting device

should be used to remove the sediment and sweep out water from the wall of the pipeline. Then, a film of inhibitor can be applied on the pipe wall by using the sealing pig, which is another type of the utility pigs[9]. When the stratified flow (multiphase condition) exists in the pipeline, sometimes the corrosion inhibitor cannot contact the top of the pipe wall, and leaving a part of the pipeline unprotected. For instance, for a pipeline in which the fluids are in liquid-gas flow condition, and the corrosion inhibitor is contained by the liquid phase flow. Due to the gravity, sometimes the liquid phase flow cannot contact the top of the pipe wall, thus the corrosion inhibitor cannot be applied to the top region of the pipeline.

The bypass pig was introduced to mitigate the risks caused by a too high pig velocity. However, if the bypass area is fixed, the pig velocity still cannot be adjusted during the pigging operation. In recent years the development of pigs with speed control technology has gained popularity[10]. Figure 1.3 shows the schematic of the pig velocity control system. The velocity of pig can be controlled by adjusting the bypass area, in order to achieve desired velocity[11]. Figure 1.4a shows two types of the typical bypass adjusting devices, and the bypass area can be adjusted by using the battery-powered electric motor. Figure 1.4b shows an example of a bypass pig with speed control technology made by the Rosen group[12]. In this “Rosen pig”, there is a bypass adjusting device after the horizontal bypass region, and the velocity of pig can be controlled by adjusting the additional bypass regions (closing and opening the bypass adjusting holes).

1.2. MOTIVATION

The first pigging operation took place in around the year of 1870, a few years after Colonel Drake discovered oil in Titusville, Pennsylvania, with the development of the oil and gas industry, the pigging operation became a standard industrial practice[13]. From the 1980s, the scientific community started to study flow around pigs, by both experiments and simulations approaches[14][15]. In recent years, the research in speed control technology for pigs has been interested in particularly[10]. The schematic of the pig velocity control system and the typical bypass adjusting devices are shown in Figure 1.3 and 1.4a.

The general equation to describe the pig motion can be expressed as:

$$m\frac{du_{pig}}{dt} = \Delta P \cdot F_{cross} + \sum_i f_i \tag{1.1}$$

Where m represents the mass of the pig, u_{pig} is the pig velocity and F_{cross} is the cross section area of the pipe. In Equation 1.1, $\frac{du_{pig}}{dt}$ represents the acceleration of the pig and f_i represents the forces acting on the pig, i.e. the friction due to the pipe wall, and gravity, if the pipeline is under inclination; ΔP represents the overall pressure drop, which is the driving force of pig's movement. The pressure drop in the bypass pig can be linked with the velocity of flow by the following expression:

$$\Delta P = \frac{1}{2}\rho u_{bypass}^2 \cdot K \tag{1.2}$$

Where ρ represents the density of fluid, u_{bypass} represents the average velocity of flow in the bypass region and K represents the pressure loss coefficient, which will be introduced in Section 2.4.1.

Thus, if the coefficient K is known, the overall pressure drop of the bypass pig can be calculated by Equation 1.2, as the flow velocity in the bypass region u_{bypass} is dependent on the bypass pig geometry and the flow condition in the pipeline. Furthermore, the motion of the bypass pig can be described through Equation 1.1. Thus, for the pig velocity control technology, detailed understanding of the flow's behaviour around the bypass pigs, especially the relationship between the pressure loss coefficient K and the bypass pigs geometry, is critical.

In this research field, the most common numerical approach is using one dimensional models to study the interaction of the multiphase flow with the pig geometry in the pipeline. The pig dynamics are modelled by the differential equations system which are coupled by the overall pressure drop, which is the driving force of the pig's movement, to the flow equations[16]. In the oil and gas industry, the pipeline could span hundreds of kilometres, which makes the one dimensional models much more appropriate than the two or three dimensional models[17].

Another approach is to study the detailed flow behaviour around the bypass pigs[18][19] by a numerical model. This can be used to find a relation between the driving force of the bypass pigs and the governing parameters of the pigs. Furthermore, by using the numerical models (in two dimensions or even three dimensions) the flow behaviour around the bypass pigs can be studied in detail.

For the motion of the pig in a pipeline, the pressure drop across the pigs cannot be predicted accurately by the one dimensional model accurately. Thus, the CFD (computational fluid dynamics) approach can be applied for the numerical modelling of the flow around the pigs. In recent years

Figure 1.5: Disk pig, reproduced from [8]

the commercial CFD packages have become more and more popular in both research field and industry[20]. The CFD approach has several advantages[21]:

- The CFD approach is based on the numerical methods and schemes. By taking advantage of the development of the understanding of the fluid dynamics theories, especially the development of the understanding of turbulence and other complex flow behaviours, the CFD approach can be applied in various fields, and reliable solutions can be achieved. On the other hand, with the development of the computer's computing ability in recent years, first of all the costs of CFD have become lower and lower; moreover, much bigger numerical simulations can be concluded.

- The costs of numerical simulations are much less than of experiments. Also, CFD can be used in some extreme conditions, which is not available for the experimental approach due to the safety risks.

- By using CFD, the detailed flow behaviour in a certain condition can be investigated, which is not easily obtainable in an experimental approach.

In fact the flow around the bypass pigs has already been studied by using the commercial CFD package ANSYS Fluent[18][19], and these studies provide a suitable starting point for further works. The details of the investigation of bypass pigs by using CFD will be introduced in Section 1.3.

1.3. PREVIOUS STUDIES

The flow around the bypass pigs has already been studied before by the CFD approach.

Singh and Henkes[18] studied a simple bypass pig model for both single phase and two phases flow, by using the commercial CFD software ANSYS Fluent. It was found that with high Reynolds number the pressure loss coefficient was in agreement with the Idelchik's[22] correlation for a thick orifice. Furthermore, in this research the multiphase flow around the bypass pigs was studied by a two dimensional planar CFD model.

Additionally, Korban[19] studied the flow around more complex bypass pigs in single phase condition by using ANSYS Fluent (version 14.5). Two dimensional axisymmetric CFD models were used

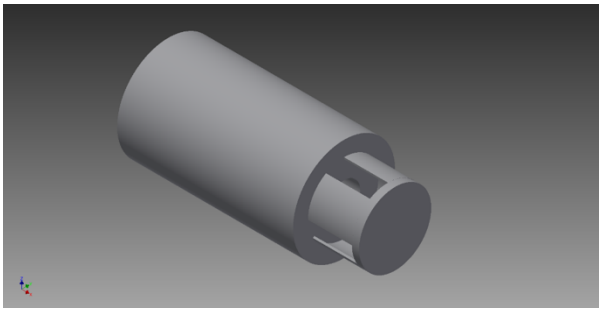

Figure 1.6: Complex bypass pig model built by CAD software

to study the flow around two types of bypass pigs, which are used in the oil and gas industry, the conventional bypass pig and the disk pig. The geometry of the conventional bypass pig is shown in Figure 1.1, and the geometry of the disk pig is shown in Figure 1.5. The detailed flow behaviour around bypass pigs was investigated. Moreover, different parameter studies were carried out, in order to study the relationship between the overall pressure loss coefficient K and the governing parameters of the bypass pigs. The numerical setup of the CFD models for the flow around bypass pigs has been defined and validated in that research, which is used as input to the present research.

1.4. OBJECTIVES

This thesis aims to achieve better fundamental understanding of the flow around various types of bypass pigs by the CFD approach.

First of all, the flow around the disk pig has been studied by Korban [19], however, some physics behind the flow around the disk pig are still unclear. More importantly, the correlation to calculate the pressure loss coefficient K for the disk pig is not given in that research. Thus, the flow around the disk pig is further investigated in the present research.

Moreover, flow around the bypass pigs with more complex geometry is studied in the present research. One of the biggest challenges to study the bypass pigs with more complex geometry is, when the bypass pig geometry is not axisymmetric; this means that the two dimensional axisymmetric CFD approach is not available any more, but instead three dimensional CFD simulations are required. In this research, the complex bypass pig that contains the adjustable bypass area device is studied. Figure 1.6 shows the complex bypass pig model built by the CAD software, it actually represents the “Rosen pig”as shown in Figure 1.4b.

For the single phase study of the bypass pigs, we are interested in the detailed flow behaviour around the bypass pigs. Also, one of the most important variables in the single phase study is the overall pressure drop, which is the driving force of the motion of the pig in the pipeline. Thus, in this research, we especially focus on investigating of the relation between the pressure loss coefficient K (and the overall pressure drop) and the governing parameters of the bypass pigs.

On the other hand, in the oil and gas industry, the flow condition in the pipelines is not always in single phase, but it can also be in two phases (liquid and gas). Thus, in this research flow around the bypass pigs in multiphase condition is investigated. In order to capture the two phases interaction, a full three dimensional CFD model is required.

In the multiphase study, the variables that we are interested in are slightly different to the variables in the single phase study. For instance, the volume fraction of the liquid (or gas) phase flow is one of the most important variables in the multiphase study. For a practical purpose, for example, we would like to study the condition when the liquid phase contacts the top of the pipe wall, as this guarantees that the corrosion inhibitor is distributed across to full perimeter of the pipe wall.

Compared with two dimensional CFD simulations used by Singh and Henkes[18] and Korban[19], the three dimensional CFD simulations require much larger computational resources and longer computing times.

1.5. THESIS STRUCTURE

This thesis is organized as follows:

In Chapter 2, the relevant theoretical background of this thesis is introduced. The numerical setup of the CFD model is described in Chapter 3. The validations of the numerical models and the modelling approaches used in the numerical setup are dealt with in Chapter 4.

The results from numerical simulations that have been performed are presented in Chapter 5, 6 and 7. In Chapter 5, the results of the disk pig study are presented; In Chapter 6, the results of complex bypass pigs with bypass adjusting device are presented; Furthermore, the results of the multiphase study are discussed in Chapter 7.

Finally, the conclusions and recommendations for future research are given in Chapter 8.

2

THEORETICAL BACKGROUND

In this chapter, some theories relevant to this research are presented. First of all, the governing equations of the numerical model are introduced. Furthermore, dimensional analysis is performed to derive the dimensionless groups of the bypass pigs numerical model. After this, theory related to the fully developed pipe flow is presented. Finally, correlations in order to calculate the pressure loss coefficient K in various geometries related to the bypass pigs geometry are discussed, and these theoretical correlations will be used to compare with the results from bypass pigs CFD models in this research.

2.1. GOVERNING EQUATIONS

The bypass pig CFD model involved in this research is a numerical system, which is governed by different flow equations. The governing equations of the CFD numerical model are introduced in this section.

2.1.1. NAVIER-STOKES EQUATIONS

We first introduce one of the most famous equations in fluid mechanics, the Navier-Stokes equations. The Navier-Stokes equations are the governing equations of the viscous fluid substances' motion, and they come from applying Newton's second law to fluid motion, thus describing the changes of the flow momentum in space and time[23]. For incompressible Newtonian fluids, the general Navier-Stokes equations can be expressed as:

$$\rho\left(\frac{\partial u}{\partial t} + u \cdot \nabla u\right) = -\nabla P + \mu \nabla^2 u + f \tag{2.1}$$

where ρ denotes the density of the fluid; u is the velocity vector, in three dimensional fluids, it represents three velocities in the x, y and z direction (u, v and w); P is the pressure of the fluid; μ is the viscosity of the fluid and f represents the body forces acting on the fluid, for instance gravity.

In Equation 2.1, the left hand side represents the inertial effects. The first term represents the time dependent effects, the second term represents the convective acceleration. On the right hand

side, the first two terms represent the internal influence of the fluid, ∇P is the pressure gradient and the second term represents the diffusion of momentum. The third term represents external forces.

Furthermore, for incompressible fluids, the so called continuity equation, which comes from mass conservation in the system, can be expressed as:

$$\nabla \cdot u = 0 \tag{2.2}$$

Equation 2.2 states that for a control volume in the fluid, the inflow has to be equal to the outflow.

Thus, the motion of fluid is described by the four differential equations. However, due to the complexity of the Navier-Stokes equations (Equation 2.1), analytical solutions are only available for the relatively simpler systems. In the practical conditions, the equations are always solved by taking a numerical approach, and only approximate solutions can be obtained.

2.1.2. REYNOLDS NUMBER

In fluid mechanics, the Reynolds number Re is a dimensionless number which is used to predict similar flow patterns in different flow situations. The Reynolds number is calculated by the ratio of the inertial force and the viscous force, and can be expressed as:

$$Re = \rho UL/\mu = UL/\upsilon \tag{2.3}$$

Where U represents the mean velocity of the object relative to the fluid, L is a characteristic linear dimension and $\upsilon = \mu/\rho$ is the kinematic viscosity.

For the fully developed pipe flow, turbulent flow occurs when the Reynolds number is larger than 4000, laminar flow occurs when the Reynolds number is smaller than 2100. In the range between 2300 and 4000, the flow is called transition flow, in which both turbulent and laminar flow are possible.

In this research, the typical pipe flow velocity is around 3 m/s, pipe diameter is around 1 m and kinetic viscosity is 3 E-7 m^2/s. Thus, based on Equation 2.3, we can calculate the typical Reynolds number is around 1 E+7, which indicates that the flow is strongly turbulent.

2.1.3. THE RANS EQUATIONS

For simulating turbulence, most of the computational approaches use three different methods:

- DNS: Direct Numerical Simulations
- LES: Large Eddy Simulations
- the RANS (Reynolds-averaged Navier-Stokes) models.

Each of these methods has its advantages and disadvantages. For the DNS approach, the Navier-Stokes equations are explicitly solved without any turbulence model, and all of the spatial and temporal scales of the turbulence are resolved. Thus, the DNS is the most accurate approach, but the computational costs is very high, and it can only be applied for relatively low Reynolds number and simple geometries. For the LES approach, the large turbulent motions are solved and the small scale motions are modelled. The idea behind LES is to reduce the computational cost by reducing the

range of length and time scales which are being solved, by a low pass filtering of the Navier-Stokes equations.

On the other hand, the RANS approach is popular in industry, as it can overcome the limitations of the DNS and LES approaches, by relying on modelling of the whole turbulence behaviour. In this research, the RANS approach is being used.

In order to derive the Navier-Stokes equations to RANS equations, the concept of Reynolds decomposition is introduced here. The Reynolds decomposition is a mathematical method to decompose the solution variables into a time-averaged part and a fluctuating part. For instance, for the velocity component u_i the decomposition can be expressed as

$$u_i = U_i + u_i' \tag{2.4}$$

Where U_i and u_i' represent the mean and fluctuating parts of u_i.

The Navier-Stokes equations (Equation 2.1) are time-averaged to obtain the RANS equations, by applying the Reynolds decomposition. After substituting the Reynolds decomposition (Equation 2.4) for the velocity component u_i in the Navier-Stokes equations (Equation 2.1), the RANS equations for the incompressible Newtonian fluid can be expressed as:

$$\rho(\frac{\partial}{\partial t}(U_i) + \frac{\partial}{\partial x_j}(U_i U_j)) = -\frac{\partial \overline{p}}{\partial x_i} + \mu\frac{\partial^2 U_i}{\partial x_j \partial x_j} + \overline{f_i} - \frac{\partial}{\partial x_j}(\rho\overline{u_i' u_j'}) \tag{2.5}$$

In this equation, the left hand side and the first three terms on the right hand side are with similar form as Equation 2.1. However, after Reynolds-averaging, one additional term appears, which is the last term of Equation 2.5. The term $\frac{\partial}{\partial x_j}(\rho\overline{u_i' u_j'})$ is related to the Reynolds stress τ_R, which is given as:

$$\tau_{R_{ij}} = -\rho\overline{u_i' u_j'} \tag{2.6}$$

With this term, the RANS equations are not closed any more, and additional equations are required to close the numerical system. Typically, this is made by using turbulence models.

2.1.4. THE $k-\epsilon$ TURBULENCE MODEL

The $k-\epsilon$ turbulence model belongs to the two equation turbulence models, which are one of the most common type of turbulence models. The basis of all two equation turbulence models is the Boussinesq eddy viscosity assumption, which postulate that the Reynolds stress tensor is proportional to the mean strain rate tensor, mathematically, it can be expressed as:

$$-\rho\overline{u_i' u_j'} = \mu_t(\frac{\partial U_i}{\partial x_j} + \frac{\partial U_j}{\partial x_i}) - \frac{2}{3}\rho k\delta_{ij} \tag{2.7}$$

Where $k = \frac{1}{2}\overline{u_i' u_i'}$ is the turbulent kinetic energy, μ_t is the turbulent viscosity, and δ_{ij} represents the Kronecker delta.

For the standard $k-\epsilon$ turbulence model, the turbulence kinetic energy k and its dissipation rate ϵ are obtained from the following transport equations:

$$\frac{\partial}{\partial t}(\rho k) + \frac{\partial}{\partial x_i}(\rho k u_i) = \frac{\partial}{\partial x_j}[(\mu + \frac{\mu_t}{\sigma_k})\frac{\partial k}{\partial x_j}] + G_k + G_b - \rho\epsilon - Y_M + S_k \tag{2.8}$$

and

$$\frac{\partial}{\partial t}(\rho\epsilon)+\frac{\partial}{\partial x_i}(\rho\epsilon u_i)=\frac{\partial}{\partial x_j}[(\mu+\frac{\mu_t}{\sigma_\epsilon})\frac{\partial\epsilon}{\partial x_j}]+C_{1\epsilon}\frac{\epsilon}{k}(G_k+C_{3\epsilon}G_b)-C_{2\epsilon}\rho\frac{\epsilon^2}{k}+S_\epsilon \tag{2.9}$$

In these equations, G_k represents the production of turbulence kinetic energy due to the main velocity gradients; G_b is the generation of turbulence kinetic energy due to buoyancy, in this research G_b is ignored as the heat transfer is not considered; Y_M represents the contribution of the fluctuating dilatation in compressible turbulence to the overall dissipation rate, for incompressible fluid this production is ignored. $C_{1\epsilon}$, $C_{2\epsilon}$ and $C_{3\epsilon}$ are constants, σ_k and σ_ϵ are the turbulent Prandtl numbers for k and ϵ, respectively. S_k and S_ϵ are user-defined source terms.

In the $k-\epsilon$ turbulence model, the turbulent production G_k is calculated as:

$$G_k=-\rho\overline{u_i'u_j'}\frac{\partial u_j}{\partial x_i} \tag{2.10}$$

In the $k-\epsilon$ turbulence model, the turbulence viscosity is calculated by k and ϵ as follows:

$$\mu_t=\rho C_\mu\frac{k^2}{\epsilon} \tag{2.11}$$

Where C_μ is a constant.

In Fluent the model constants have the following values[24]:

$$C_{1\epsilon}=1.44,\ C_{2\epsilon}=1.92,\ C_\mu=0.09,\ \sigma_k=1.0 \text{ and } \sigma_\epsilon=1.3$$

2.1.5. MULTIPHASE FLOW MODELLING

In this research, the multiphase flow around a pig is studied. The relevant theories of multiphase flow modelling are introduced in this part.

In fluid mechanics, the multiphase flow is the simultaneours flow of:

- Materials with different states or phases, i.e. solid, liquid or gas.
- Materials with different chemical properties in the same state or phase.

In this research, we consider the multiphase flow consisting of a liquid phase and a gas phase, and no reaction is considered. Thus, in this research we want to simulate the gas-liquid flow by using CFD.

Typically, there are two approaches for the numerical modelling of the multiphase flow:

- The Euler-Lagrange approach: The fluid phase is treated as a continuum by solving the time-averaged Navier-Stokes equations, and the dispersed phase is solved by tracking a large number of bubbles, particles or droplets through the calculated flow field. The dispersed phase can exchange momentum, mass and energy with the fluid phase. This approach is suitable for modelling of several conditions, for instance coal and liquid fuel combustion, spray dryers and some particle-laden flows[24]. However, this approach is not available for modelling of applications in which the volume fraction of the second phase is not negligible, so this approach cannot be used in this research.

- The Euler-Euler approach:The different phases are treated as interpenetrating continua numerically. In this approach, the volume of a phase cannot be occupied by the other phases, and conservation equations for each phase are derived to obtain a set of equations, and for all phases the equations have a similar structure. The equations can be closed by providing constitutive relations[24].

In ANSYS Fluent, three different Euler-Euler multiphase models can be chosen: the volume of fluid (VOF) model, the mixture model and the Eulerian model. Each multiphase model has its suitable applications. For slug flows and stratified/free-surface flow, the VOF model is suggested[24]. Thus, in this research, the VOF (volume of fluid) model is chose for the multiphase modelling.

The VOF model relies on the fact that two phases are not interpenetrating. For each phase which added in the system, a variable is introduced, the volume fraction of the phase in the computational cell. In each control volume, the volume fractions of all phases sum to 1. The n^{th} phase's volume fraction in a cell is denoted as α_n, and there are three possible conditions:

- α_n=0 indicates the cell is empty of the n^{th} phase.
- α_n=1 indicates the cell is full of the n^{th} phase.
- 0<α_n<1 indicates the cell contains the interface between the two phases.

Based on the local value of α_n, the appropriate properties and variables are assigned to each control volume.

For the n^{th} phase, the volume fraction equation can be expressed as:

$$\frac{\partial \alpha_n}{\partial t} + \vec{v} \cdot \nabla \alpha_n = \frac{S_{\alpha_q}}{\rho_n} \tag{2.12}$$

Where $\vec{v}$ represents the phase velocity, ρ_n represents the density of n^{th} phase and S is the source term, which is zero by default. The volume fraction equation is not solved for the primary phase, and the primary phase volume fraction can be computed based on:

$$\sum_{n=1}^{n} \alpha_q = 1 \tag{2.13}$$

Thus for the two phase flow, we have:

$$\alpha_1 = 1 - \alpha_2 \tag{2.14}$$

In the two phase flow, for the material properties in each cell, the density can be expressed as:

$$\rho = \alpha_2 \rho_2 + (1 - \alpha_2)\rho_1 \tag{2.15}$$

Where ρ_1 and ρ_2 represent the density of the two phases.

2.2. DIMENSIONLESS GROUPS

The dimensional analysis and dimensionless groups of the bypass pig CFD model are introduced in this section. Based on the dimensionless groups, the control parameters of the bypass pigs numerical models can be much more clear. We first start with the conventional bypass pig, as this type of bypass pig is the simplest bypass pig studied in this research.

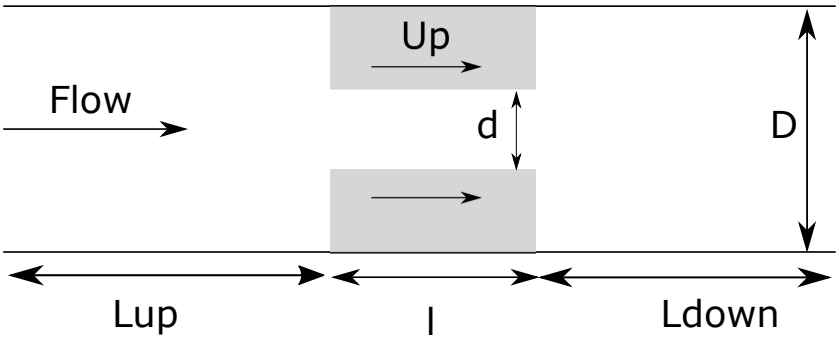

Figure 2.1: 2D sketch of the conventional bypass pig

Figure 2.1 shows the 2D sketch of the conventional bypass pig. The key parameters that govern the conventional bypass pig are summarized in Table 2.1. In this research, the dimensions of the variables are length (L), mass (M), time (T) and degree (D).

The Buckingham Π theorem is applied for the dimensionless analysis, as for the conventional bypass pig we have eight variables and three dimensions, five dimensionless groups are required. The dimensionless groups which are independent of each other are summarized in Table 2.2.

The motivation of choosing these dimensionless groups is as follows:

- The dimensionless group bypass area $(d/D)^2$ represents the ratio of the cross sectional area of the bypass region and the pipe. This dimensionless parameter represents the degree of contraction of the flow to pass the bypass pig.

- The dimensionless group bypass aspect ratio l/d represents the ratio of the length and diam-

Bypass pigs	Parameter	Symbol	Dimensions
Conventional bypass pig	Pipe diameter	D	[L]
	Bypass diameter	d	[L]
	Bypass pig length	l	[L]
	Bulk velocity in pipe	U_D	$[L][T]^{-1}$
	Pig velocity	U_P	$[L][T]^{-1}$
	Pressure drop	Δp	$[M][L]^{-1}[T]^{-2}$
	Fluid density	ρ	$[M][L]^{-3}$
	Fluid viscosity	μ	$[M][L]^{-1}[T]^{-1}$
Disk pig	Diameter of disk	H	[L]
	Distance between pig body and the disk	h	[L]
	Diameter of downstream pipe	D^*	[L]
	Thickness of the disk	t	[L]
Complex bypass pig	Diameter of holes' inner wall	H_i	[L]
	Number of opening holes	$n = 4$	[-]
	Angle of opening holes	ω	[D]

Table 2.1: Parameters which govern the bypass pigs CFD models

eter of the bypass region. A large bypass aspect ratio represents that the pig can be treated as a thick orifice[19].

- The bulk Reynolds number $\rho D U_D/\mu$ has already been introduced in Section 2.1.2, and this dimensionless group represents the flow condition around the bypass pig.
- The velocity ratio U_P/U_D is the ratio of the bulk velocity and the pig velocity. It determines the amount of fluids which can pass through the bypass pig. For instance, if the U_P/U_D is equal to 1, the pig is moving as the same velocity of the pipe flow, thus no fluid can pass through the pig.
- The pressure loss coefficient $\Delta p/(\frac{1}{2}\rho U_d^2)$ compares the overall pressure drop across the bypass pig to flow's kinetic energy per unit volume in the horizontal bypass region.

After the dimensional analysis, the dimensionless groups of the conventional bypass pig can be combined into:

$$\frac{\Delta p}{\frac{1}{2}\rho U_d^2} = f((\frac{d}{D})^2, \frac{l}{d}, \frac{\rho D U_D}{\mu}, \frac{U_P}{U_D}) \tag{2.16}$$

Where U_d represents the velocity in the bypass region, which is dependent on the parameter U_D, U_P and the dimensionless group $(\frac{d}{D})^2$.

The disk pig is another bypass pig which is studied in this research, its geometry is based on the conventional bypass pig, and there is a deflector, shaped as a disk after the horizontal bypass region. Figure 2.2 shows the 2D sketch of the disk pig. Besides the parameters for the conventional bypass pigs, for additional parameters are required to govern the shape of the disk, which are summarized in Table 2.1. Thus, four additional dimensionless groups are required by the disk pig model, which are summarized in Table 2.2.

The disk aspect ratio t/H represents the ratio of the thickness and the diameter of the disk. In reality, the thickness of the disk should be relatively small[19], which means the disk aspect ratio

Bypass pigs	Dimensionless groups	Expression
Conventional bypass pig	Bypass area	$(d/D)^2$
	Bypass aspect ratio	l/d
	Bulk Reynolds number	$\rho D U_D/\mu$
	Velocity ratio	U_P/U_D
	Pressure loss coefficient	$\Delta p/(\frac{1}{2}\rho U_d^2)$
Disk pig	Disk aspect ratio	t/H
	Disk height	H/D
	Downstream pipe diameter	D^*/D
	Disk bypass area	$4d \cdot h/D^2$
Complex bypass pig	Thickness of bypass adjusting holes	H_i/H
	Opening fraction of the holes	$\omega/45°$

Table 2.2: Dimensionless groups for the bypass pigs models

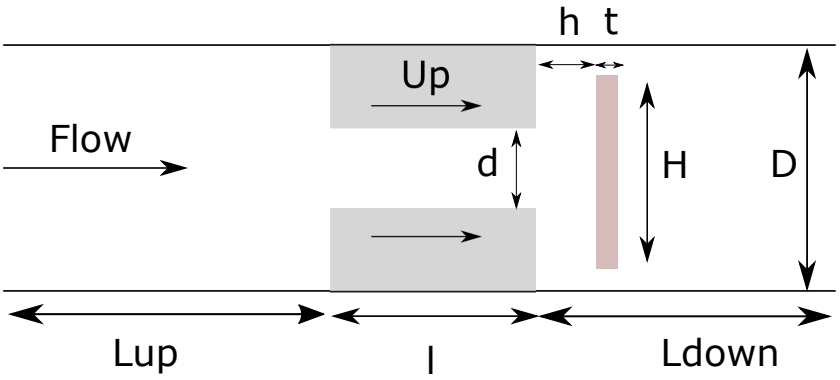

Figure 2.2: 2D sketch of the disk pig

t/H should be << 1.

The disk height H/D represents the relative size of the disk and pipe, and it is determined as the ratio of the disk diameter H and the pipe diameter. For the disk pig geometry, the dimensionless parameter is in the range: $d/D < H/D < 1$, as the diameter of the disk has to be larger than the horizontal bypass region diameter, and smaller than the pipe diameter.

Another dimensionless parameter downstream pipe diameter D^*/D represents the diameter of the downstream pipe. In reality, this dimensionless parameter is equal to 1, as the diameter of the pipeline is a constant. However, in this research the diameter of the downstream pipe's influence on the flow behaviour around the bypass pigs is investigated. When this dimensionless parameter is equal to 1, the downstream pipe's diameter is equal to the upstream pipe's diameter; if this parameter is relatively large, the downstream pipe has much larger diameter than the upstream pipe.

In the disk pig, there is another bypass region around the disk, and the disk bypass area is defined as the smallest cylindrical surface area that the flow has to pass through, and it is equal to $\pi d \cdot h$. The dimensionless parameter disk bypass area $4d \cdot h/D^2$ is determined as the ratio of the disk bypass area and the pipe cross sectional area. The parameter $4d \cdot h/D^2$ can be compared with the parameter $(d/D)^2$, to compare the areas of the two bypass regions in the disk pig.

As discussed in Section 1.4, in this research, the complex bypass pig with bypass adjusting device is studied. Figure 2.3a shows the 2D sketch of the complex bypass pig, which is based on the disk pig model, and in order to represent the bypass adjusting device, opening holes are generated between the horizontal bypass region and the disk, which is shown in Figure 2.3b. Thus, the complex bypass pig requires additional parameters to govern the bypass adjusting holes, which are summarized in Table 2.1.

The parameter angle of opening holes ω represents the angle of each opening holes, and in this research, we change this parameter, in order to represent bypass adjusting operation.

In this research, we keep the parameter number of opening holes $n = 4$, thus two additional dimensionless groups are required by the complex bypass pig model, which are summarized in Table 2.2.

The dimensionless parameter thickness of bypass adjusting holes H_i/H represents the ratio of diameter of the inner wall and outer wall of the bypass adjusting holes. The thickness of the bypass adjusting device should be relatively small, thus the dimensionless group thickness of bypass ad-

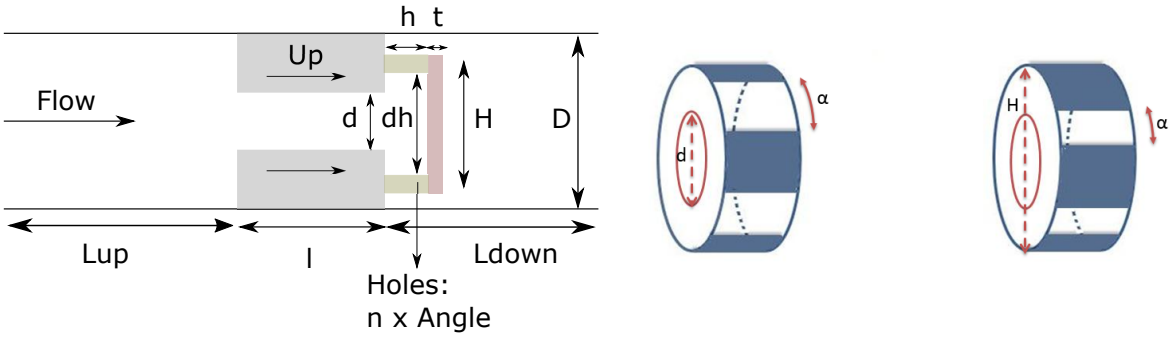

(a) 2D sketch of the complex bypass pig

(b) Bypass adjusting device in the complex bypass pig

Figure 2.3: 2D sketch of the complex bypass pig

justing holes H_i/H should be close to 1. In this case, the flow around the bypass adjusting holes will be treated as the flow around the sharp-edged orifice in this research. This assumption will be introduced later.

In the complex bypass pig model, there are four opening holes, so the maximum angle of each holes is 45°. Thus, changing of the dimensionless parameter opening fraction of the holes $\omega/45°$ represents the bypass adjusting process. In the case when the bypass adjusting holes is fully opened, the parameter $\omega/45° = 1$; and when the bypass adjusting holes is fully closed, $\omega/45° = 0$, in this case, the flow cannot pass through the pig, and the pig will move with the same velocity of the flow. Thus, changing of the dimensionless parameter opening fraction of the holes between the range $0 < \omega/45° < 1$ represents the speed control process of the bypass pig.

In the complex bypass pig, there is an additional bypass region in the bypass adjusting holes, and the area of this bypass region can be expressed as:

$$F_{holes} = \pi H_i h \frac{n \cdot \omega}{360} \tag{2.17}$$

Where $n = 4$.

Also, in order to represent the additional bypass region in complex bypass pig, one additional dimensionless number: opening holes bypass area is suggested at here, and it can be expressed as:

$$\text{Opening holes bypass area} = \frac{H_i h \omega}{22.5 D^2}$$

2.3. FULLY DEVELOPED PIPE FLOW AND ENTRANCE LENGTH

In a pipeline with a relatively long length, the flow in it should be in the fully developed condition. Thus, the theories relevant to the fully developed pipe flow are introduced in this section. Furthermore, in this research we would like to achieve fully developed pipe flow and set its profiles as the boundary conditions of the bypass pig CFD model. Thus, the theoretical equations to calculate the required entrance length of the upstream pipe are introduced in this section.

A fluid needs some length to develop the velocity profile after entering the pipe. When a fluid is entering a pipe with a uniform velocity, the fluid in the layer, which contacts the pipe wall, has the same velocity of the wall due to the no-slip condition. Due to the viscosity of the fluid, the layer which is in contact with the pipe wall resists the motion of adjacent layers and decreases the fluid

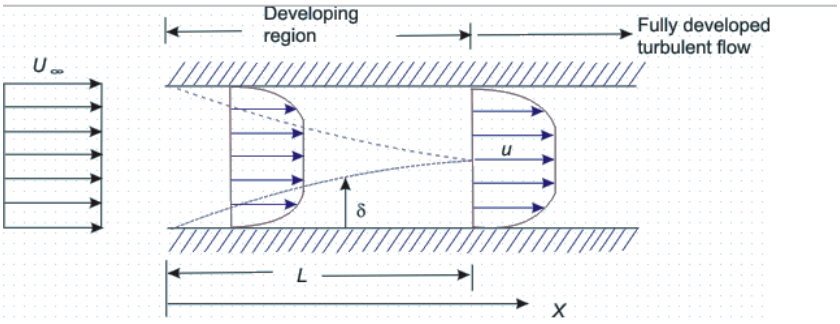

Figure 2.4: Developing turbulent pipe flow[1]

velocity gradually. From the mass conservation, the velocity of middle layers of the fluid in the pipe increases. This develops a velocity gradient across the cross section of the pipe. The developing velocity profile of a fluid entering a pipe is shown in Figure 2.4.

The layers in which the shearing viscous forces are significant, is called boundary layer. The boundary layer divides the pipe flow into two regions:

- Boundary layer region: The region in which viscous effects and the velocity changes are significant.
- The irrotational flow region: The region in which the viscous effects and the wall normal velocity changes are negligible.

When the fluid just enters the pipe, the thickness of the boundary layer gradually increases from zero as we move in the direction of fluid flow, and eventually it reaches the pipe center and fills the entire pipe. This region from the entrance of pipe to the point where the boundary layer covers the entire pipe is termed as the hydrodynamic entrance region. In this region the velocity profile is developing and the flow is called the developing flow. After this region, the velocity profile is fully developed and continues unchanged. This region is called the fully developed region.

In order to calculate the required entrance length for the pipe flow, a dimensionless number entrance length El is introduced at here, and it can be expressed as:

$$El = l_e/D \tag{2.18}$$

where l_e represents the length required to fully developed velocity profile and D represents pipe diameter.

White[1] suggested that based on dimensional analysis, the entrance length l_e is only dependant on the Reynolds number Re, and the entrance length number El can be calculated by:

For laminar flow:

$$El_{laminar} = 0.06Re \tag{2.19}$$

For turbulent flow:

$$El_{turbulent} = 4.4Re^{1/6} \tag{2.20}$$

In our case, the flow in the pipeline is strongly turbulent, thus, Equation 2.18 and 2.20 can be used to calculate the required entrance length for the bypass pig CFD model, if the flow enters the pipe with a uniform velocity, in order to let the flow in the upstream pipe to be fully developed.

2.4. PRESSURE LOSSES IN VARIOUS GEOMETRIES

In this section, the correlations to calculate the pressure drop in various geometries, which are related to the bypass pigs, are introduced. Before introducing the correlations for various geometries, a dimensionless variable: total pressure loss coefficient K is firstly introduced.

It has already been shown that the correlations suggested by Idelchik[22] can calculate the pressure loss (coefficient) for various geometries, for instance sudden contraction and sudden expansion[19]. The 2D sketches of the conventional bypass pig, disk pig and complex bypass pig which are studied in this research are shown in Figures 2.1 2.2 and 2.3a. For the conventional bypass pig, its geometry is a combination of a sudden contraction and a sudden expansion. Similarly, for the disk pig, it is a combination of a sudden contraction and a disk valve. In this research, the bypass adjusting holes in the complex bypass pig (as shown in Figure 2.3b) is considered as a sharp-edged orifice, this approximation will be introduced later. Thus, in this section the correlations to calculate the pressure loss coefficient for the sudden contraction, the sudden expansion, the disk valve, the sharp-edged orifice and the thick orifice are introduced. The correlations introduced in this section will be used to compare with the CFD results.

2.4.1. PRESSURE AND TOTAL PRESSURE COEFFICIENT

In fluid dynamics, the total pressure P_t refers the sum of the static pressure P and the dynamic pressure q. The total pressure coefficient is a variable which is used for studying the incompressible fluids' flow. The total pressure coefficient C_{tp} is expressed as:

$$C_{tp} = \frac{P_t - P_{t_\infty}}{\frac{1}{2}\rho_\infty {V_\infty}^2} \tag{2.21}$$

Where, P_t is the total pressure at the point at which the total pressure coefficient is being evaluated, $P_{t\infty}$ is the maximum total pressure in the flow, ρ_∞ is the free stream fluid density and V_∞ is the maximum velocity (average velocity in different parts) in the flow. In this research, the fluid density is a constant, thus ρ_∞ is equal to ρ.

Furthermore, with definitions of parameters pressure coefficient C_{tp}, which is Equation 2.21, the overall pressure loss coefficient K is expressed as:

$$K = C_{tp_{in}} - C_{tp_{out}} = \frac{\Delta P_t}{\frac{1}{2}\rho {V_\infty}^2} \tag{2.22}$$

Where ΔP_t is the overall total pressure drop.

In this research, we assume the fluids are incompressible. Thus, if the pressure loss coefficient K for a disk pig is known, the overall pressure drop can be calculated by Equation 2.22, as the maximum velocity is dependent on the governing parameters of the bypass pig. Then, the motion of the pig can be described, by Equation 1.1.

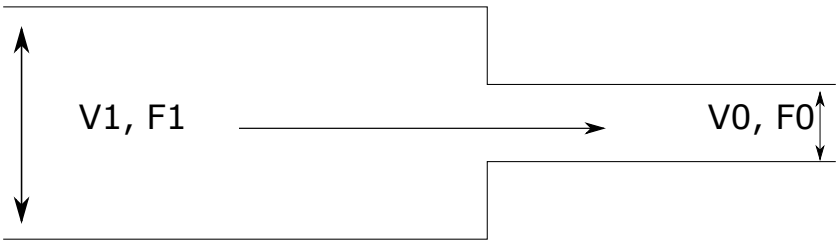

Figure 2.5: 2D sketch of the sudden contraction

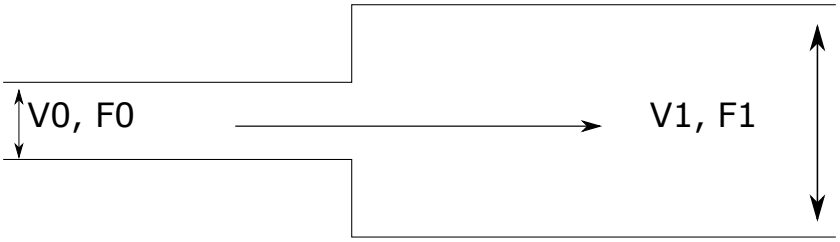

Figure 2.6: 2D sketch of the sudden expansion

2.4.2. PRESSURE LOSS IN SUDDEN CONTRACTION

Figure 2.5 shows the 2D sketch of the sudden contraction. In this research, the correlation for the sudden contraction, which is suggested by Idelchik[22] is used:

$$K_c = \frac{\Delta P_{t_c}}{\frac{1}{2}\rho {V_0}^2} = 0.5(1 - \frac{F_0}{F_1})^{3/4} \tag{2.23}$$

Where K_c is the pressure loss coefficient of the sudden contraction, ΔP_{t_c} is the overall pressure drop across the sudden contraction, V_0 is the velocity in the contraction region, F_0 is the cross section area in the contraction region (narrow pipe) and F_1 is the cross section area of the pipe. From Equation 2.23, we find that the overall pressure loss coefficient K is dependent on the two cross section areas.

2.4.3. PRESSURE LOSS IN SUDDEN EXPANSION

Figure 2.6 shows the 2D sketch of the sudden expansion. Similar as Equation 2.23 for the sudden contraction, the pressure loss coefficient of the sudden expansion K_e is also a function of the two cross section areas F_1 and F_0[22]. The pressure loss coefficient for sudden expansion coefficient can be expressed as:

$$K_e = \frac{\Delta P_{t_e}}{\frac{1}{2}\rho {V_0}^2} = (1 - \frac{F_0}{F_1})^2 \tag{2.24}$$

2.4.4. DISK VALVE

Figure 2.7 shows the 2D sketch of the disk valve. The disk valve is actually based on the pipe flow sudden expansion, and there is a deflector plate just after the narrower pipe. The pressure loss coefficient for disk valve K'_{dv} can be expressed as[22]:

$$K'_{dv} = \frac{\Delta P_{t_{dv}}}{\frac{1}{2}\rho {V_0}^2} = \alpha_0 + \beta_0 \tag{2.25}$$

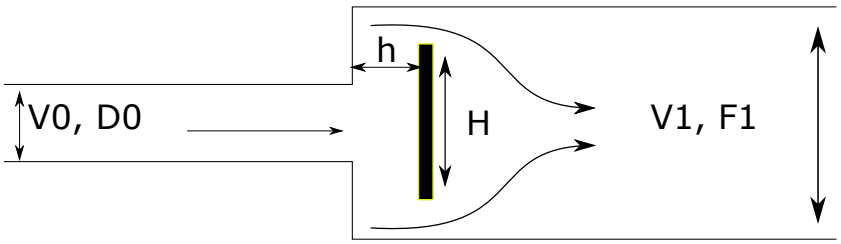

Figure 2.7: 2D sketch of the disk valve

Where:

$$\alpha_0 = 0.55 + 4(\frac{(H - D_0)/2}{D_0} - 0.1) \tag{2.26}$$

and

$$\beta_0 = \frac{0.155}{(h/D_0)^2} \tag{2.27}$$

Where V_0 is the velocity in the narrower pipe, H is the diameter of the disk, D_0 is the diameter of the narrower pipe and h is equal to the distance between the narrower pipe and the disk.

Then, Equation 2.25 can be rewritten as:

$$K'_{dv} = \frac{\Delta P_{t_{dv}}}{\frac{1}{2}\rho {V_0}^2} = 2\frac{H}{D_0} + \frac{0.155{D_0}^2}{h^2} - 1.85 \tag{2.28}$$

In this correlation, we use the pressure loss coefficient K' instead of the K. This is because in Equation 2.22, the velocity is taken as the maximum velocity V_∞. However, in the disk valve, the maximum averaged velocity, which is dependent on the parameters D_0, h and H, can also be in the disk bypass region. Thus, in Equation 2.28 we use the velocity in the narrower pipe V_0, instead of the maximum velocity in the system, to calculate the pressure loss coefficient.

Equation 2.28 is valid within[22]:

$$0.1 < \frac{h}{D_0} < 0.25$$

and

$$1.2 < \frac{H}{D_0} < 1.5$$

2.4.5. PRESSURE LOSSES IN SHARP-EDGED ORIFICE

Figure 2.8 shows the 2D sketch of the sharp-edged orifice. The thickness of the orifice is relatively small, thus, its influence on the overall flow behaviour is negligible[22]. The pressure loss coefficient for sharp-edged orifice K_{seo} can be expressed as[22]:

$$K_{seo} = \frac{\Delta P_{t_{seo}}}{\frac{1}{2}\rho {V_0}^2} = (1 + 0.707\sqrt{1 - F_0/F_1} - F_0/F_1)^2 \tag{2.29}$$

Where F_0 and F_1 represent the cross section area of orifice (smallest area) and pipe, V_0 and V_1 represent the velocity in the orifice (largest velocity) and velocity in pipe respectively.

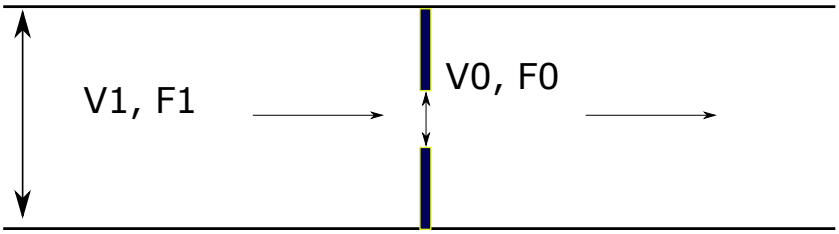

Figure 2.8: 2D sketch of the sharp-edged orifice

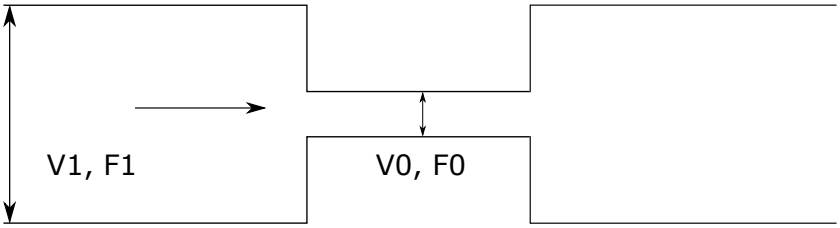

Figure 2.9: 2D sketch of the thick orifice

2.4.6. PRESSURE LOSS IN THICK ORIFICE

Figure 2.9 shows the 2D sketch of the thick orifice. In this case the thickness of the orifice is much larger than the sharp-edged orifice (as shown in Figure 2.8), thus the flow behaviour is totally different if compared with sharp-edged orifice. The pressure loss coefficient for thick orifice can be expressed as[22]:

$$K_{to} = 0.5(1 - \frac{F_0}{F_1})^{0.75} + \tau(1 - \frac{F_0}{F_1})^{1.375} + (1 - \frac{F_0}{F_1})^2 + \frac{4fl}{d} \tag{2.30}$$

Where the F_0 and F_1 represent the cross section area of bypass and pipe respectively, and τ is a parameter dependent on the aspect ratio of the bypass region, while f represents the Fanning friction factor, which is equivalent to the skin friction coefficient.

Obviously, the thick orifice is a combination of a sudden expansion and a sudden contraction. In fact, in Equation 2.30, the first term is the pressure loss due to the sudden contraction (Equation 2.23), and the third term is due to the sudden expansion (Equation 2.24). The second term is a correlation for narrow orifice, while the fourth term represents the wall shear stress on the wall inside of the orifice.

2.4.7. PRESSURE LOSS IN BYPASS PIGS

It has already been tested by the CFD approach that the pressure loss coefficient K for conventional bypass pig can be accurately predicted by the Idekchik's correlation for the thick orifice (Equation 2.30)[18][19], as the conventional bypass pig is shaped like a thick orifice (as shown in Figure 2.9). Furthermore, in Equation 2.30, the second term and the fourth term are relatively small, if compared with the first term due to the sudden contraction and the third term due to the sudden expansion, which can be expressed as:

$$K_{conv} = K_{to} \approx 0.5(1 - \frac{F_0}{F_1})^{0.75} + (1 - \frac{F_0}{F_1})^2 \tag{2.31}$$

Figure 2.10 shows the 2D sketch of the flow around the disk pig. The difference between conventional bypass pig and disk pig is: for the disk pig, there is a deflector plate after the thick orifice,

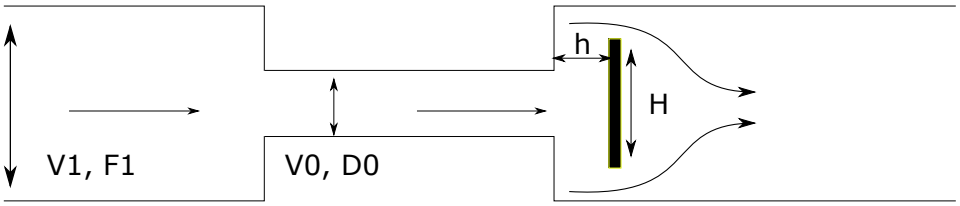

Figure 2.10: 2D sketch of the flow around the disk pig

which is called horizontal bypass area for bypass pigs. Unfortunately, no correlation for disk pig was suggested, as the out flow of the horizontal bypass area will flow around the disk, make the flow behaviour much more complex than the conventional bypass pig (or thick orifice). However, the disk pig is actually a combination of a sudden contraction and a disk valve (as shown in Figure 2.7). Thus, the disk pig model will be studied in this research, and the results from CFD simulations will be compared with the combination of the pressure loss coefficient for sudden contraction K_c and disk valve K_{dv}. This can be expressed as:

$$K_{dp} = K_c + K_{dv} \tag{2.32}$$

2.5. SUMMARY

In this chapter, the relevant theories related to this research are presented. First of all, the governing equations of the numerical models in order to study the flow around bypass pigs are introduced. In this research, RANS (Reynolds-averaged Navier-Stokes) approach is used for the turbulence modelling, and the k-ϵ model is chosen as the turbulence model. Moreover, the VOF (volume of fluid) model is chose for the multiphase modelling, and the transport equation and the numerical approaches of the VOF model are introduced.

Secondly, for the different bypass pigs which are studied in this research, the dimensionless parameters which govern the flow around the bypass pigs are presented, based on a study of the dimensionless groups. In chapters 6 and 7, the relationship between the flow around bypass pigs and these parameters will be studied.

Furthermore, the relevant theories of the fully developed pipe flow is introduced. In reality, the bypass pig is moving in the pipeline, and if the pipeline has a relatively long length, the flow condition in it should be fully developed. In this research, we use the fully developed pipe flow profiles as the boundary conditions of the bypass pigs models, thus Equation 2.20 can be used to predict the required entrance length to let the pipe flow fully develop.

Finally, theories of pressure losses in various geometries, which are related to the bypass pigs' geometries, are introduced. In chapters 6 and 7, these correlations will be used to compare with the results from the bypass pigs CFD studies.

3

NUMERICAL SETUP

This chapter deals with the numerical setup of the bypass pig CFD model. In this research, all the CFD simulations are performed by the commercial CFD package ANSYS Fluent (version 14.5). First of all, the flow domain of a bypass pig, and the boundary conditions of the numerical model, are introduced. As discussed in Section 2.1, the mathematical system of the RANS turbulence modelling approach has to be closed by using a turbulence model, and the turbulence model used in this research is introduced. Furthermore, the meshing strategy is presented in details.

3.1. FLOW DOMAIN AND BOUNDARY CONDITIONS

The flow domains of the bypass pig studied in this research are introduced in this section. Furthermore, the flow domain is formed by different types of boundary conditions. As the flow domain and boundary conditions of the multiphase study are slightly different when compared with the single phase study, the flow domain and boundary conditions for the multiphase flow study are introduced individually.

3.1.1. FLOW DOMAIN FOR SINGLE PHASE STUDY

As discussed in Section 1.4, most of the CFD simulations are based on three-dimensional model in this research. This is because:

- When the bypass pig geometry is not axisymmetric any more, the 2D aixsymmetric CFD model is not available to study flow around this type of bypass pig, and full three dimensional CFD model is required.
- The full 3D CFD model is required by the multiphase flow study, in order to capture the interaction of the gas and liquid phase.

Figure 3.1 shows the real flow domain to represent the process that a bypass pig is moving inside of the pipeline. The flow is moving to right direction, thus, the green line and red line represent the inlet and outlet, respectively. The bypass pig is driven by the fluids in the pipeline, thus the pig is

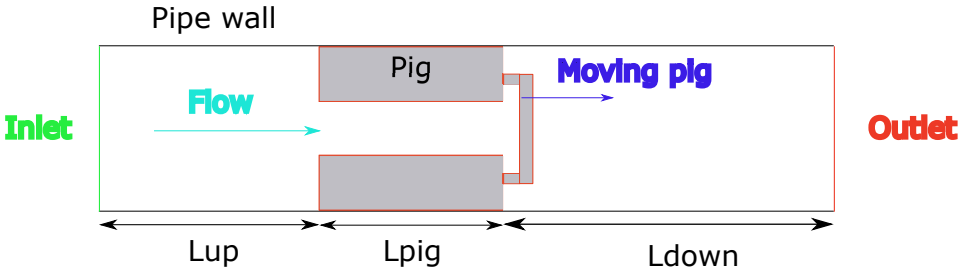

Figure 3.1: Flow domain of bypass pig single phase study

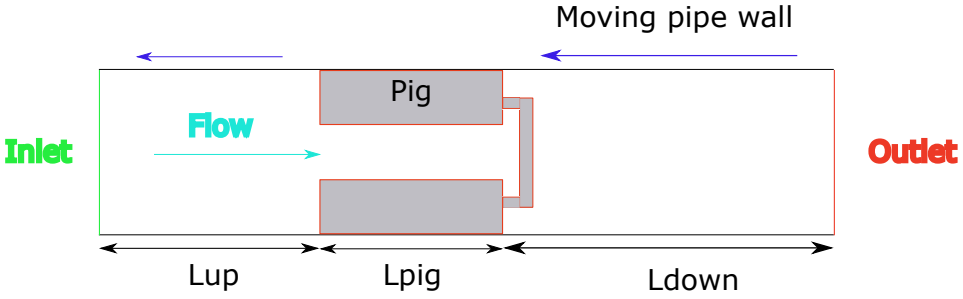

Figure 3.2: Flow domain of bypass pig single phase study in the pig's reference frame

also moving to right direction. As the fluids can pass through the bypass regions, the bypass pig should moves with a smaller velocity than the fluids. The pig is moving inside of the pipeline with certain velocity, thus another boundary condition is the stagnant pipe wall.

However, in order to focus on the flow behaviour around the bypass pig, we used the pig's reference frame, which means the pig is stagnant in this system. Thus, we use the flow domain which is shown in Figure 3.2 instead of the real flow domain which is shown in Figure 3.1. In this system, the pig wall is stagnant, and the pipe wall is moving with the real pig velocity but in another direction. Similarly, the fluid's velocity changes to the velocity relative to the moving pig. The real and relative velocities of the fluids, pig and pipe wall are summarized in Table 3.1.

3.1.2. BOUNDARY CONDITIONS FOR SINGLE PHASE STUDY

For the flow domain shown in Figure 3.1, we set the inlet and outlet as velocity inlet and pressure outlet, respectively. The velocity inlet boundary condition is used to define the velocity and scalar properties of the flow at inlet boundary. For a three dimensional model, three velocity components, i.e. x, y and z direction velocities are required to form the inlet boundary condition. The pressure outlet boundary condition is used to define the static pressure at flow outlet, and the static pressure on the pressure outlet is gauged pressure, which uses the atmospheric pressure (as the operation

Boundary conditions	Real flow domain	Reference flow domain
Inlet	Fluid velocity U	$U - V_{pig}$
Pig	Real pig velocity V_{pig}	0
Pipe	0	$-V_{pig}$

Table 3.1: Velocities of the fluids, pig and pipewall in real and reference flow domain

pressure) as a reference point. Since we assume that the fluids are incompressible, the gauge pressure set on the pressure outlet does not have influence on the simulations' results.

However, since we use the $k-\epsilon$ model for the turbulence modelling, two more governing equations (Equations 2.9 and 3.5) are added in the numerical system. Thus, additional boundary conditions are required by the equations for turbulent kinetic energy k and turbulence dissipation rate ϵ. In this research, this is made by specifying the turbulence intensity I and the turbulence length scale l.

The turbulence intensity I is defined as the ratio of the root-mean-square of the velocity fluctuations:

$$I = \sqrt{\frac{\frac{1}{3}(u'^2 + v'^2 + w'^2)}{U^2}} \tag{3.1}$$

which could also be related to the turbulence kinetic energy k:

$$I = \sqrt{\frac{2k}{3U^2}} \tag{3.2}$$

On the other hand, the turbulence length scale l is a physical quantity related to the size of the large eddies that contain the energy in turbulent flow.

The turbulence intensity I at the core of a fully developed duct flow can be estimated as:

$$I = 0.16(Re)^{-1/8} \tag{3.3}$$

Similarly, the turbulence length scale l is restricted by the size of duct, in fully developed duct flows, which can be estimated as[24]

$$l = 0.07D \tag{3.4}$$

Thus, Equations 3.3 and 3.4 are used to calculate the additional boundary conditions for the velocity inlet and pressure outlet.

The flow domain is bounded by the pipe wall and the pig wall. The difference is: the pig wall is stagnation wall, while the pipe wall is moving with the negative real pig velocity. In order to let the fluid to be fully-developed in the pipeline region, the length of upstream and downstream pipe have to be relatively long.

However, in this research, we actually use the fully developed pipe flow's profiles as the UDF (user defined function) boundary conditions, instead of the uniform boundary conditions which are suggested in this section, for the single phase studies. The UDF boundary conditions approach will be introduced and validated later.

3.1.3. FLOW DOMAIN AND BOUNDARY CONDITIONS FOR MULTIPHASE FLOW STUDY

In general, the CFD model for multiphase flow study is still similar as the single phase model. For instance, we still use the pig's reference frame. Figure 3.3 shows the general flow domain of the multiphase study. Similar as the single phase bypass pig study, the pig is still stagnant, and the pipe wall is moving with the negative real pig velocity. In the oil and gas pipeline, the gas phase and liquid phase are moving as segregated flow. Driven by gravity, the liquid phase flow is in the bottom

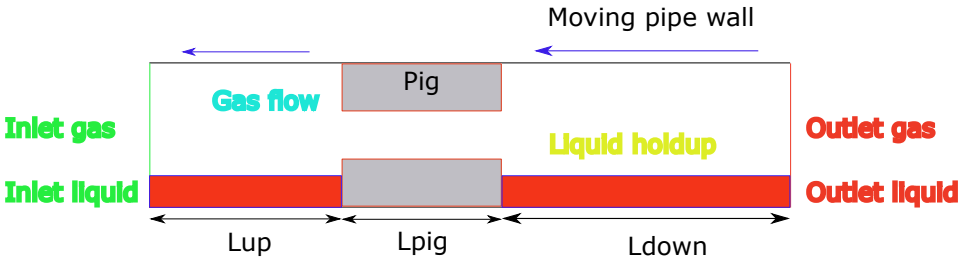

Figure 3.3: General flow domain of the bypass pig multiphase study in the pig's reference frame

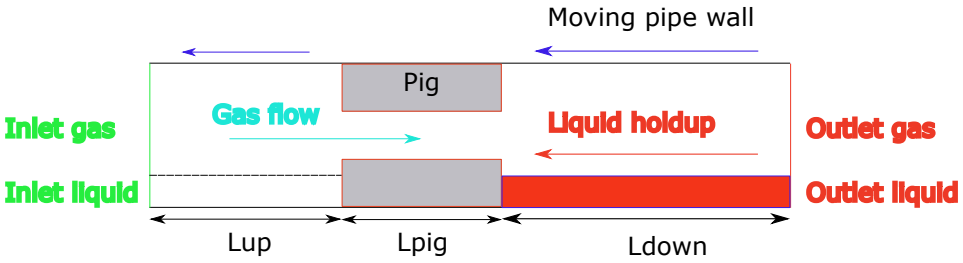

Figure 3.4: Flow domain of the multiphase phase flow around the bypass pig considered in this research

and the gas phase flow is in the upper region of the pipeline. This is shown in Figure 3.3, and the red colour region (bottom of the pipe) represents the liquid phase flow and the white colour region represents the gas phase flow. The moving direction of the liquid and gas phase, and the multiphase flow's behaviour around the bypass pig are determined by the velocities of pig, gas phase flow and liquid phase flow. In the oil and gas pipeline, we assume that the gas velocity is always higher than the liquid phase, and there are three different conditions:

- If the pig moves with a lower velocity than the liquid phase, the two phase flow will drive the pig moves inside of the pipeline. This behaviour is similar as the single phase study.
- If the pig moves with the same velocity as the liquid phase, the liquid has no movement in the reference frame system.
- If the pig moves with higher velocity than the liquid phase, the gas will pass through the bypass region, as the pig's velocity has to be smaller than gas phase. However, in the reference frame system, the liquid phase moves to the opposite direction.

In this research, only the third case is considered. Figure 3.4 shows the flow domain we consider in the multiphase study. The pig is moving inside of the pipeline, with a velocity higher than liquid phase but lower than the gas phase. Thus, in the reference frame, the gas is moving to right direction and the liquid is moving to the opposite direction. As the gas has a higher velocity than pig, the gas can pass through the bypass region of the pig. The liquid cannot pass to the upstream region, thus the liquid slug will appear in the downstream region.

As shown in Figure 3.4, the flow domain is separated into two regions: the gas region (white region, upper) and liquid region (red region, bottom). Thus, the inlet and outlet surfaces are also separated to liquid/gas inlet and outlet. Similar as the single phase study, we set the inlets as velocity inlet, and the gas phase outlet is set as pressure outlet. However, as the liquid is actually moving from

outlet to inlet direction, the liquid outlet is set as velocity inlet. The setting of the (three) velocity inlets and (one) pressure outlet are same as single phase model's boundary conditions. And for the walls boundary, the pipe wall is still setting as moving wall, with the real pig velocity but in another direction, and the pig wall is set as stagnation wall.

3.2. REALIZABLE $k-\epsilon$ TURBULENCE MODEL AND STANDARD WALL FUNCTION

The application of wall functions method in CFD is popular in industry when the $k-\epsilon$ model is being used as the turbulence model, as the wall functions approach can overcome the disadvantages of the $k-\epsilon$ turbulence model. It was suggested that the realizable $k-\epsilon$ model is the most suitable turbulence model for modelling of flow around bypass pigs, as it leads the most realistic results if compared with the experiments' data[18]. Furthermore, the combination of realizable $k-\epsilon$ turbulence model and the standard wall function method in CFD simulations for bypass pig has already been tested by Korban[19]. Thus, in this research we use the realizable $k-\epsilon$ model as the turbulence model, while the standard wall function approach is used for the near wall treatment.

3.2.1. REALIZABLE $k-\epsilon$ MODEL

The standard $k-\epsilon$ model has already been introduced in Section 2.1.4, and it has become as a industry standard. However, the standard $k-\epsilon$ turbulence model has some disadvantages. Fortunately, the research of the standard $k-\epsilon$ model have been developed over time. The realizable $k-\epsilon$ model was introduced by Shih in 1995[25] and it belongs to the $k-\epsilon$ turbulence models family.

The realizable $k-\epsilon$ model became a popular turbulence model in recent years, and it was suggested that this turbulence model performs especially well in the strong separation flow condition[26]. The realizable $k-\epsilon$ model differs from the standard $k-\epsilon$ model in two important ways:

- The realizable $k-\epsilon$ model contains an alternative formulation for the turbulence viscosity.
- A modified transport equation for the dissipation rate ϵ has been derived from an exact equation for the transport of the mean-square vorticity fluctuation.

The transport equation for turbulence kinetic energy k in the realizable $k-\epsilon$ model is same as Equation 2.9 for the standard $k-\epsilon$ model, and a new transport equation for the dissipation rate ϵ is used:

$$\frac{\partial}{\partial t}(\rho\epsilon)+\frac{\partial}{\partial x_j}(\rho\epsilon u_j)=\frac{\partial}{\partial x_j}[(\mu+\frac{\mu_t}{\sigma_\epsilon})\frac{\partial\epsilon}{\partial x_j}]+\rho C_1 S\epsilon-\rho C_2\frac{\epsilon^2}{k+\sqrt{\nu\epsilon}}+C_{1\epsilon}\frac{\epsilon}{k}C_{3\epsilon}G_b+S_\epsilon \tag{3.5}$$

Where:

$$C_1=\max[0.43,\frac{\eta}{\eta+5}],\ \eta=S\frac{k}{\epsilon}\ \text{and}\ S=\sqrt{\frac{1}{2}(\frac{\partial U_j}{\partial x_i}+\frac{\partial U_i}{\partial x_j})^2}$$

As discussed in Section 2.1.4, in this research the G_b and Y_M are neglected, and the turbulence production G_k is calculated by Equation 2.10.

The $k-\epsilon$ models calculate the eddy viscosity by Equation 2.11, and in the realizable $k-\epsilon$ model, the coefficient C_μ is no longer a constant, but being calculated by:

$$C_\mu=\frac{1}{A_0+A_s\frac{kU^*}{\epsilon}} \tag{3.6}$$

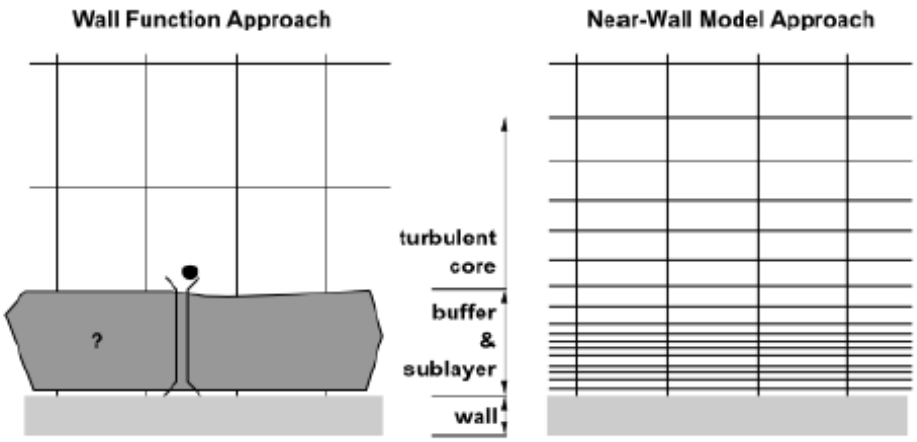

Figure 3.5: Wall functions approach in CFD, reproduced from [24]

Where A_0=4.04 is a constant, A_s is calculated by the mean shear rate and U^* is given by:

$$U^* = \sqrt{\frac{1}{4}(\frac{\partial U_j}{\partial x_i} + \frac{\partial U_i}{\partial x_j})^2 + \frac{1}{4}(\frac{\partial U_j}{\partial x_i} - \frac{\partial U_i}{\partial x_j})^2} \tag{3.7}$$

In Fluent, the model constants for realizable $k-\epsilon$ model have the following values[24]:

$$C_{1\epsilon}=1.44,\ C_{2\epsilon}=1.92,\ \sigma_k=1.0 \text{ and } \sigma_\epsilon=1.2$$

3.2.2. STANDARD WALL FUNCTION

The $k-\epsilon$ turbulence model is only valid in fully turbulent flow, thus it cannot modelling the flow in the near wall region accurately. Typically, this situation can be improved by applying wall functions. The basic idea behind wall functions is applying boundary conditions at some distance away from the wall boundary, which is shown in Figure 3.5. The wall conditions have another important advantage: the mesh resolution close to the walls can be significantly lower than without applying wall functions but solving the fluids in the near wall region completely.

In this research, the standard wall function is being used in order to bridge the viscosity-affected region. In theory, velocity profile in the logarithmic sub layer can be expressed as:

$$u^+ = \frac{1}{\kappa}\ln y^+ + B \tag{3.8}$$

Where κ is the von Karman constant approximately equals to 0.41, B is a constant equal to 5.2[24], y^+ and u^+ are the dimensionless distance and dimensionless velocity, respectively.

The dimensionless distance y^+ and dimensionless velocity u^+ can be both computed from the friction velocity u_τ, which can be expressed as:

$$u_\tau = \sqrt{\frac{\tau_w}{\rho}} \tag{3.9}$$

Where τ_w is the wall shear stress. And the dimensionless distance y^+ can be expressed as:

$$y^+ = \frac{u_\tau y}{\nu} \tag{3.10}$$

Where y is the distance to the wall and ν is the kinematic viscosity. On the other hand, the dimensionless velocity u^+ can be expressed as:

$$u^+ = \frac{u}{u_\tau} \tag{3.11}$$

For the standard wall function used in Fluent, Equation 3.8 can be rewritten as:

$$U^* = \frac{1}{\kappa}\ln(Ey^*) \tag{3.12}$$

Where the dimensionless velocity U^* and dimensionless distance y^* can be expressed as:

$$U^* = \frac{\rho U_P C_\mu^{1/4} K_P^{1/2}}{\tau_w} \tag{3.13}$$

and

$$y^* = \frac{\rho C_\mu^{1/4} K_P^1/2 y_P}{\mu} \tag{3.14}$$

Where E=9.793 is the empirical constant, U_P and k_P represent the mean velocity of fluid and the turbulence kinetic energy at the near wall node P, respectively; y_P represents the distance from point P to the wall; In Fluent, the von Karman constant $\kappa = 0.4187$.[24].

Furthermore, for the turbulence modelling in standard wall function, the boundary condition for turbulence kinetic energy k is given as:

$$\frac{\partial k}{\partial n} = 0 \tag{3.15}$$

Where n is the local coordinate normal to the wall.

Under the local equilibrium hypothesis, the production of kinetic energy G_k and its dissipation rate ϵ at the wall adjacent cells can be expressed as:

$$G_k = \tau_w \frac{\partial U}{\partial y} = \frac{\tau_w^2}{k\rho C_\mu^{1/4} k_P^{1/2} y_P} \tag{3.16}$$

and:

$$\epsilon_P = \frac{C_\mu^{3/4} k_P^{3/2}}{k y_P} \tag{3.17}$$

Moreover, under this hypothesis, the G_k and ϵ are assumed to be equal in the wall adjacent control volume[24].

To apply the wall functions, the dimensionless distance y^+ should within 30 and 20,000, as in this range the flow is in the logarithmic sublayer, in which the log low (Equation 3.8) can be used to predict the velocity profile[23].

3.3. UDF BOUNDARY CONDITIONS

For the single phase studies, we use UDF (user defined function) boundary conditions for the velocity inlet and pressure outlet, instead of the uniform boundary conditions.

In reality, the flow in a relatively long pipeline should be fully developed. As the bypass pig is moving inside of the pipeline, the flow in the pipe region of the CFD model should also be fully-developed. The key parameters of the typical pipe flow involved in this research are summarized

in Table 3.2. Based on these parameters and Equation 2.20, we can calculate the required entrance length of the bypass pig CFD model, in order to achieve fully developed pipe flow in the upstream pipe is:

$$le=74.9\ m$$

Obviously, this entrance length is too long if we use it as the upstream pipe length in the bypass pig CFD models. Thus, we perform a pipe flow study based on a 100 metres pipe CFD model. We can achieve the fully developed pipe flow's profile from this simple pipe study, which are shown in Figure 3.6. Then, we set these profiles as the inlet and outlet boundary conditions of the bypass pig CFD models, through the UDF method. In this way, the inlet and outlet boundary conditions are both set as fully developed pipe flow condition.

For the inlet boundary conditions, the x direction velocity u's profile is shown in Figure 3.6a, the y and z direction velocities v and w should be zero for a fully developed pipe flow.

Furthermore, for the velocity inlet and pressure outlet, two additional boundary conditions are required by the numerical system. In this case, this is made by set the fully developed pipe flow's turbulence kinetic energy k's profile (as shown in Figure 3.6b) and turbulence dissipation rate ϵ's profile (as shown in Figure 3.6c) as the UDF boundary conditions.

Compared with the uniform boundary conditions, the UDF boundary conditions method has two main advantages:

- The boundary conditions are set as the fully developed pipe flow, thus make the inlet and outlet of the bypass pig flow domain more realistic.
- By using this method, we need a relatively shorter upstream pipe length in the bypass pig CFD model (in this case $L_{up} = 2D$), thus a lot of computational resources can be saved during running the simulations.

The fully developed pipe flow's profiles and the UDF boundary conditions approach will be validated later.

3.4. MESHING STRATEGIES

In a CFD study, the meshing is always the most time-consuming part. In order to obtain accurate and reliable numerical solutions, constructing a high quality mesh is necessary. On the other hand,

Parameter	Value
Pipe Diameter D	1.16 m
Density ρ	68 kg/m^3
Viscosity μ	2.264 E-5 kg/ms
Velocity U	2.87 m/s
Reynolds number R_e	1 E+7

Table 3.2: Key Parameters of the pipe flow

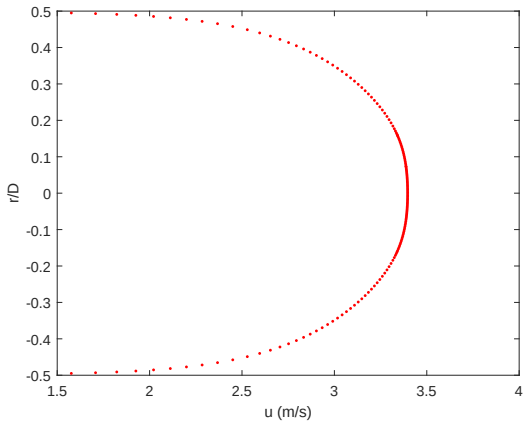

(a) Velocity profile

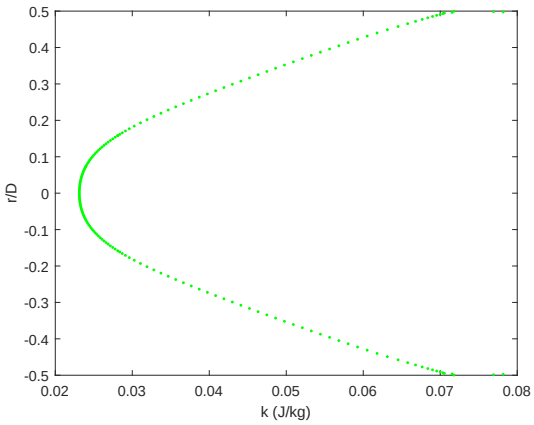

(b) Turbulent kinetic energy's profile

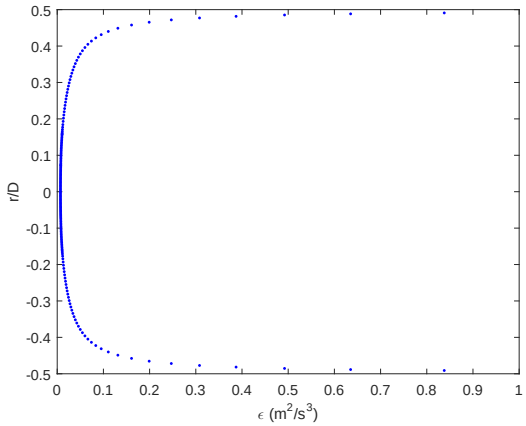

(c) Turbulent dissipation rate profile

Figure 3.6: Fully developed pipe flow profiles

the computing time is strongly dependent on the mesh. In this research, the three dimensional mesh for the bypass pig CFD model is generated by the meshing software ANSYS ICEM-CFD.

In general, there are two types of meshing methods available: structured mesh and unstructured mesh. Figure 3.7 compares the unstructured mesh and structured mesh for the same geometry. The most noticeable difference between the unstructured mesh (as shown in Figure 3.7a) and the structured mesh (as shown in Figure 3.7b) is, the structured mesh follows a uniform pattern, while the unstructured mesh does not. For the structured mesh, the hexahedral elements are orthogonal in i, j and k space (in three dimensional case), every cell has a unique set of (i ,j ,k) values, and this is not available for unstructured mesh.

In CFD, structured hexahedral mesh is always preferred, as this method gives more accurate solutions than the other meshes. Furthermore, by using structured hexa mesh the computation time and memory required can be saved a lot[27].

On the other hand, generating structured mesh is much more complex than unstructured mesh. In ICEM-CFD, the structured hexa mesh is generated through the multi-blocking method. For this method, the geometry is separated into different parts, and each part is represented by a block.

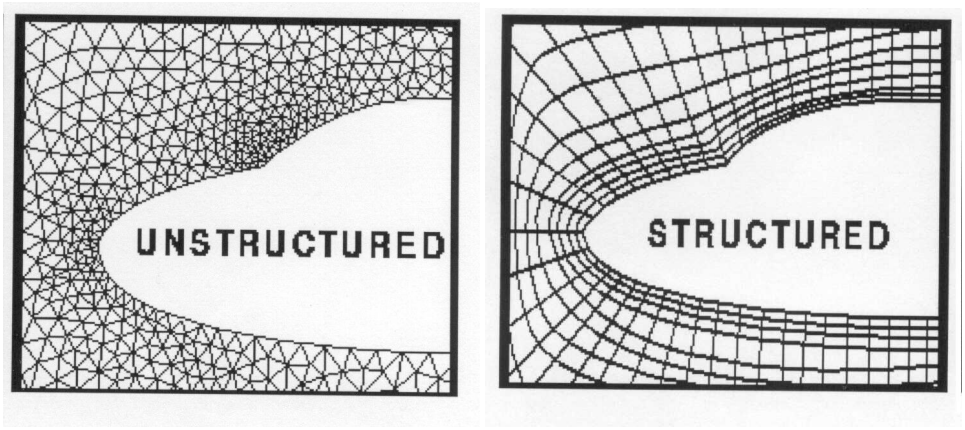

(a) Unstructured mesh (b) Strecutred mesh

Figure 3.7: Comparision between unstrucured mesh and structured mesh

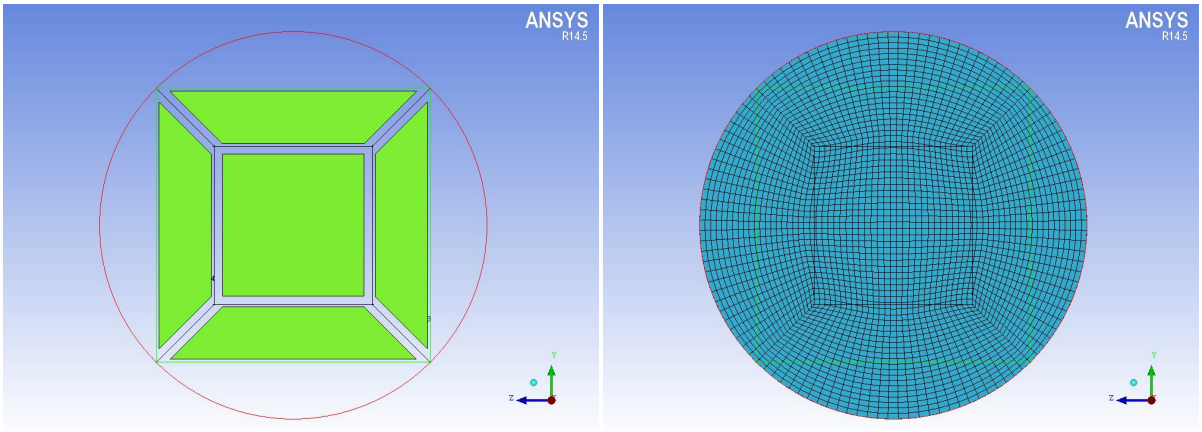

(a) Splited blocks (b) Structured hexahedral mesh generated by multi-blocking method

Figure 3.8: Structured mesh generated by multi-blocking method on a circle surface

Then, the structured mesh elements are mapped on the edges of the blocks, in i, j and k directions.

For instance, Figure 3.8 shows the structured mesh generated on a cylinder, by the multi-blocking approach. Figure 3.8a shows the blocks which separate the cylinder in different parts. The blocks are separated by the automatic O-grid method, and there is a square block in the center, with four blocks around it. The structured hexa mesh generated is shown in Figure 3.8b, and the straight lines represent the edges of the blocks. The settings in order to control the mesh are applied on the edges, and two neighbour blocks are connected by the edge which is shared by two blocks, so the mesh in different regions is also connected. In ICEM-CFD, in order to generate mesh on the boundary surfaces and make the mesh fully fills different regions, the edges have to be associate on the curves of geometry, and this can be done by the software automatically.

Fortunately, in our case the flow domain of the bypass pig is circular. Thus, a similar mesh

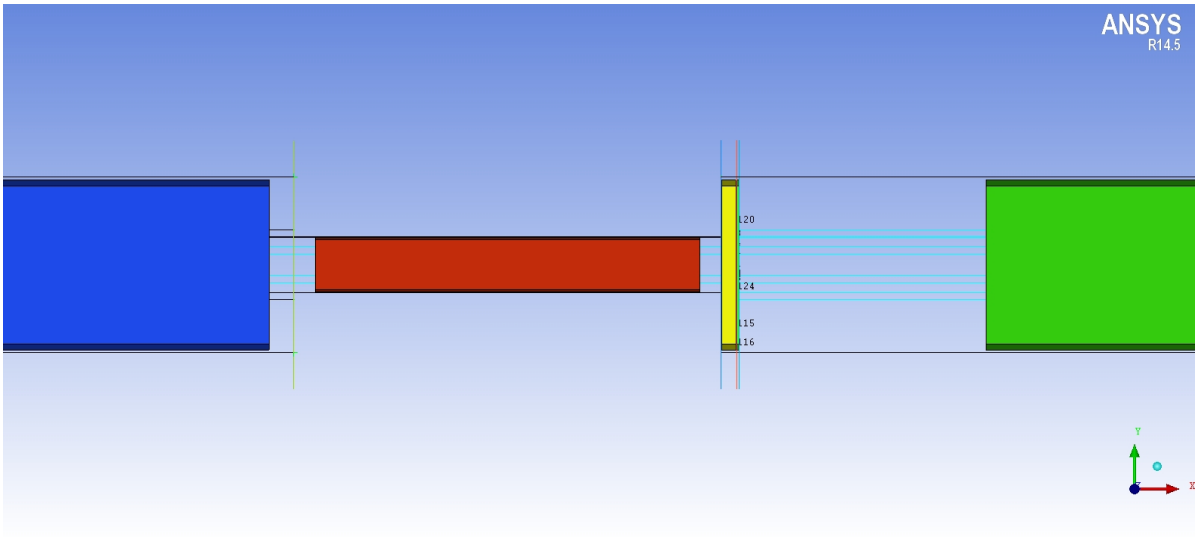

(a) Blocks represent different regions in x direction

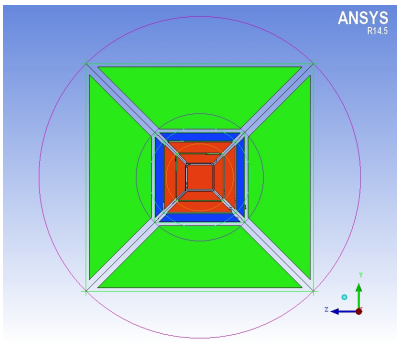

(b) Blocks of pipe region

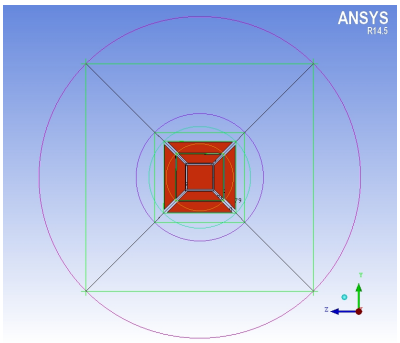

(c) Blocks of bypass region

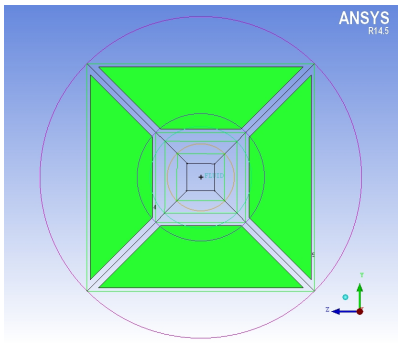

(d) Blocks of disk region

Figure 3.9: Multi-blocking meshing approach: Blocks for the disk pig

method can be perfectly applied for the bypass pig CFD model. Figure 3.9 shows the blocks which represent different parts of the disk pig geometry. In x direction, the initial block is split into five regions, as shown in Figure 3.9a. From let to right, the blue blocks represent the upstream pipe, the red blocks represent the horizontal bypass region, the yellow blocks represent the region between horizontal bypass region and disk, and the green blocks represent the downstream pipe. Another special region, which connects the yellow blocks and the green blocks, represents the flow region around the solid disk. In this figure this region is not shown clearly, as the thickness of disk is relatively small. Similar as the blocks and the mesh for the cylinder, as shown in Figure 3.8, in the y and z direction, for the three dimensional bypass pig model, there is a cubic block in the center and the other blocks are around it in four directions, as shown in Figures 3.9b, 3.9c and 3.9d. In the y and z direction, the initial block is split into three different regions by the O-grid method, as shown in Figure 3.9b, which represents the blocks in the pipe region. Figure 3.9c shows the blocks in horizontal bypass region, and this region has the smallest diameter. Also, Figure 3.9d shows the blocks in the region around the solid disk. In order to full fill different regions with mesh, the edges have to be associate on the curves of the disk pig geometry.

Figure 3.10 shows the mesh generated by the multi-blocking approach for the disk pig. Figure

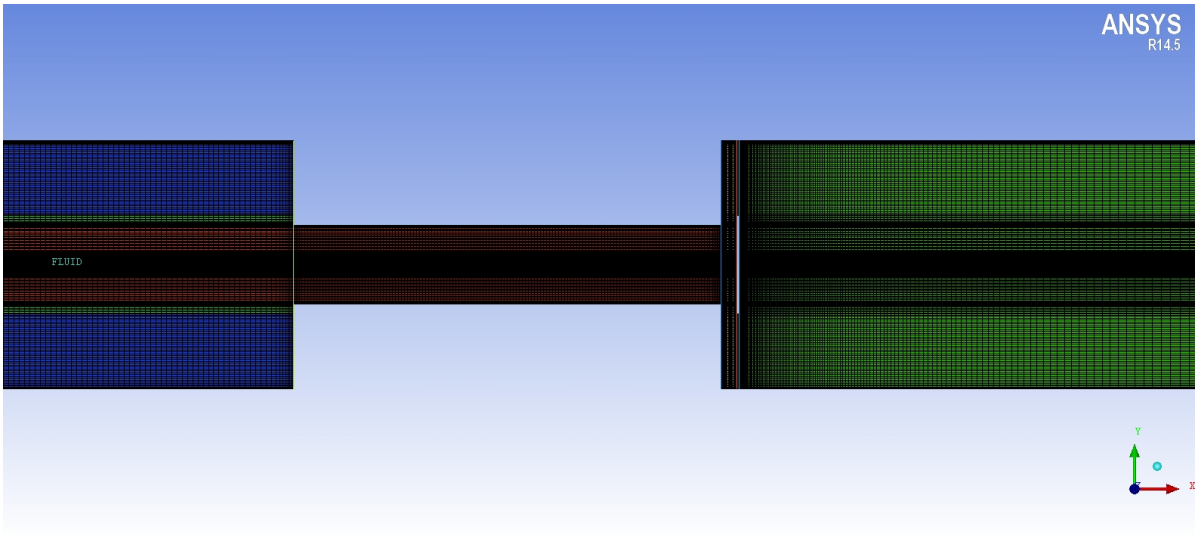

(a) Mesh generated on the cross plane

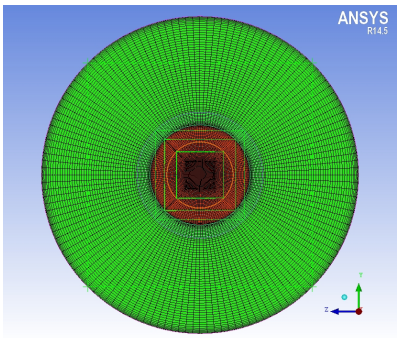

(b) Mesh of pipe region

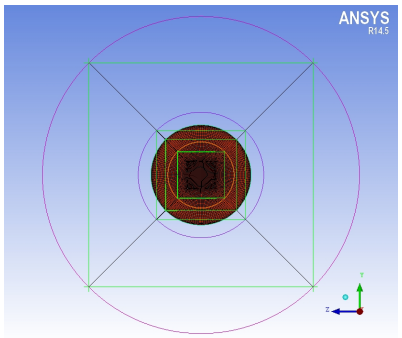

(c) Mesh of bypass region

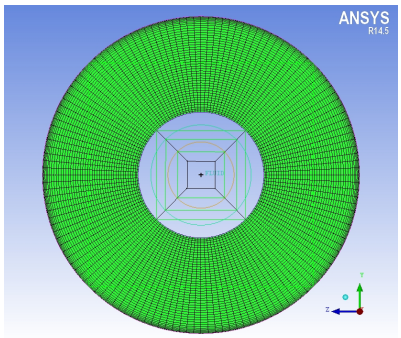

(d) Mesh of disk region

Figure 3.10: Multi-blocking meshing approach: Mesh generated for the disk pig

3.10a shows the mesh on the cross plane, and the blank region in the downstream pipe represents the solid disk. Figure 3.10b, 3.10c and 3.10d show the mesh in the pipe region, horizontal bypass region and the region around the disk, respectively. By using the multi-blocking method, different regions represented by blocks connect with each other, thus the mesh in the horizontal bypass area (Figure 3.10c) with smallest diameter is actually same as mesh in the center of the pipe region (Figure 3.10b), and the mesh in the region around the disk (Figure 3.10d) is same as the outer mesh in the pipe region.

As we split the disk pig into different regions, and different mesh settings are applied on different blocks, then the mesh in different regions has to be connected, in order to increase the quality of mesh. Figure 3.11a shows the mesh details on the cross section plane, and different colours represent different regions. How the meshes in different regions connect with each other is presented on this figure. In ICEM-CFD, this is made by linking two connecting edges from two neighbour blocks, and setting the spacing of the first node and the growth rate on edges.

Furthermore, as discussed in Section 3.2.2, for the bypass pig CFD model we use the standard wall function for the near wall treatment, which requires that the cell closest to the wall should located between $30<y^+<20{,}000$. Thus, the thickness of the cells closest to the wall has to be relatively

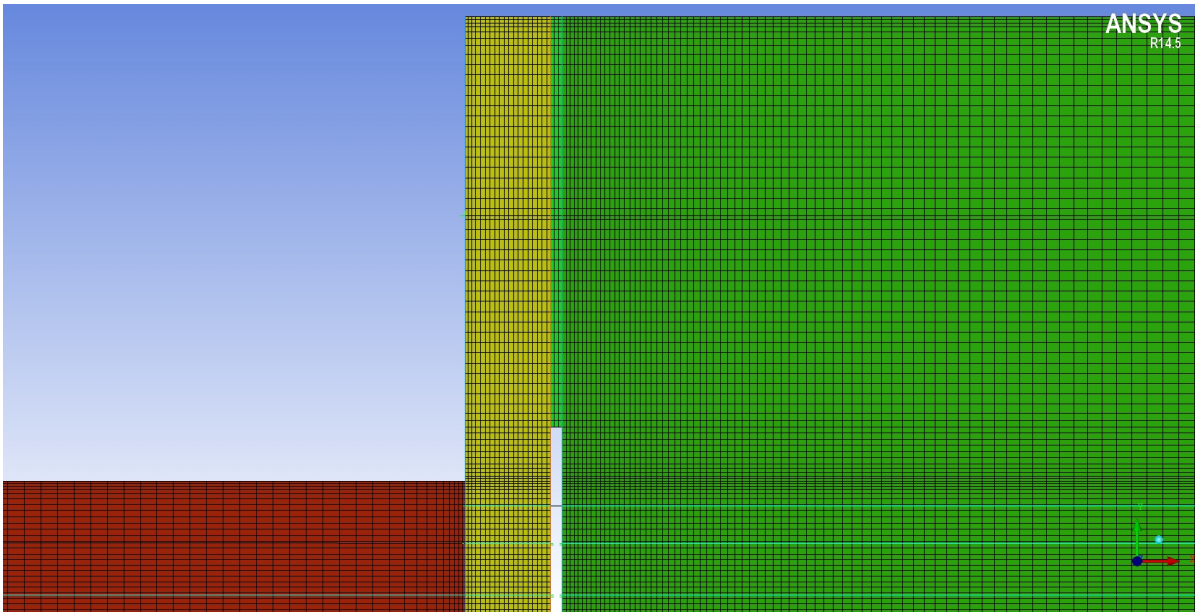

(a) Mesh details on the cross section plane

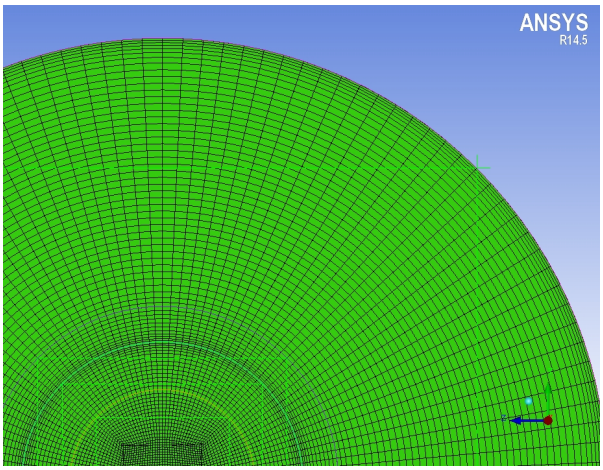

(b) Mesh details in the pipe region

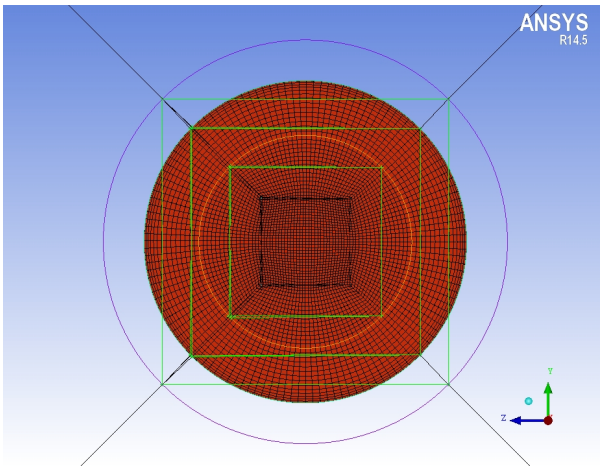

(c) Mesh details in the bypass region

Figure 3.11: Details of the mesh for the disk pig

small, which can be found on Figure 3.5. For the disk pig, we generate the mesh on the walls (upstream and downstream pipe walls and bypass pig wall) with relatively small thickness, which is shown in Figure 3.11b and 3.11c. In ICEM-CFD, this is done by setting a relatively small spacing for the first node on the edge which contacts the wall, and setting a growth rate on the edge. In order to achieve high quality, the growth ratio set at here is 1.2.

In ICEM-CFD, the major quality criteria for the hexa mesh are angle and determinant, which are shown in Figure 3.12. The minimum angle of the hexa mesh generated in our case is 45 degree, as shown in Figure 3.12a, which is much larger than the acceptable angle for the CFD solver ANSYS Fluent. Furthermore, the criteria “Determinant 3×3”represents the general mesh quality. From Figure 3.12b, we find that for the cells with lowest quality, this criteria is still larger than 0.8. Thus, we know that the mesh generated for the disk pig CFD model has very high quality.

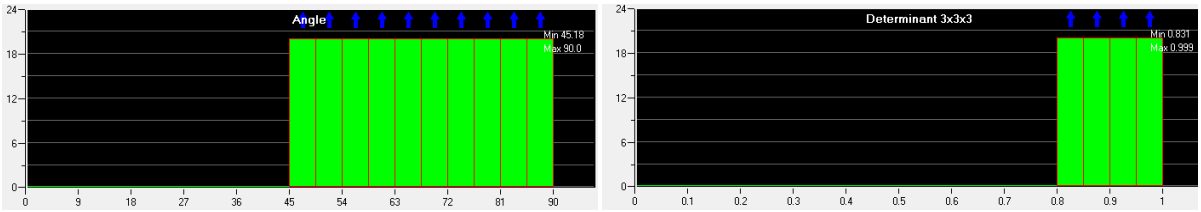

(a) Criteria: angles

(b) Criteria: determinant 3×3

Figure 3.12: Mesh quality

The very high quality mesh for disk pig is introduced in this section, and for the CFD models for the other bypass pigs, similar meshing approach can be used, as the bypass pigs have circular geometry. For instance, for the complex bypass pig geometry which has bypass adjusting holes, the only difference is the blocks are split further in the y and z direction into different parts.

3.5. SUMMARY

In this chapter, the numerical setup of the bypass pig CFD model are introduced in details. First of all, the flow domain to represent the process that the bypass pig is moving inside of the pipeline is introduced, and the flow domain is bounded by four boundary conditions: velocity inlet, pressure outlet, the moving pipe wall and the stagnant pig wall. The Equations to calculate the uniform boundary conditions are introduced.

Secondly, in this research, the realizable k-ϵ model is chose as the turbulence model, while the standard wall function is applied for the near wall region treatment. These approaches are introduced in details.

In order to achieve more realistic boundary conditions and decrease the computational resources required, the UDF boundary conditions approach is introduced in this chapter. We first achieve the fully developed pipe flow through a pipe CFD study, and we set the flow's profiles as the boundary conditions for the single phase studies. The fully developed pipe flow's profiles and this modelling approach will be validated in Chapter 4.

Finally, the mesh strategy of the bypass pig CFD models is introduced in details. In this research, the structured hexa mesh is generated by ANSYS ICEM-CFD, through the multi-blocking approach. The bypass pig geometry are split into different regions, and each region is represented by one block. Then, the structured mesh is mapped on the blocks. For the disk pig model, very high quality mesh is generated, and similar meshing approach can be used for the other bypass pigs studies.

4

VALIDATION

This chapter deals with various studies in order to validate the numerical modelling approaches of the bypass pig CFD model, which have been introduced in Chapter 3.

First of all, as the accuracy of the numerical solution and the computing time of the numerical simulation are strongly dependent on the mesh, a mesh independence study is carried out. The mesh independence study is performed by comparing the results from different models with various mesh cell number. Also, as the two dimensional axisymmetric CFD model has already been validated by Korban[19], the results from the new three dimensional CFD model are compared with the validated two dimensional model.

The bypass pigs CFD model for the multiphase flow study is different from the single phase study, and the multiphase study is performed by transient simulations, instead of steady state. Thus the mesh and time step size independence study for multiphase study is carried out individually.

Finally, as discussed in Section 3.3, in the single phase study, we use the fully developed pipe flow profiles as the UDF boundary conditions instead of the uniform boundary conditions. This modelling approach is validated in this chapter.

4.1. MESH INDEPENDENCE STUDY

The mesh independence study aims to make sure that the solutions are independent of the mesh settings. The way we performed the mesh independence study is as follows:

- The first mesh is constructed, and we run a full simulation with this model. The continuity has to decrease to an acceptable range, and the solution has to be converged.
- Then we build the second model, typically with 1.5 times the refinement of the previous mesh. We also run a full simulation on this configuration.
- We compare the results from the two different meshes. If the differences are unacceptable, a third mesh with further refinement is required.

The fluid behaviour around a bypass pig is very complex, especially for the bypass pig with more complex geometry. Thus, meshing error of <1% is acceptable in our case.

In this part, the mesh independence study of the conventional bypass pig and the complex bypass pig is carried out, and the mesh independence study of the disk pig will be introduced in the Appendix.

4.1.1. CONVENTIONAL BYPASS PIG

We first perform the mesh independence study of the conventional bypass pig, as this type of bypass pig has a relatively simple geometry. Moreover, the more complex bypass pigs are based on the conventional bypass pig, which means that the valid mesh settings can be used for the more complex bypass pigs.

The key parameters govern the conventional bypass pig model in this study are summarized in Table 4.1. Three different meshes of varying refinement are tested, with the number of cells: 1,901,856; 4,044,663 and 9,511,515 respectively.

Figure 4.1 shows the distribution of the total pressure coefficient C_{tp} on the centreline. It is found that the total pressure's distribution on the centreline of the mesh with around 4 million cells has very small difference if compared with the mesh with around 10 million cells. The overall pressure drop predicted by these models is similar.

Furthermore, we compare the velocity profiles in the different regions of the model with 4 million cells mesh, with the two dimensional axisymmetric CFD model, which has already been validated by Korban[19]. Figure 4.2 shows the x velocity u profile in different regions. From Table 4.1, we know that the location of the back of the pig is at x = 0, and the pig length is 2m. Thus, Figure 4.2a shows the velocity profile in the upstream pipe, Figure 4.2b and 4.2c show the velocity profiles in the bypass region, and Figure 4.2d shows the velocity profile in the downstream pipe. It is found that the flow behaviour obtained by the three dimensional model is similar as the validated two dimensional model.

Parameter	Value
Bulk velocity U	2.87 m/s
Horizontal bypass area (%)	10%
Pipe Diameter D	1.16 m
Bypass pig diameter d	0.3668 m
Upstream pipe length	$5D$
Downstream pipe length	$20D$
Pig length	2 m
Location of the back of the pig	z=0
Density ρ	68 kg/m^3
Viscosity μ	2.264 E-5 kg/ms
Reynolds number R_e	1 E+7

Table 4.1: Key Parameters govern the conventional bypass pig geometry used in the mesh independence study

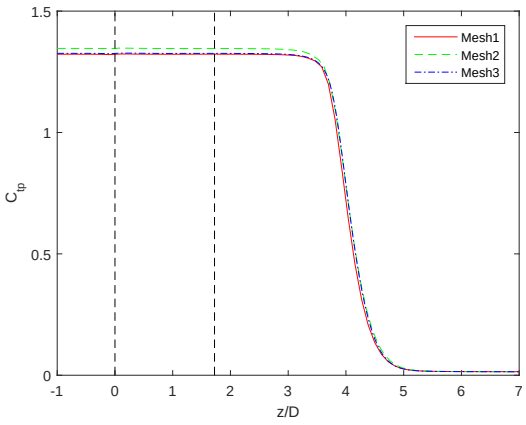

Figure 4.1: Total pressure coefficient along the centreline for the conventional bypass pig

Finally, the important wall quantity y^+, which is calculated by Equation 3.8, is plot in Figure 4.3. It is found that both of the mesh and the flow of the conventional bypass pig are axisymmetric. As discussed in Section 3.2.2, the standard wall function has no modelling error if the wall quantity lies within $30 < y^+ < 20000$. In this case it is found that the y^+ values are all in acceptable range.

4.1.2. COMPLEX BYPASS PIG

The complex bypass pig, which contains the bypass adjusting device, has a more complex geometry than the previous model. However, the mesh settings for the complex bypass pig model can still inspired by the mesh validated in Section 4.1.1. The key parameters which govern the complex bypass pig model used in this study are summarised in Table 4.2. As discussed in the Section 3.3, the complex bypass pig model uses the fully developed pipe flow profiles as the boundary conditions. By using this approach, the upstream pipe length is decreased from $5D$ to $2D$. This modelling approach will be validated in Section 4.3. Two meshes are generated for the complex bypass pig model, with 5,157,598 and 8,348,462 cells respectively. The first mesh, which has around five million cells, is inspired by the validated mesh for the conventional bypass pig, and another mesh with further refinement is generated, in order to investigate if the first mesh is fine enough to achieve mesh independent solution.

Figure 4.4 shows the total pressure coefficient C_{tp}'s distribution on the centreline. It is found that the pressure drop predicted by the two meshes is similar.

Furthermore, we compare the velocity profiles in different regions. Figure 4.5 shows the velocity profile at different positions in the x direction. Based on the parameters summarized in Table 4.2, we know that Figure 4.5a shows the velocity profile in the upstream pipe; Figure 4.5b shows the velocity profile in the horizontal bypass region; as h is the distance between the pig body and the disk, Figure 4.5c shows the velocity profile in the bypass adjusting region; And Figure 4.5d shows the velocity profile in the downstream pipe. From Figure 4.5, we find the flow behaviour obtained by the mesh 1 is similar as the mesh 2.

Also, as discussed before, in order to apply the wall functions, it is required that the y^+ value lies within $30 < y^+ <20000$, and Figure 4.6 shows the y^+ values are all in acceptable range. In this case,

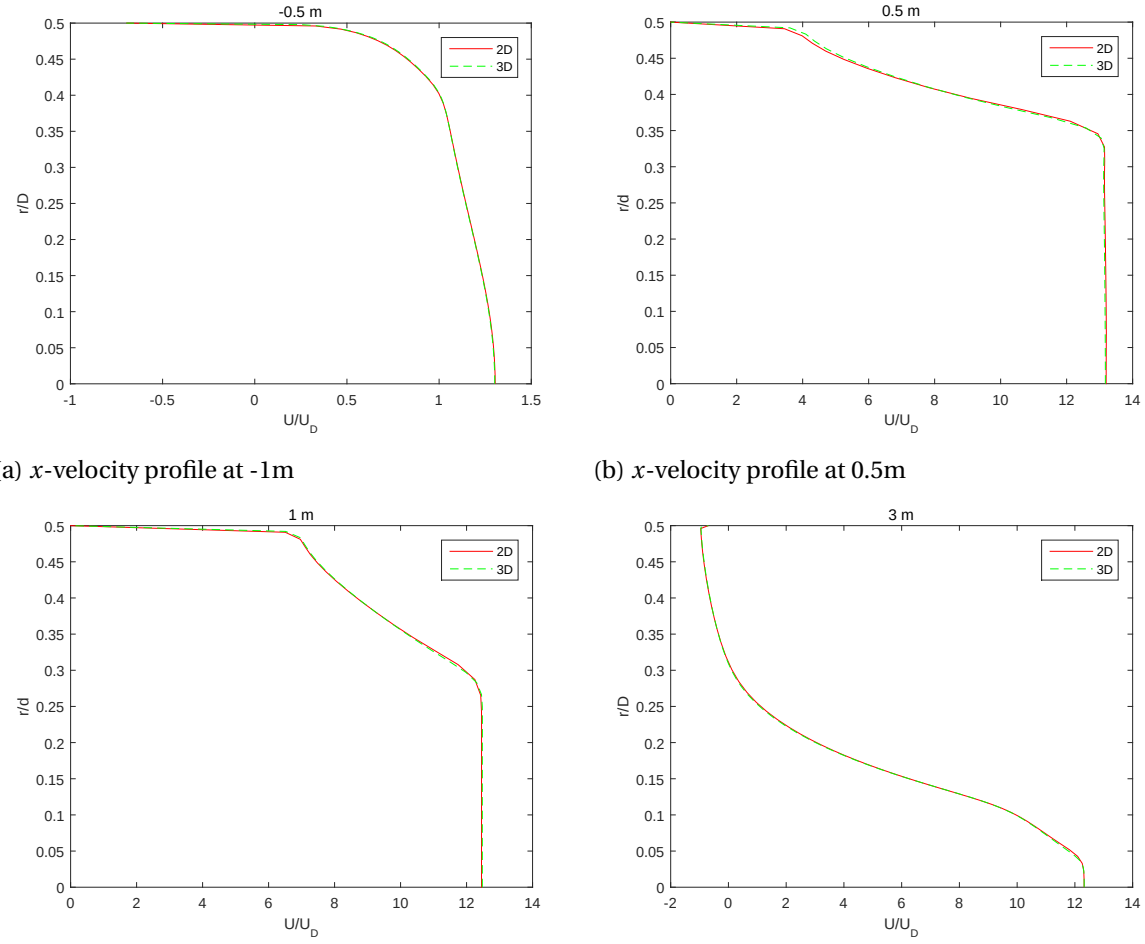

(a) x-velocity profile at -1m

(b) x-velocity profile at 0.5m

(c) x-velocity profile at 1m

(d) x-velocity profile at 3m

Figure 4.2: Velocity profiles for the conventional bypass pig mesh independent study

the mesh is still axisymmetric, but the flow around the bypass pig is not axisymmetric any more after the horizontal bypass region, due to the bypass adjusting holes. This is also shown in this figure.

Thus, the first mesh is acceptable and we do not need a third mesh with further refinement. And the complex bypass pig studies are based on the first mesh which is studied in this part.

4.2. MESH AND TIME STEP SIZE INDEPENDENCE STUDY FOR MULTIPHASE STUDY

The bypass pig CFD model for the multiphase flow study is different to the single phase studies, thus, the mesh independence study for multiphase study is presented individually. Furthermore, we use the transient simulation in the multiphase flow study, instead of the steady state simulation. Thus the time step size independence is studied in this section, in order to make sure that the solution is independent on the time step size setting.

The flow domain and boundary conditions are introduced in Section 3.1.3, and the mesh & time independent study are based on a bypass pig model with 4% bypass area. The key parameters which govern the bypass pig model used in this mesh & time step size independent study are summarized in Table 4.3. The condition we consider here is: in the real pipeline, the gas is moving with 8 m/s,

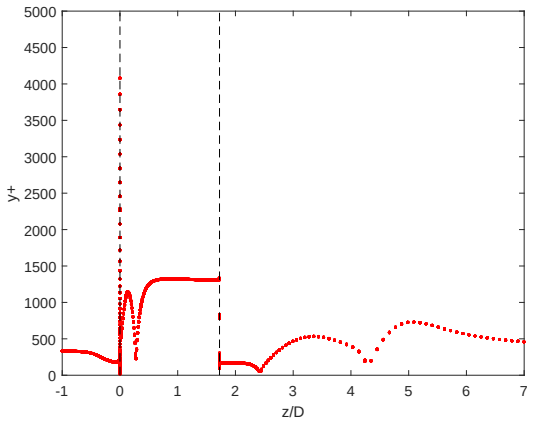

Figure 4.3: y^+ value on the cells closest on the walls for the conventional bypass pig model

the liquid is moving with 2 m/s and the pig is driven by the mixture of gas and liquid, with a velocity of 5 m/s. Thus, in the reference frame of the pig, the gas phase flow moves with 3 m/s, the liquid phase flow moves with -3 m/s and the pipe wall moves with -5m/s. The negative velocity means the liquid phase flow and the pipe move from the outlet to inlet direction, as shown in Figure 3.4. The surface tension of the liquid phase and gas phase is simulated as a constant, 0.0119 N/m.

The bypass pig model used in multiphase study is a conventional bypass pig model, thus, the

Parameter	Value
Bulk velocity U	UDF
Horizontal bypass area (%)	30%
Pipe Diameter D	1.16 m
Bypass pig diameter d	0.6354 m
Upstream pipe length	$2D$
Downstream pipe length	$20D$
Horizontal bypass length	2 m
Location of the back of the pig	z=0
Holes bypass area (%)	30%
Distance between the pig body and the disk h	$0.2236D$
Disk diameter H	$0.7071D$
Holes inner diameter dh	$0.6708D$
Disk thickness t	$0.07071D$
Number of holes n	4
Angle of hole ω	45^o
Density ρ	68 kg/m^3
Viscosity μ	2.264 E-5 kg/ms
Reynolds number R_e	1 E+7

Table 4.2: Key parameters govern the complex bypass pig geometry used in the mesh independent study

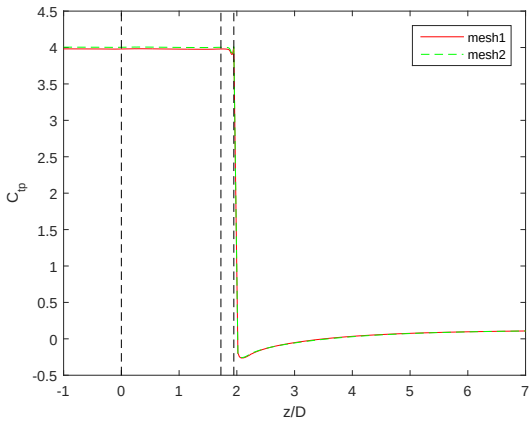

Figure 4.4: Total pressure coefficient distribution on the centreline for the complex bypass pig mesh independence study

valid mesh settings from Section 4.1.1 can still be used in this study. For the mesh independent study, two meshes with 1,766,172 elements and 2,692,000 elements, respectively, are generated. The two models with different mesh settings run with the time step size 0.001 s, which is suggested by Singh and Henkes[18]. For the time step size independence study, a smaller time step size is further tested. The time step size independent study is based on the time step size 0.0002 s. For the multiphase study, the volume fraction of liquid is the variable we are most interested in.

Figure 4.7 shows the volume fraction of liquid contour for three models involved in this independent study, after running the model 1 second. The left figures (Figures 4.7a, 4.7c and 4.7e) show

Parameter	Value
Gas velocity U_{gas}	3 m/s
Liquid velocity U_{liquid}	-3 m/s
Pipe wall velocity U_{wall}	-5 m/s
Bypass area (%)	4%
Pipe Diameter D	1.16 m
Bypass pig diameter d	0.232 m
Upstream pipe length	$15D$
Downstream pipe length	$25D$
Pig length	2 m
Location of the back of the pig	z=0
Density of gas ρ_{gas}	41.5 kg/m^3
Density of liquid ρ_{liquid}	750 kg/m^3
Viscosity of gas μ_{gas}	1.20 E-5 kg/ms
Viscosity of liquid μ_{liquid}	0.0005 kg/ms
Surface tension	0.0119 N/m
Liquid hold up	0.3

Table 4.3: Key Parameters govern the bypass pig geometry used in the multiphase mesh & time step size independent study

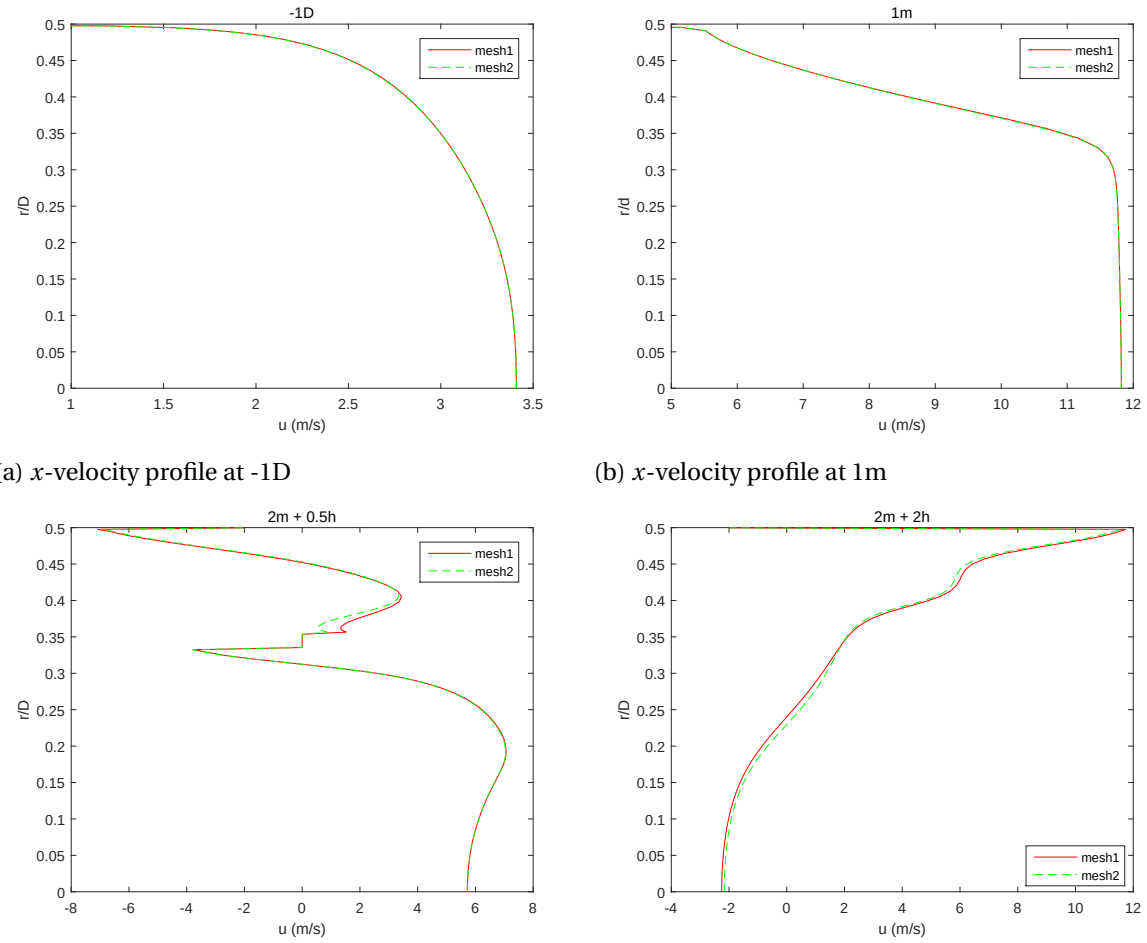

(a) x-velocity profile at -1D

(b) x-velocity profile at 1m

(c) x-velocity profile at 2m + 0.5h

(d) x-velocity profile at 2m + 2h

Figure 4.5: Velocity profiles for the complex bypass pig mesh independent study

the volume fraction of liquid contour on the cross section plane. The right figures (Figures 4.7b, 4.7d and 4.7f) show the volume fraction of liquid contour on the section plane in the downstream pipe, which is at the position $x = 2.6m$. Figure 4.7 shows the volume fraction of liquid contours, the red colour represents the liquid phase and the blue colour represents the gas phase.

The flow behaviour is extremely complex in the bypass pig model, especially in the region at the beginning of the downstream pipe. We can observe the liquid hold up in the beginning of the downstream pipe, and the bypassed gas passes through the liquid hold up, from these figures. In general, there are three levels of fluids after the bypass region (as shown in Figure 4.7b, 4.7d and 4.7f) after 1 second. In the bottom there is the liquid flow, the liquid slug flow is in the top region and the bypassed gas which passes through the liquid slug is in the middle region. In the three cases tested at here (two simulations for mesh independence study and one additional simulation for time step size independence study), the flow behaviours are very similar.

Figure 4.8 and 4.9 show the volume fraction of liquid and velocity's distributions on the centre-line. Unlike the single phase studies, the results from multiphase simulations are extremely complex, thus the variables' distribution on a certain line are very sensitive, which can be found on

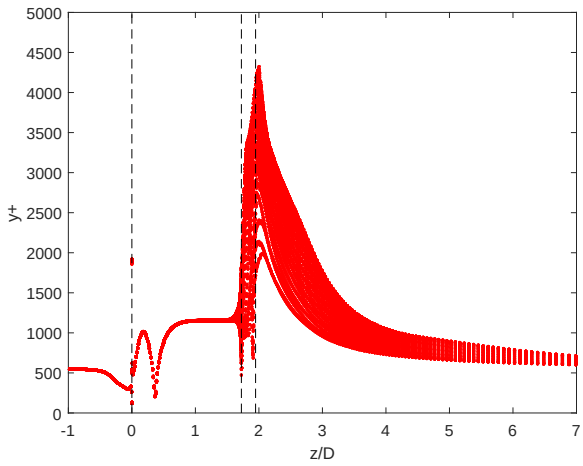

Figure 4.6: y^+ value on the cells closest on the walls for the complex bypass pig CFD model

these figures. In these figures, we find that for both the mesh independence study and the time step size independence study, the peaks of volume fraction of liquid (as shown in Figure 4.8)velocity (as shown in Figure 4.9) are in similar positions.

Thus, based on the multiphase mesh and time step size independent studies, the mesh with 1,766,172 elements and the time step size 0.001 s are chose for the further multiphase studies.

4.3. UDF BOUNDARY CONDITIONS

As discussed in Section 3.3, we use the fully developed pipe flow's profiles as the boundary conditions of the bypass pig CFD models through UDF (user defined functions) approach, since it provides more realistic boundary conditions, and saves a lot of computational resources. This section deals with the validation of the UDF boundary conditions modelling approach. We first compare the fully developed pipe flow's velocity profiles with theory, moreover we compare results from UDF boundary conditions simulations with simulations with uniform boundary conditions. This validation is based on the disk pig, as flow's behaviour around the disk pig is relatively more complex. Also, the complex bypass pig geometry is based on the disk pig. The parameters which govern the disk pig geometry used in this study are summarized in Table 4.4

4.3.1. FULLY DEVELOPED PIPE FLOW'S VELOCITY PROFILE

We achieve fully developed pipe flow's profiles through one CFD simulation for a 100 meters pipe. Figure 4.10a shows the x-velocity distribution on the centreline for the 100 meters pipe. From this figure, we find that the velocity profile is not changing after 75 meters, which means the pipe flow is fully developed after 75 meters entrance length, and this result matches Equation 2.20.

Figure 4.10b shows the velocity profile on different positions in x direction: 15m, 30m, 95m. The blue line (15m) and green line (30m) show the velocity profiles in the hydrodynamic entrance region, and the red line shows the velocity profile in the fully developed region.

We recall the log low which was introduced in Section 3.2.2, in theory the velocity profile for the

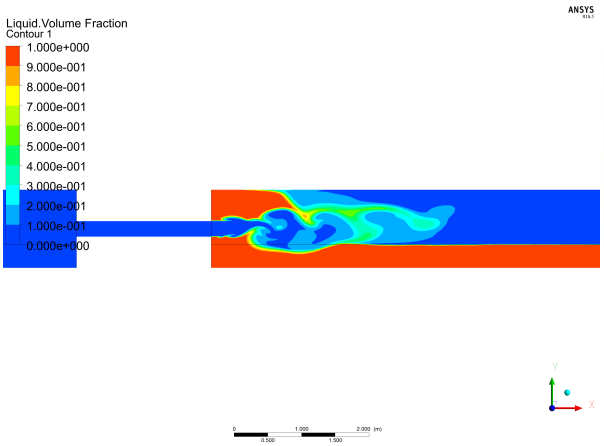

(a) 1st mesh with 0.001 s time step size: cross section

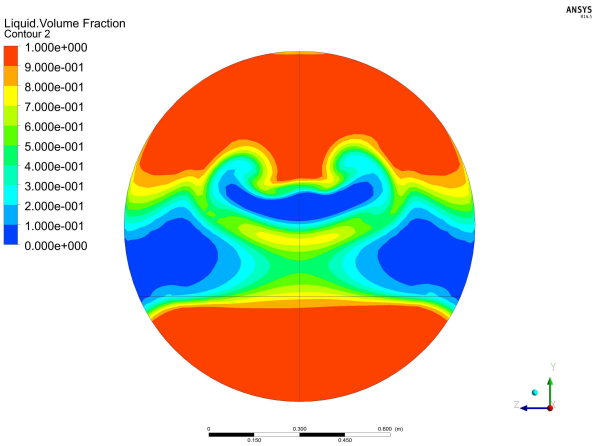

(b) 1st mesh with 0.001 s time step size: downstream pipe section

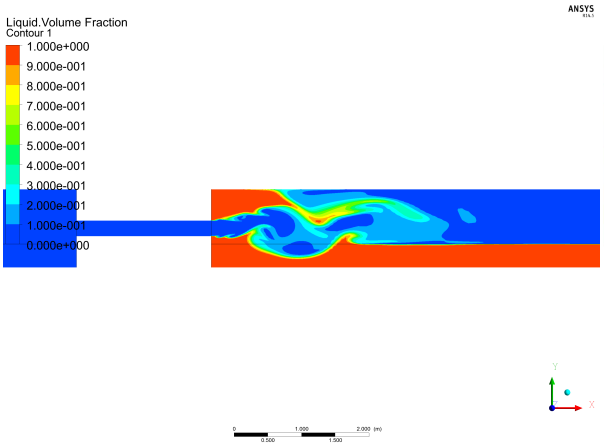

(c) 2nd mesh with 0.001 s time step size: cross section

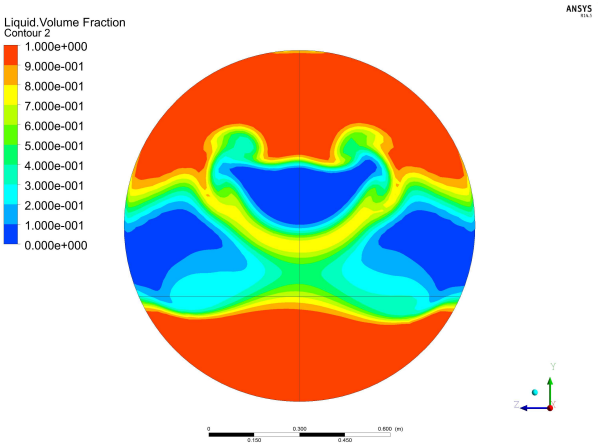

(d) 2nd mesh with 0.001 s time step size: downstream pipe section

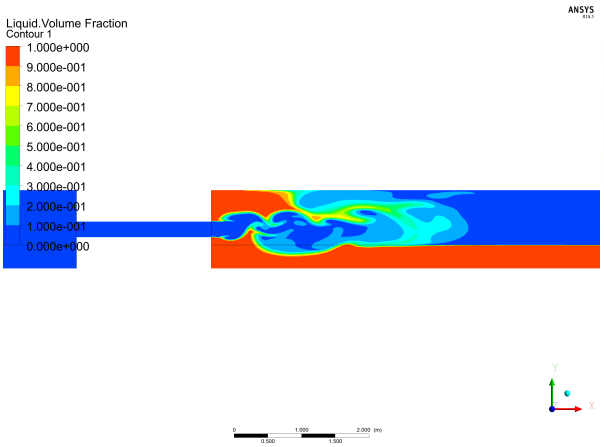

(e) 1st mesh with 0.0002 s time step size: cross section

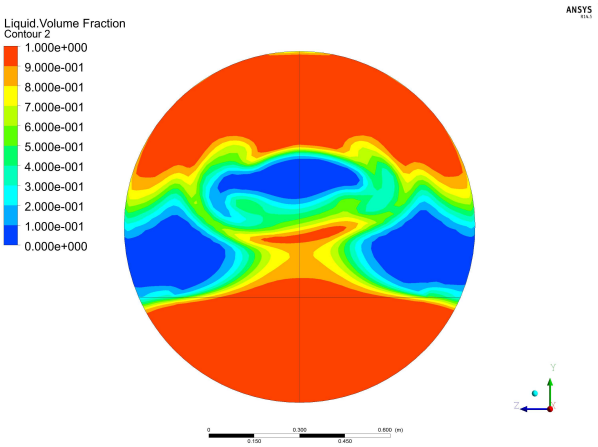

(f) 1st mesh with 0.0002 s time step size: downstream pipe section

Figure 4.7: Volume fraction of liquid contours on the cross section and the downstream pipe section plane, after $t = 1s$, for the mesh & time step independence study of the multiphase study

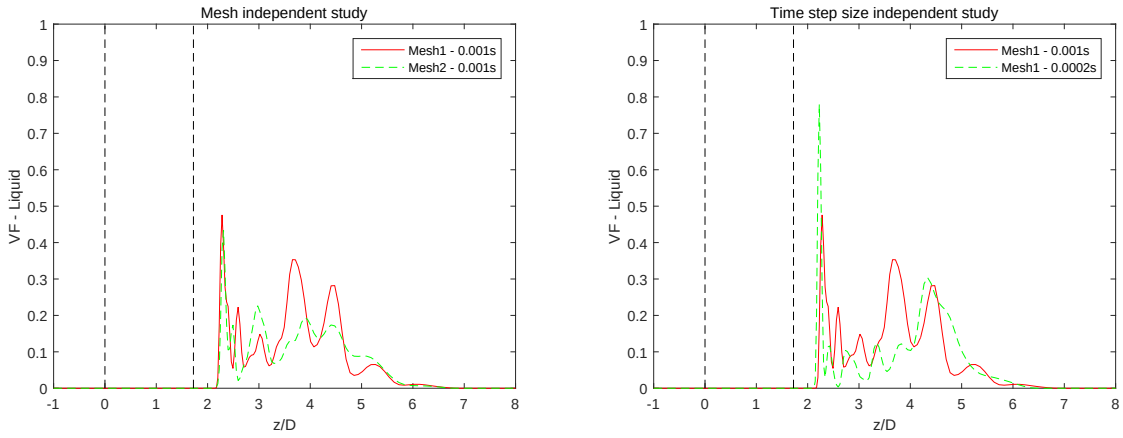

(a) Mesh independent study

(b) Time step size independent study

Figure 4.8: Volume fraction of liquid's distribution on the centreline for the mesh & time step independence study of the multiphase study

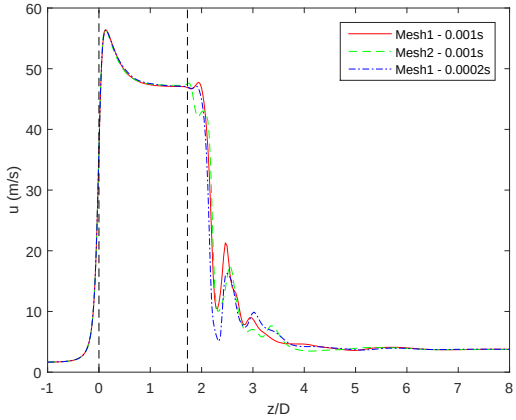

Figure 4.9: x-velocity's distribution on the centreline for the mesh & time step independence study of the multiphase study

fully developed profile can be expressed as:

$$u^+ = \frac{1}{\kappa} \ln y^+ + B \tag{4.1}$$

Where y^+ and u^+ are the dimensionless distance and dimensionless velocity, which can be calculated by Equation 3.10 and 3.11. Figure 4.11a shows the mean velocity profiles in fully developed turbulent pipe flow. And Figure 4.11b shows the velocity profiles at 15 m, 30 m and 95 m, from the CFD simulation of the 100 m pipe.

Pope[28] suggested two groups of constants:

$$\kappa = 0.41,\ B = 5.2$$

And

$$\kappa = 0.436,\ B = 6.13$$

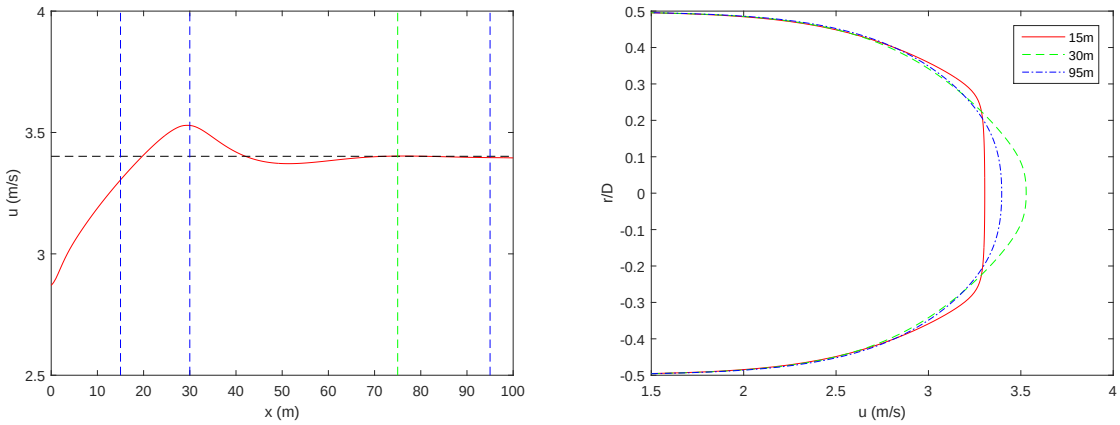

(a) X-velocity distribution on the centreline

(b) Velocity profile at different position

Figure 4.10: Results of the 100 m pipe pipe CFD study

for the log law (Equation 4.1), to predict the fully developed pipe flow's velocity profile. The log law with two groups constants is plot on Figure 4.11 as the solid line and the dashed line. In Figure 4.11a, the symbols represent experimental data at six Reynolds numbers ($Re = 3.2E+4$, $9.9E+4$, $4.09E+5$, $1.79E+6$, $7.71E+6$ and $2.99E+7$), and it can be found that the log law with two groups of constants can predict the velocity profile of fully developed pipe flow in various Reynolds numbers Re.

The fully developed pipe flow's profile we achieve from the pipe CFD simulation is shown in Figure 4.11b, and the velocity profile is represented as the red points. From this figure, we find that most of the CFD results are located on the straight lines, which represent the theoretical log law. It

Parameter	Value
Bulk velocity U	2.87 m/s
Horizontal bypass area (%)	10%
Disk bypass area (%)	8%
Pipe Diameter D	1.16 m
Bypass pig diameter d	0.3668 m
Upstream pipe length	$5D$
Downstream pipe length	$20D$
Pig length	2 m
Location of the back of the pig	z=0
Distance between the pig body and the disk	h=0.06303D
Disk diameter	H = 0.396D
Disk thickness	t = 0.00862D
Density ρ	68 kg/m^3
Viscosity μ	2.264 E-5 kg/ms
Reynolds number R_e	1 E+7

Table 4.4: Key Parameters govern the disk pig geometry used in the UDF boundary conditions validation study

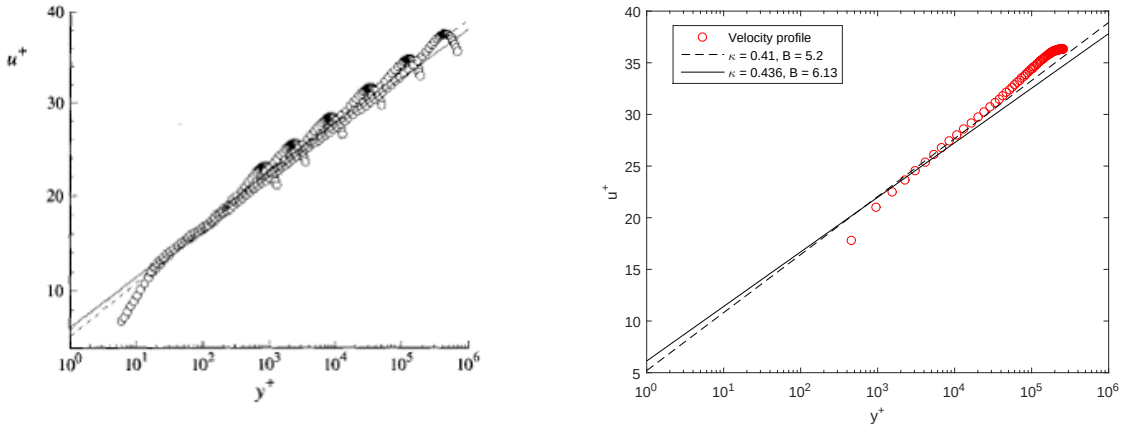

(a) Mean velocity profiles in fully developed turbulent pipe flow, reproduced from [28]

(b) Fully developed pipe flow's velocity profile from the CFD simulation

Figure 4.11: Fully developed pipe flow's velocity profiles

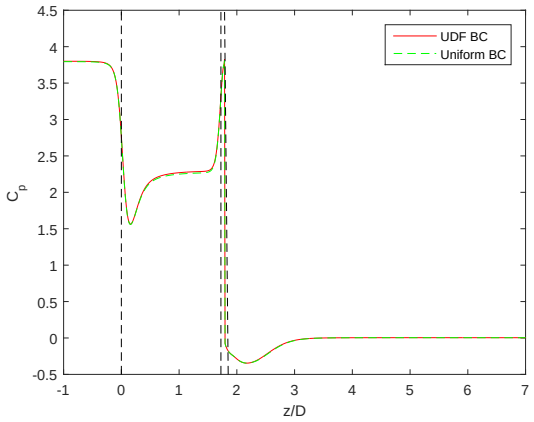

Figure 4.12: Total pressure coefficient distribution on the centreline for the UDF boundary conditions validation

indicates that the pipe flow we used to set as the boundary conditions of the bypass pigs models is in fully developed condition.

4.3.2. UDF BOUNDARY CONDITIONS VALIDATION

In this part, the UDF boundary conditions approach is validated, by comparing the results achieved from this approach with the CFD simulation with uniform boundary conditions.

Figure 4.12 shows the total pressure coefficient distribution on the centreline, for the two cases:

- The model with UDF boundary conditions, which are set as the fully developed pipe flow's profiles.
- The model with uniform boundary conditions, which were discussed in Section 3.1.

From Figure 4.12, we find the overall pressure drop are unchanged if we use the UDF boundary conditions instead of the uniform boundary conditions. This is because the overall pressure drop is

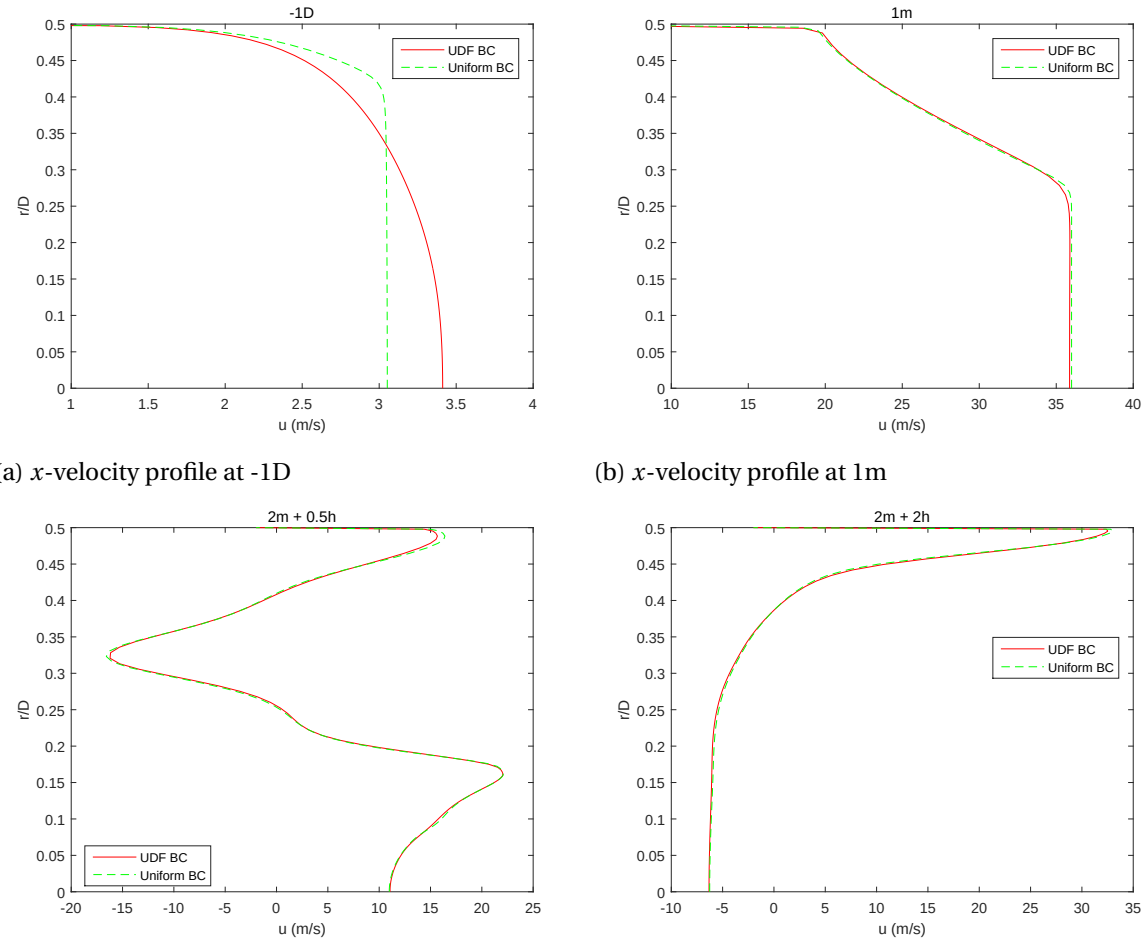

(a) x-velocity profile at -1D

(b) x-velocity profile at 1m

(c) x-velocity profile at 2m + 0.5h

(d) x-velocity profile at 2m + 2h

Figure 4.13: x-velocity profiles for the UDF boundary conditions validation

mostly dependent on the mass flow rate of flow, which passes through the bypass regions. Thus, we further compare the detailed flow behaviour around the disk pig, achieved from simulations with two boundary conditions approaches.

Figure 4.13 shows the velocity profiles on different positions in x direction. Figure 4.13a shows the velocity profile in the inlet pipe, Figure 4.13b shows the velocity profile in the bypass pig, Figure 4.13c shows the velocity profile in the region between the bypass pig and the disk, and Figure 4.13d shows the velocity profile in the outlet pipe. From these velocity profiles, we find that the flow behaviour is only different in the inlet pipe. On Figure 4.13a, the green line shows the velocity profile in the inlet pipe for the uniform boundary conditions case, and we can see the front of the velocity profile is still flat, which means the pipe flow is still developing in the inlet pipe. On the other hand, the velocity profile for the UDF boundary conditions case (red line) is in fully developed condition.

Figure 4.12 and 4.13 prove that: even similar results can be achieved by using two different approaches, the simulations with UDF boundary conditions can simulate more realistic conditions for the bypass pigs. More importantly, for instance for the disk pig case, the UDF boundary conditions approach decreases the upstream pipe length from $5D$ to $2D$, and decrease the cells number from

7,308,038 to 5,386,934, thus almost 25% of the computational resource can be saved by using this modelling approach.

4.4. SUMMARY

In this chapter, the modelling approaches and the numerical models for the bypass pig studies are validated, through various studies.

First of all, the mesh independent study is performed, to make sure that the numerical solutions are independent on the mesh. As the multiphase study is based on transient simulations, the time step size independent study is performed, to make sure that the solutions are independent on the time step size setting also.

As discussed in Chapter 3, for the single phase studies we use the fully developed pipe flow's profiles as the UDF boundary conditions, and this modelling approach is then validated in this chapter. First of all, the mean velocity profile achieved through the pipe CFD study is compared with the theory. It is found that the pipe flow is in fully developed condition. Also, this modelling approach is validated by comparing the results from the simulations with the fully developed boundary conditions and the simulations with uniform boundary conditions. It is found that this modelling approach gives more realistic boundary conditions, and saves a lot of computational resources.

5

RESULTS OF DISK PIG STUDY

This chapter deals with results from the disk pig study. The flow around the disk pig has already been studied by Korban[19]. In that research, the relation between the pressure loss coefficient K and the parameters which govern the disk pig model, is investigated. However, the general correlation to predict the pressure loss coefficient K for the disk pig is not given. Thus, in the present research, the flow around the disk pig is further investigated. Table 4.4 summarizes the key parameters to govern the disk pig model. In different studies, the parameters are slightly changed, which will be discussed in each study.

In this chapter, first of all the flow features of the disk pig are presented. During the disk pig study, two different flow behaviours around the disk pig are observed, and the investigation of the two flow behaviours is carried out secondly. Finally, different parameter studies are carried out, in order to study the relation between the pressure loss coefficient K and the governing parameters of the disk pig model.

5.1. FLOW FEATURES OF DISK PIG

This section deals with the detailed flow features around the disk pig.

Figure 5.1 shows the streamlines that represent the mean flow around the disk pig. In the sudden contraction region, the flow behaviour is similar to the conventional bypass pig. After the horizontal bypass region, the flow moves around the disk. In the disk bypass region, the flow is shaping as a jet structure. After the disk, the main recirculation zone in the center of the downstream pipe.

In general, two different flow behaviours around the disk pig are observed during the disk pig study. Figure 5.1a shows one of the flow behaviours observed. In the disk bypass region, a jet is formed. After the jet moves out of the disk bypass region, it contacts the pig wall first. Then, the jet moves along the pig wall and the pipe wall to the downstream pipe. There is a recirculation zone between the jet and the pig wall. In the downstream pipe, the main recirculation zone is under the jet, which contacts the pipe wall.

Figure 5.1b shows another flow behaviour around the disk pig observed. After the disk bypass region, the jet does not contact the pig wall, but contacts the downstream pipe wall directly. Thus,

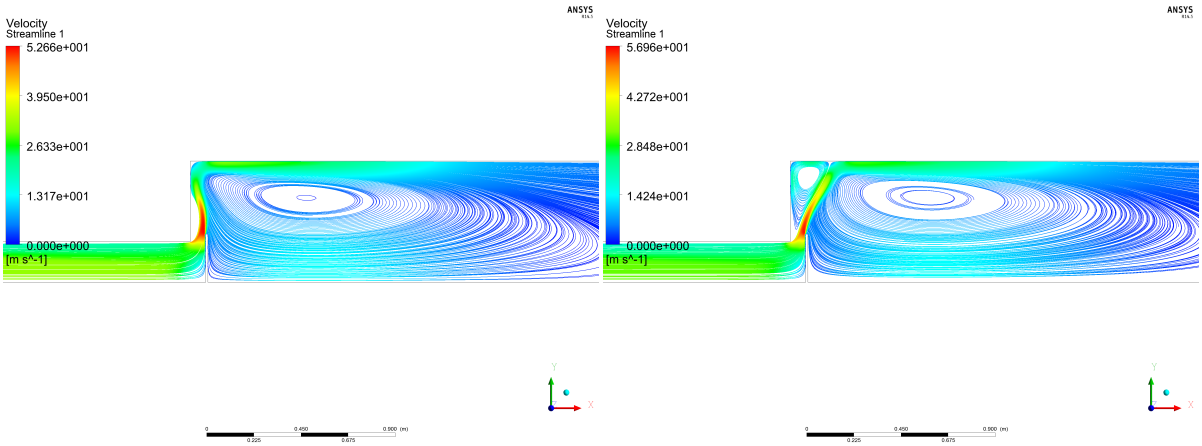

(a) Behaviour A (b) Behaviour B

Figure 5.1: Streamlines of the flow around the disk pig

the recirculation zone between the pig body and the jet is at the corner of the pig wall and the downstream pipe wall. The main recirculation zone is still in the center of the downstream pipe.

In this research, we name the flow behaviour shown in Figure 5.1a as “flow behaviour A”, and name the flow behaviour shown in Figure 5.1b as “flow behaviour B”. Figure 5.1 shows the two flow behaviours around a disk pig with the same governing parameters, and the investigation of the two flow behaviour around the disk pig will be presented in Section 5.2. The biggest difference between these two flow behaviours is the shape of the jet, and it is influenced by the recirculation zone between the pig body and the jet it self. This recirculation zone’s influence on the shape of the jet will be investigated in Section 5.3.4.

Figure 5.2 shows the velocity contour of the disk pig with two different flow behaviours. The two different flow behaviours, especially the shape of jet, can also be shown clearly on these figures. In both cases, the maximum velocity is in the position that the jet contacts the top of the disk. In the upstream and downstream pipe, the flow moves with the bulk velocity U, but in the main recirculation zone in the downstream pipe, the velocity is higher than around.

In this research, the pressure loss coefficient K is one of the most important quantities we are interested in . It is found that the overall pressure drop will increase when the flow behaviour changes from behaviour A to B (in this case the pressure increases with 30%), as shown in Figure 5.3. Thus, the driving force of the disk pig (which is the overall pressure drop of the disk pig) is strongly dependent on the flow behaviour around it.

Figure 5.4 shows the total pressure contour for two disk pig flow behaviours. Combine these figures with the total pressure coefficient C_{tp}’s distribution on the centreline (Figure 5.3), we find that most of the total pressure loss comes from the disk bypass region. The total pressure contour for the flow behaviour A is shown in Figure 5.4a, and the lowest total pressure is in the recirculation zone between the jet and the pig body. For the flow behaviour B, the total pressure contour is shown in Figure 5.4b, and the lowest total pressure is in the recirculation zone in the corner of pig body and pipe wall. In the recirculation zones, the static pressure is lower than around. Also, the velocity in the recirculation zones is relatively small, and leading low dynamic pressure. Thus, in the recirculation

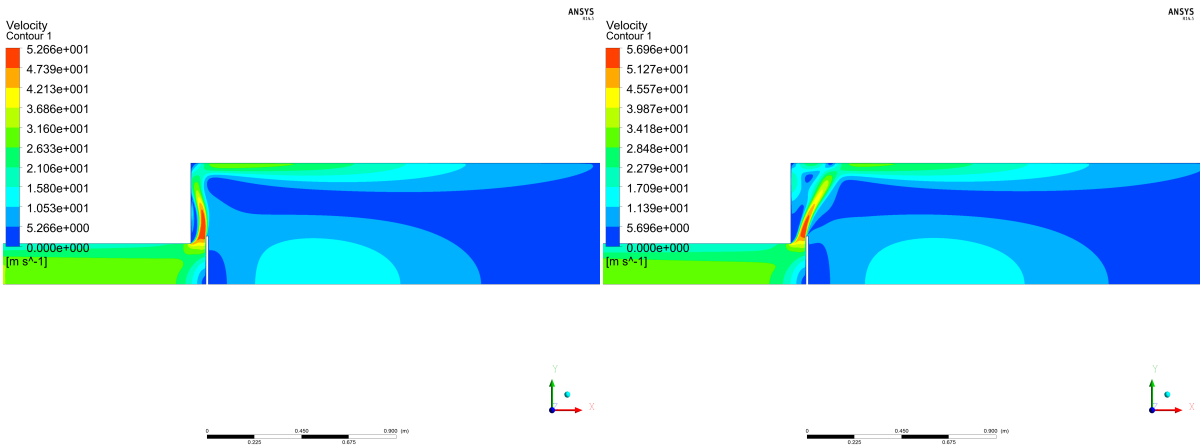

(a) Behaviour A (b) Behaviour B

Figure 5.2: Velocity contours of the flow around the disk pig

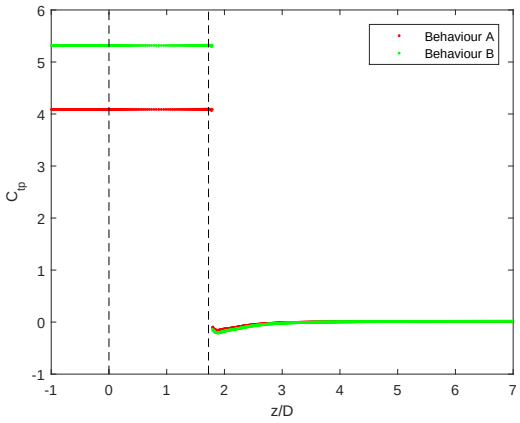

Figure 5.3: Total pressure coefficient's distribution on the centreline of the disk pig study

zones the total pressure is lower than the region around it. The core region of the main recirculation also has a relatively low total pressure, which is shown in Figure 5.4b clearly.

Figure 5.5 shows the turbulence intensity contour for two disk pig flow behaviours. From these figures, we find that the maximum turbulence intensity is in the edge of the jet, around 10 m/s in both cases. Along the jet the turbulence intensity drops down quickly, and becomes low again in the downstream pipe.

5.2. INVESTIGATION OF THE TWO NUMERICAL SOLUTIONS

During the disk pig study, two completely different flow behaviours around the disk pig are observed. Most importantly, the pressure drop across the disk pig, which is the driving force of the bypass pig's motion in the pipeline, is strongly dependent on the flow behaviour around it. Thus, in this section the two flow behaviours, which come from two different numerical solutions, are further investigated.

During the disk pig study, it is found that the flow behaviour around the disk pig is dependent

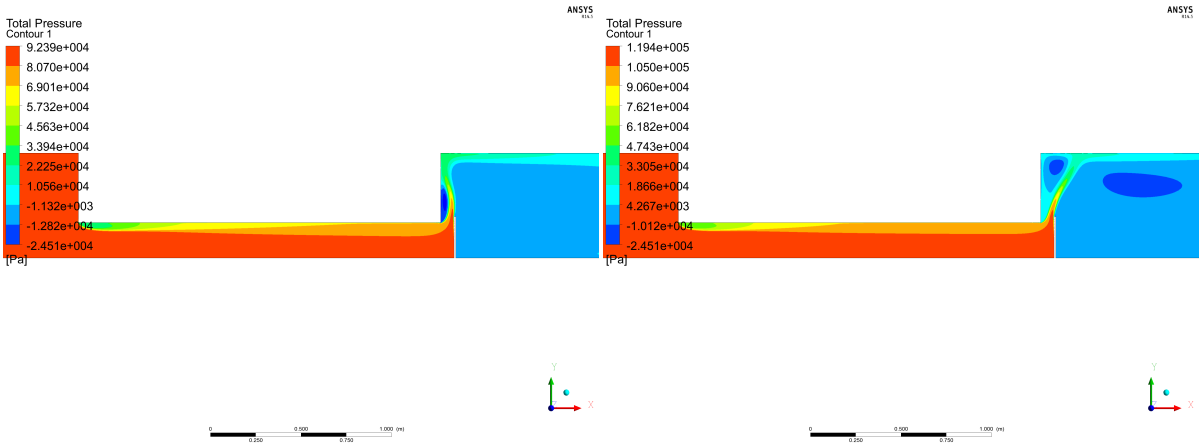

(a) Behaviour A (b) Behaviour B

Figure 5.4: Total pressure contours of the flow around the disk pig

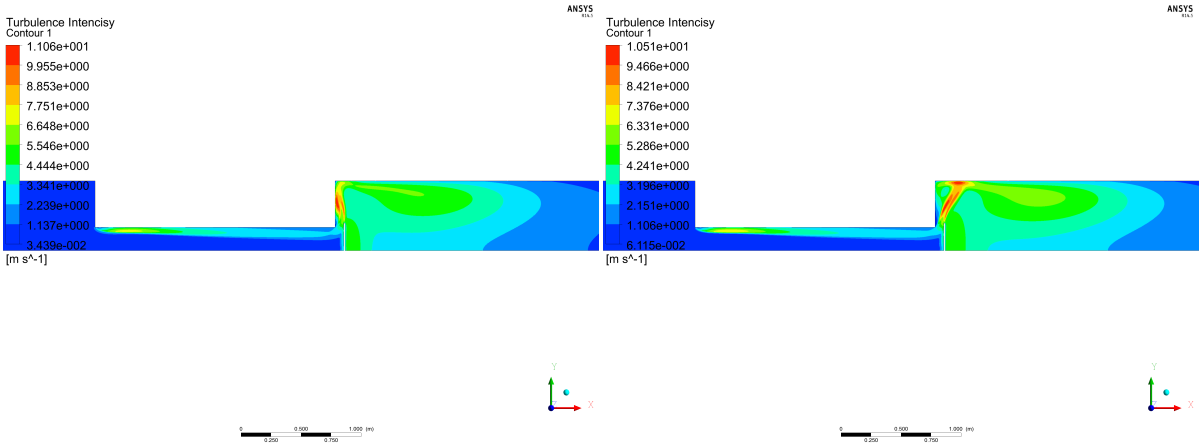

(a) Behaviour A (b) Behaviour B

Figure 5.5: Turbulence intensity contour for two disk pig flow behaviours

on the numerical solution approaches. For instance, the flow behaviours shown in Figure 5.1 come from the same disk pig model. In this disk pig model, the other parameters are same as summarized in Table 4.4, and we increase the horizontal bypass area from 10% to 11.3 %, which means increase the parameter bypass pig diameter d from 0.3668 m to 0.3899 m. The flow behaviour A, as shown in Figure 5.1a, comes from the steady state simulation, and in this case the default initialization scheme of Fluent is used to initialize the numerical model.

In order to validate the assumption that the flow around the disk pig is in steady state, the same CFD model is ran as transient simulation, and we find that the solution is stable after some time. If we run the solution from the transient simulation into steady state again, we find that the solution is stable (not changing) during the simulation, which means the solution from the transient simulation is still in steady state. However, in this numerical solution, the flow around the disk pig behaves as the behaviour B, as shown in Figure 5.1b.

Thus, for a disk pig model with certain governing parameters, two completely different numer-

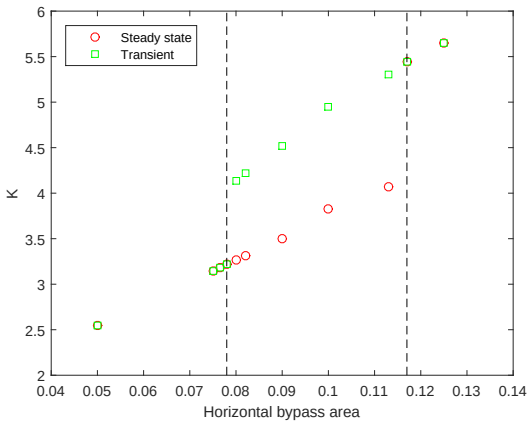

Figure 5.6: Pressure loss coefficient as a function of horizontal bypass area for the disk pig parameters study, results from steady state and transient simulations

ical solutions can be achieved, and both of the solutions are in steady state. Which behaviour the flow around the disk pig behaves is determined by the initial conditions of the steady state numerical simulation:

- The flow behaviour A comes from the steady state simulation, in this case the numerical model is initialized by the default initialization scheme of Fluent.
- The flow behaviour B comes from the steady state simulation in which the initial conditions are the solution we achieved through running the CFD model in transient after some time.

Furthermore, we change the parameters which govern the disk pig model, to investigate how the numerical solutions are related to the disk pig geometry. This study will be introduced as the horizontal bypass area parameter study for the disk pig in Section 5.3.1. In this study, we change the dimensionless parameter $(d/D)^2$ from 5% to 12.5%, and run the CFD models with different initial conditions of the steady state simulation.

Figure 5.6 summarizes all the results from two simulations with two numerical approaches. The red points represent the results from steady state simulations, in which the numerical model is initialized by Fluent's default initialization scheme. On the other hand, the green points represent the solutions come from the simulations with the initial conditions as the solutions firstly achieved from transient simulations.

From this study, we actually find in the region:

$$7.8\% < (\frac{d}{D})^2 < 11.3\%$$

Two different solutions with completely different flow behaviours around the disk pig can be achieved, and the final numerical solution is determined by the initial conditions of the CFD simulation.

Moreover, in the region where horizontal bypass area is smaller than 7.8%, the flow always behaves as the behaviour A; and in the region that the horizontal bypass area is larger than 11.3%, the flow always behaves as the behaviour B. In this Figure, it is found that for the same disk pig geometry, the flow behaviour B causes a higher overall pressure drop than the behaviour A.

5.3. PARAMETERS STUDY

In this section, different parameter studies are carried out, in order to study the relationship between the pressure loss coefficient K and the disk pig geometry. Moreover, the flow behaviour around the disk pig is also dependent on the parameters which govern the disk pig geometry. As shown in Table 4.4, the disk pig geometry is governed by several parameters. However, Korban[19] suggested that the flow behaviour and the pressure loss coefficient for disk pig are mainly dependent on three parameters: bypass pig diameter d, diameter of disk D and distance between the pig body and disk h. Similar conclusion is also suggested by Idelchik's correlation for disk valve (Equation 2.28). Furthermore, the influence of the downstream pipe diameter on the flow behaviour around the disk pig is investigated in this section.

Thus, four parameter studies for the dimensionless groups:

- Horizontal bypass area: $(\frac{d}{D})^2$
- Disk height: $\frac{H}{D}$
- Disk bypass area: $\frac{4d \cdot h}{D^2}$
- Downstream pipe diameter: D^*/D

as introduced in Section 2.2, are performed in this section.

As discussed in Section 2.4.7, the pressure loss coefficient for conventional bypass pig K_{conv} can be calculated by the combination of one sudden contraction and one sudden expansion. Similarly, we assume for the disk pig, the pressure loss coefficient K_{dp} can be calculated by the combination of the correlation for the sudden contraction (Equation 2.23) and for the disk valve (Equation 2.28). This assumption can be expressed as:

$$K'_{dp} = K'_c + K'_{dv} = 0.5(1 - \frac{d^2}{D^2})^{3/4} + 2\frac{H}{d} + \frac{0.155d^2}{h^2} - 1.85 \tag{5.1}$$

Where K'_c and K'_{dv} represent pressure loss coefficient in sudden contraction and disk valve. In different parameter studies, the results calculated by Equation 5.1 are compared with the CFD results.

5.3.1. HORIZONTAL BYPASS AREA

As discussed before, for the disk pig model with the horizontal bypass area $(\frac{d}{D})^2$ is equal to 11.3%, if the numerical model is ran in steady state, the flow behaviour is observed as the flow behaviour A, as shown in Figure 5.1a; on the other hand, if the model is ran as transient simulation, the flow behaviour B, as shown in Figure 5.1b, is observed[1].

The parameter study for the dimensionless parameter horizontal bypass area $(d/D)^2$ is carried out. In the initial model, $(d/D)^2$ = 10%, and in this study we change the $(d/D)^2$ from 5% to 12.5%, in both numerical approaches as discussed in Section 5.2. In general, it is found that in the disk pig

[1] As discussed before, we actually run the solution from transient simulation into steady state again, thus, this solution is also in steady state, and the different steady state solutions come from the initial conditions for steady state simulations

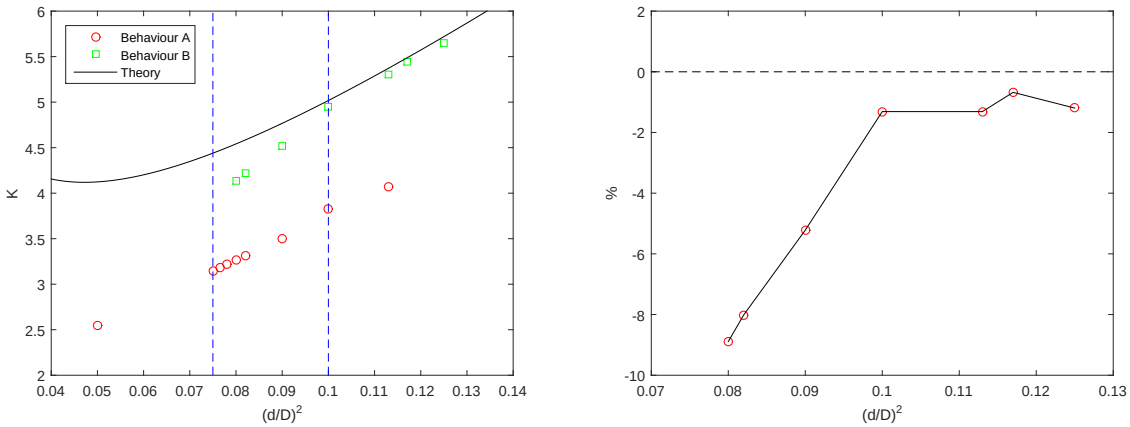

(a) Pressure loss coefficient as a function of horizontal bypass area in different flow behaviours

(b) Deviation of the theory from the CFD results for the behaviour B

Figure 5.7: Theory compared with CFD results, for the disk pig horizontal bypass area parameter study

CFD model the flow behaviour A appears if the dimensionless group $(\frac{d}{D})^2$ is relatively small, and the flow behaviour B appears when $(\frac{d}{D})^2$ is relatively large.

Figure 5.7 compares the results calculated by Equation 5.1 and the results from CFD simulations. For the CFD results, the red points show the results from solution while the flow around the disk pig behaves as the behaviour A and the green points represents the solutions with flow behaviour B. In general, we find that Equation 5.1 can calculate the pressure loss coefficient K'_{dp} when the flow around the disk pig behaves as the behaviour B accurately. Figure 5.7b only shows the deviation of Equation 5.1 from the CFD results with the flow behaviour B. When the horizontal bypass area d^2/D^2 is lower than 9%, the error is relatively large, around 7%, but still in acceptable range. And when the parameter d^2/D^2 is larger than 10%, the errors are within 1%.

It is noticed that Equation 2.28 for disk valve is valid in a certain range in theory, as shown in Figure 5.7a as the blue dashed lines. However, based on the CFD results, we find that this equation still can calculate the pressure loss coefficient for disk pig even out of this range.

5.3.2. DISK DIAMETER

Another parameter which has influence of the flow around the disk pig is the disk diameter H, thus, in this part the parameter study for the dimensionless parameter disk height H/D is performed. In the initial model, $H/D = 0.396$, and in this parameter study, we keep the other parameters fixed and change the H/D from 0.325 to 0.55. The results calculated by Equation 5.1 are also being compared with the CFD results.

Figure 5.8 shows the pressure loss coefficient K_{dp} as a function of the disk height H/D. The red points represent the results from solutions behave as the flow behaviour A, and the green points represent the flow behaviour B. It is found that when the disk has relatively small disk height (when $H/D < 0.35$), the flow around the disk pig behaves as the behaviour B, and when the dimensionless group $H/D > 0.375$, the flow around the disk pig changes to behaviour A.

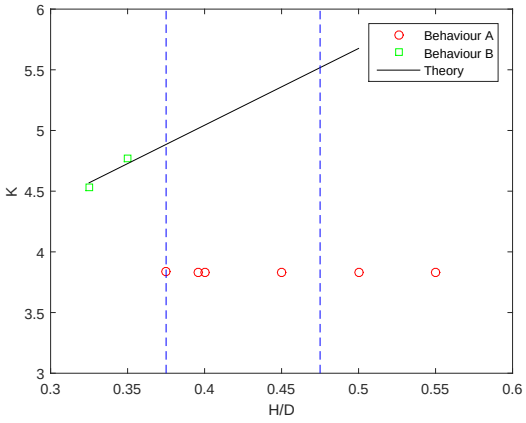

Figure 5.8: Pressure loss coefficient as a function of disk diameter for the disk pig parameters study, with different flow behaviours

In Figure 5.8, the results calculated by Equation 5.1 is represented by the black solid line. Similar as being introduced in Section 5.3.1, it is found that Equation 5.1 can calculate K_{dp} accurately if the flow around the disk pig behaves the behaviour B. Unfortunately, in this parameter study, we only have two points which can be compared with Equation 5.1, as the disk diameter D has to be larger than the diameter of the horizontal bypass region $d = 0.316D$; on the other hand, the flow around disk pig changes to behaviour B when H/D is larger than 0.375. Also, the two results are actually not in the valid range for Equation 2.28, which is represented by the blue dashed lines. However, it is found that Equation 5.1's results match the CFD results, as the errors for both two points at H/D = 0.325 and 0.35 are within 1%.

When H/D is larger than 0.375, while the flow around the disk pig behaves as the behaviour A, the pressure loss coefficient K_{dp} is a constant 3.83, which means the overall pressure loss in disk pig is not changing when we increase the disk diameter D.

5.3.3. DISK BYPASS AREA

Furthermore, the parameter study of the dimensionless group disk bypass area $4d \cdot h/D^2$ is carried out at here. In this parameter study, we keep the other parameters fixed, and change the parameter distance between the pig body and the disk h, in order to change the dimensionless parameter disk bypass area $4d \cdot h/D^2$ from 6% to 20%.

Figure 5.9a shows the pressure loss coefficient for disk pig K_{dp} as a function of the disk pig bypass area $4d \cdot h/D^2$. The red points represent the results from solutions behave as the flow behaviour A, and the green points represent the flow behaviour B. It is found that when the parameter h is relative small (when $4d \cdot h/D^2 < 10\%$), the flow around the disk pig behaves as the flow behaviour A, and when $4d \cdot h/D^2 > 10\%$, it changes to the flow behaviour B.

In Figure 5.9a, the results calculated by Equation 5.1 is represented by the black solid line. Similar as two previous parameter studies, in this case Equation 5.1 can still calculate K_{dp} when the flow around the disk pig behaves as the flow behaviour B accurately. Figure 5.9b shows the deviation of theory from the CFD results only for the results with flow behaviour B, and most of the errors are

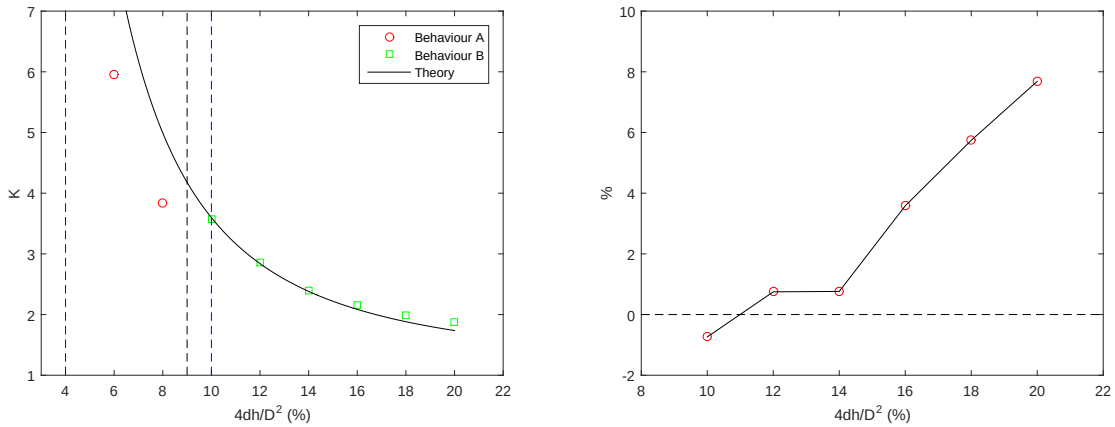

(a) Pressure loss coefficient as a function of disk bypass area with different flow behaviours

(b) Deviation of the theory from the CFD results for the behaviour B

Figure 5.9: Theory compared with CFD results, for the disk pig disk bypass area parameter study

within 5%, even all the points are actually out of the valid range for Equation 5.1, as shown as the blue dashed lines.

5.3.4. DOWNSTREAM PIPE DIAMETER

In this section, the parameter study of the dimensionless parameter downstream pipe diameter D^*/D is carried out. In reality, the parameter D^*/D has to be equal to 1, however, in this research, we keep other parameters fixed, and change the downstream pipe diameter D^*/D from 1 to 2, in order to study the diameter of the downstream pipe's influence on the flow behaviour around the bypass pig. In this study, the parameters which govern the disk pig geometry are slightly different from the parameters summarized in Table 4.4, and we change the parameter h from $0.06303D$ to $0.1107D$, in order to change the dimensionless parameter disk bypass area to 14%. As discussed in Section 5.3.3, in this case, when the parameter $D^*/D = 1$, the flow around the disk pig behaves as the behaviour B, and Equation 5.1 can calculate the pressure loss coefficient K accurately.

The theoretical results calculated by Equation 5.1 are compared with the results from the CFD simulations on Figure 5.10. Figure 5.10a shows the pressure loss coefficient as a function of the downstream pipe diameter D^*/D, while the theoretical results are plot as the black solid line. It is found that that with relative small downstream pipe diameter, the flow around the disk pig behaves as the behaviour B, and it changes to the behaviour A when $D^*/D > 1.45$. Similar as the other parameter studies introduced before, Equation 5.1 can still calculate the pressure loss coefficient for the disk pig accurately, if the flow around the disk pig behaves as the behaviour B. As shown in Figure 5.10b, the maximum error is around 3%.

Idelchik [22] suggested that for the disk valve, the influence of the pipe diameter on the pressure loss coefficient is limited. In this study, it is found that the pressure loss coefficient changes 2% when we increase the dimensionless parameter D^*/D from 1 to 1.42. Thus, based on this study it is found that the diameter of the downstream pipe's influence on the pressure loss coefficient is negligible, and Equation 5.1 can calculate the pressure loss coefficient for disk pig accurately, if the flow around

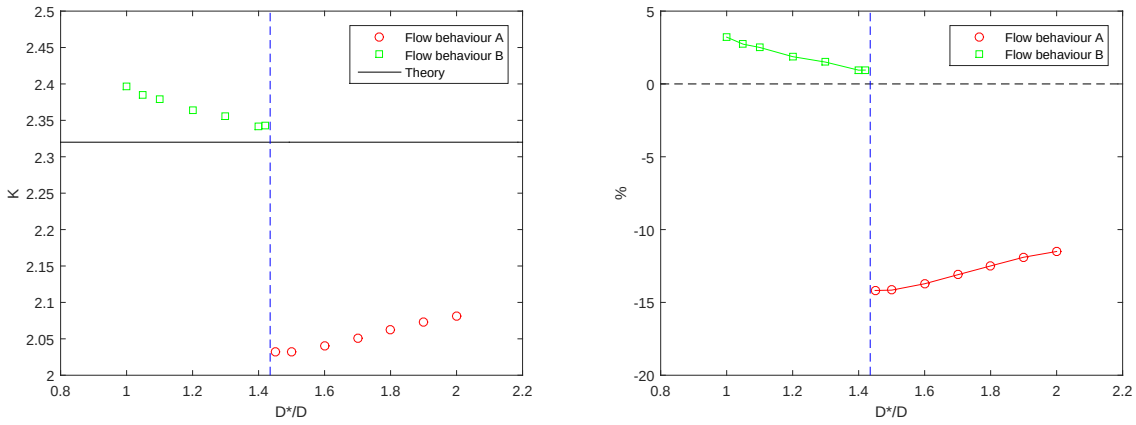

(a) Pressure loss coefficient as a function of down-stream pipe diameter (b) Deviation of the theory from the CFD results

Figure 5.10: Theory compared with CFD results, for the disk pig downstream pipe diameter parameter study

it behaves as the flow behaviour B.

Furthermore, this parameter study can help us a lot to achieve better understanding of the two flow behaviours observed around the disk pig, as introduced in Section 5.1. Figure 5.11 shows the streamlines to represents the mean flow around the disk pig, with various dimensionless parameter D^*/D. When the parameter D^*/D is smaller than 1.42, the flow around the disk pig behaves as the behaviour B, which is shown in Figure 5.11a and 5.11b; when the parameter D^*/D is larger than 1.45, the flow changes to the behaviour A, as shown in Figure 5.11c and 5.11d.

In the flow behaviour A, the jet structured flow contacts the pig wall again when it moves out of the disk bypass region, then it moves along the pig wall and the pipe wall. There is a recirculation zone between the main jet and the pig wall, the shape and height of this recirculation zone for the cases where $D^*/D = 1.45$ and $D^*/D = 2$ are same.

Thus, it is much more clear that, when the diameter of the downstream pipe is not large enough for the recirculation zone between the jet and pig body in the flow behaviour A, the recirculation zone can drive the jet structured flow to behaviour B, in which the jet contacts the pipe wall directly when it moves out of the disk bypass region, and location of the recirculation zone changes to the corner of the pig and pipe wall.

5.4. SUMMARY

In this chapter, the results from disk pig study are presented. First of all, the flow features of the disk pig are introduced in details. It is found that two different flow behaviours can be observed for flow around the disk pig, through CFD simulations (flow behaviour A as shown in Figure 5.1a and flow behaviour B as shown in Figure 5.1b). Which flow behaviour would happen around the disk pig is dependent on:

- Initial conditions of the steady state CFD simulations: For a disk pig with certain governing parameters, two steady state solutions can be achieved by CFD simulations, by different initial conditions.

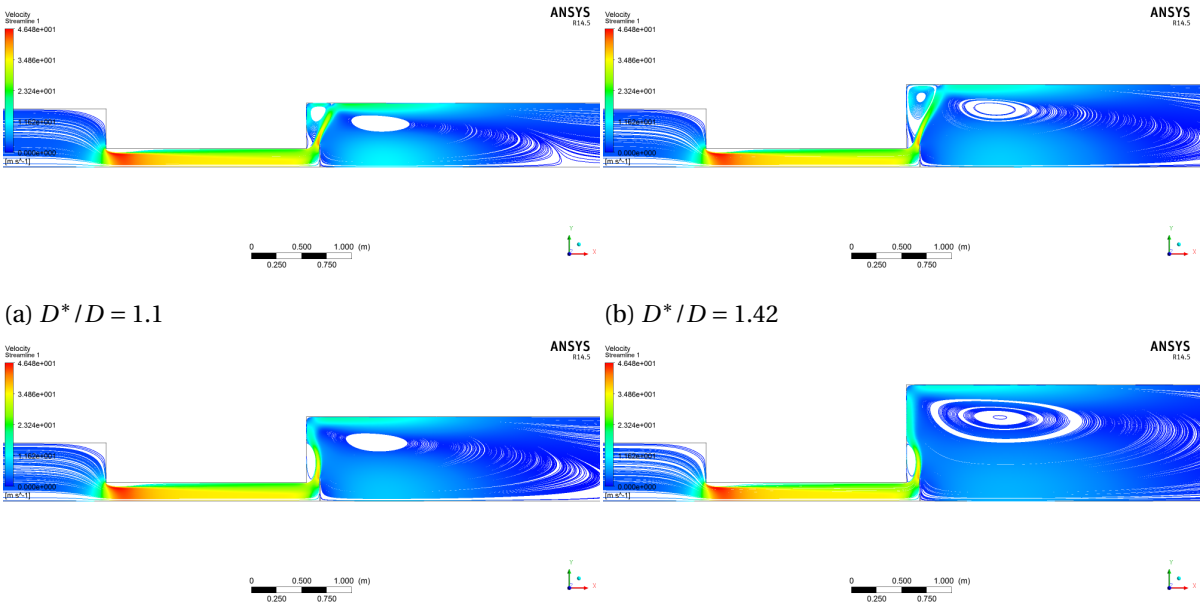

(a) $D^*/D = 1.1$

(b) $D^*/D = 1.42$

(c) $D^*/D = 1.45$

(d) $D^*/D = 2$

Figure 5.11: Streamlines of the flow around the disk pig with various downstream pipe diameter

- Parameters which govern the disk pig geometry: In general, if we increase the dimensionless groups: horizontal bypass area $(d/D)^2$ (by increasing the bypass diameter d), decrease the disk height H/D (by increasing diameter of the disk H) or increase the disk bypass area $4d \cdot h/D^2$ (by increasing the distance between pig body and disk h), the flow around the disk pig changes from behaviour A to B.

Furthermore, four parameter studies are carried out, in order to study the relationship between the pressure loss coefficient for disk pig K_{dp} and the disk pig geometry. The correlation for K_{dp}, which is inspired by the correlation to calculate the pressure loss coefficient for conventional bypass pig K_{conv} (Equation 2.30), is suggested: Equation 5.1. Based on the parameters study, it is found that Equation 5.1 can calculate the pressure loss coefficient for disk pig K_{dp} accurately, if the flow around the disk pig behaves as the flow behaviour B (which is shown in Figure 5.1b).

6

RESULTS OF COMPLEX BYPASS PIGS STUDY

This chapter deals with results from the complex bypass pig study. The complex bypass pig is another type bypass pig which is investigated in this research, and its geometry and governing dimensionless parameters have been introduced in Section 2.2. For the complex bypass pig, we generate four bypass adjusting holes to represent the bypass adjusting device (thus the dimensionless parameter $n = 4$), and we change the angle of bypass adjusting holes ω, to represent the bypass adjusting process. Unlike the conventional bypass pig and disk pig have axisymmetric geometry and two dimensional CFD simulations can be used, the complex bypass pig study requires three dimensional CFD models, which means the simulations involved in this chapter are much more computational expensive than the disk pig study in chapter 5. In this study, two complex bypass pig models are studied. The parameters govern the first complex bypass pig geometry are summarized in Table 4.2, in the initial model when the parameter $\omega = 45°$, both the horizontal bypass area and the opening holes bypass area are 30%. Furthermore, another complex bypass pig model is investigated in this study, the parameters govern this complex bypass pig geometry are summarized in Table 6.1. With these parameters, the initial model has both 10% horizontal bypass area and opening holes bypass area.

In this chapter, first of all the flow features of the complex bypass pig are presented. Furthermore, different parameter studies are carried out, in order to study how the pressure loss coefficient K (and overall pressure drop) is influenced by the governing parameters of the complex bypass pig model. In this study, two correlations are suggested to predict the pressure loss coefficient for the complex bypass pig, and these correlations are tested at the end of this chapter.

6.1. FLOW FEATURES OF COMPLEX BYPASS PIG

The flow features around the complex bypass pig are introduced in this section. First of all, as the complex bypass pig geometry is based on the disk pig, the flow features around the disk pig with same parameters of the complex bypass pig models, but without the bypass-adjusting device, are introduced.

Figure 6.1 shows the streamlines of the disk pig models. Figure 6.1a and 6.1b show the results of the disk pig models with 30% and 10% horizontal bypass area, respectively. In both cases, the flow behaves as the behaviour B, as discussed in Section 5.1. The jet formed in the disk bypass region contacts the pipe wall directly, the main recirculation zone is under the jet, and there is a smaller recirculation zone at the corner of the bypass pig and pipe wall.

Figure 6.2 shows the streamlines of the complex bypass pig. The left figures show the streamlines on a cross section plane. Figure 6.2a and 6.2c show the streamlines of the complex bypass pig with 30% and 10% bypass areas, respectively[1]. From these figures, we find that the jets formed in the bypass adjusting holes contact the pipe wall directly, and there are recirculation zones at the corner of pig body and pipe wall. The main recirculation zone is in the downstream pipe, and the main recirculation zone is much more complex than in disk pig case. This is because there are four three-dimensional main jets formed in the four bypass adjusting holes, and when the jets flow around the disk, the jet structured flows mix again in the downstream pipe.

As the flow in the bypass adjusting holes region is very complex, we generate streamlines on another pipe-section plane halfway between the pig body and the disk, as shown in Figure 6.2b and 6.2d, for 30% bypass areas case and 10% bypass area case, respectively. From these figures we can

[1]As discussed before, two complex bypass pig models are studied in this study, the first model has 30% horizontal bypass area, while the second model has 10% horizontal bypass area. For both two initial models with 45 degrees bypass adjusting holes, the opening holes bypass area are equal to the horizontal bypass area

Parameter	Value
Bulk velocity U	UDF
Horizontal bypass area (%)	10%
Pipe Diameter D	1.16 m
Bypass pig diameter d	0.3668 m
Upstream pipe length	$2D$
Downstream pipe length	$20D$
Horizontal bypass length	2 m
Location of the back of the pig	z=0
Holes bypass area (%)	10%
Distance between the pig body and the disk h	$0.1118D$
Disk diameter H	$0.4835D$
Holes inner diameter H_i	$0.4472D$
Disk thickness t	$0.07071D$
Number of holes n	4
Angle of hole ω	45^o
Density ρ	68 kg/m^3
Viscosity μ	2.264 E-5 kg/ms
Reynolds number R_e	1 E+7

Table 6.1: Key parameters of complex bypass pig geometry, with 10% horizontal bypass area, used in the complex bypass pig study

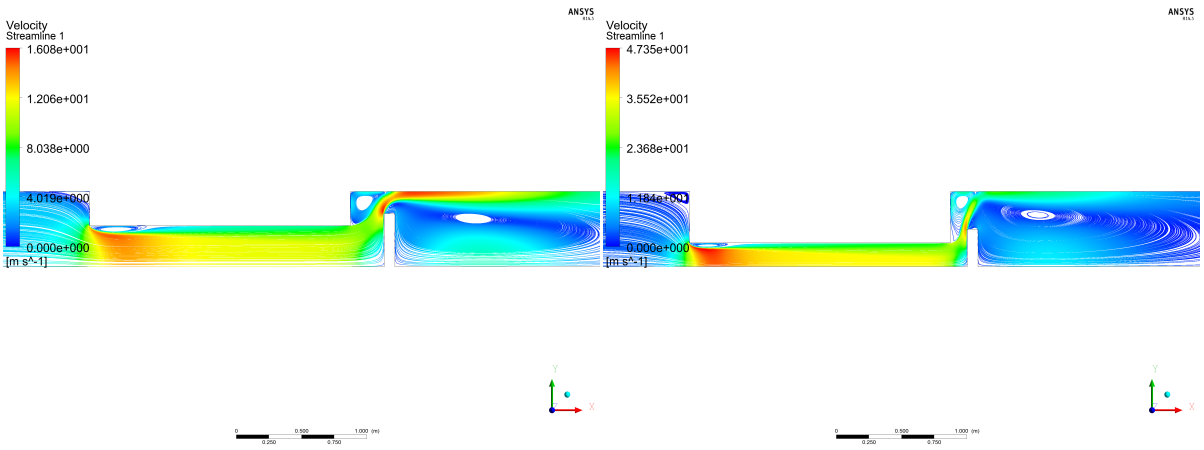

(a) Streamlines of the disk pig with 30 persents horizontal bypass area

(b) Streamlines of the disk pig with 10 persents horizontal bypass area

Figure 6.1: Streamlines of the disk pigs with the same parameters of the complex bypass pigs

observe how the flow passes through the bypass adjusting holes. In these figures, the white blank regions represent the solid part of the bypass adjusting device, and the grey region represents the flow region. Four main jets are formed in the bypass adjusting holes, and contact the pipe wall after they flow out of the holes. In the region between the bypass adjusting device and pipe wall, recirculation zones are observed between two neighbour main jets. For the complex bypass pig with 10% bypass areas, the distance between the bypass adjusting holes and the pipe wall is relatively long, thus, each of the main jets separates into two smaller jets, and additional recirculation zones are observed between the two jets.

In reality, for a bypass pig that contains bypass adjusting device, the thickness of the bypass adjusting device is relatively small. In the complex bypass geometries studied in this research, we make this thickness relatively small, which means the dimensionless parameter H_i/H is close to 1, and this is shown in Figure 6.2b and 6.2d. Unfortunately, the research to study the flow around this type geometry is limited. However, the situation when the flow pass through the opening holes is similar as the flow around the sharp-edged orifice, as discussed in Section 2.4.5. Thus, the Idelchik's correlation for sharp-edged orifice (Equation 2.29) is used to compare with the results from complex bypass pig study. For the sharp-edged orifice, the thickness of the orifice's influence on the flow behaviour and the overall pressure loss coefficient K_{seo} is negligible. In our case, as the thickness of the bypass adjusting device is also relatively small, then we assume it has little influence on the flow behaviour in complex bypass pig geometry.

Figure 6.3 shows the total pressure contour on the cross section plane for the complex bypass pig models. Figure 6.3a and 6.3b show the results for the complex bypass pig models with 30% and 10% bypass areas, respectively. The total pressure is not changing a lot when the flow passes through the horizontal bypass area, and large pressure drop happens when the flow pass around the disk. The lowest total pressure is in the recirculation zone in the corner of the pig body and pipe wall, and relatively low total pressure in the main recirculation zone in the center of the downstream pipe. As the model with 10% bypass areas has much smaller horizontal bypass area and opening holes

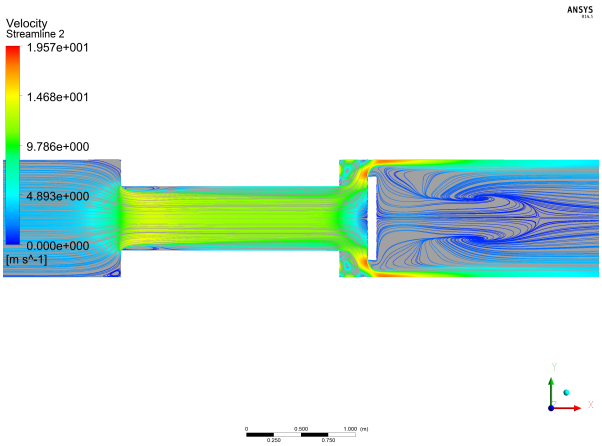

(a) Streamlines of complex bypass pig with 30 persents horizontal bypass area on the cross section plane

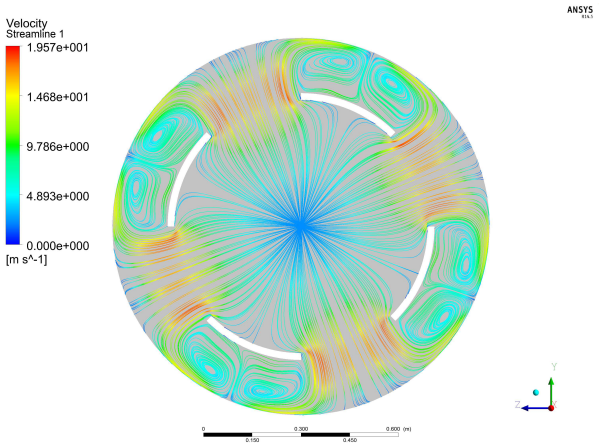

(b) Streamlines of complex bypass pig with 30 persents horizontal bypass area on the pipe section plane, which is at $x = 2m + 0.5h$

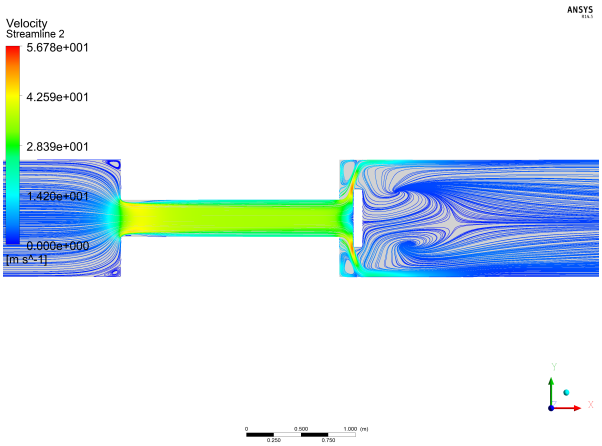

(c) Streamlines of complex bypass pig with 10 persents horizontal bypass area on the cross section plane

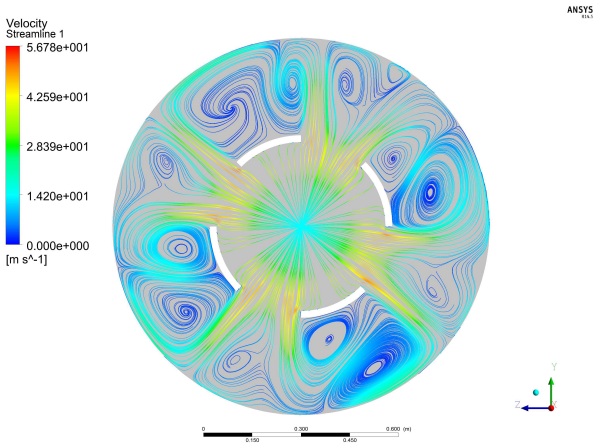

(d) Streamlines of complex bypass pig with 10 persents horizontal bypass area on the pipe section plane, which is at $x = 2m + 0.5h$

Figure 6.2: Streamlines for the complex bypass pig

bypass area, it has much larger overall pressure drop than the 30% bypass areas model. Furthermore, Figure 6.4 shows the total pressure coefficient's distribution on the centreline. Based on these figures, it is found that most of the total pressure drop comes from the disk bypass region and the opening holes bypass region.

6.2. PARAMETER STUDY

In this section, different parameter studies of the complex bypass pig are carried out, in order to study the relationship between the pressure loss coefficient K for complex bypass pig and its governing parameters. As discussed in Section 2.2, the complex bypass pig geometry is based on the disk pig, and additional parameters are required to govern the bypass adjusting device. In this research, we generate four opening holes to represent the bypass adjusting device, so the dimensionless parameter $n = 4$. The thickness of the bypass adjusting device is relatively small in the complex bypass

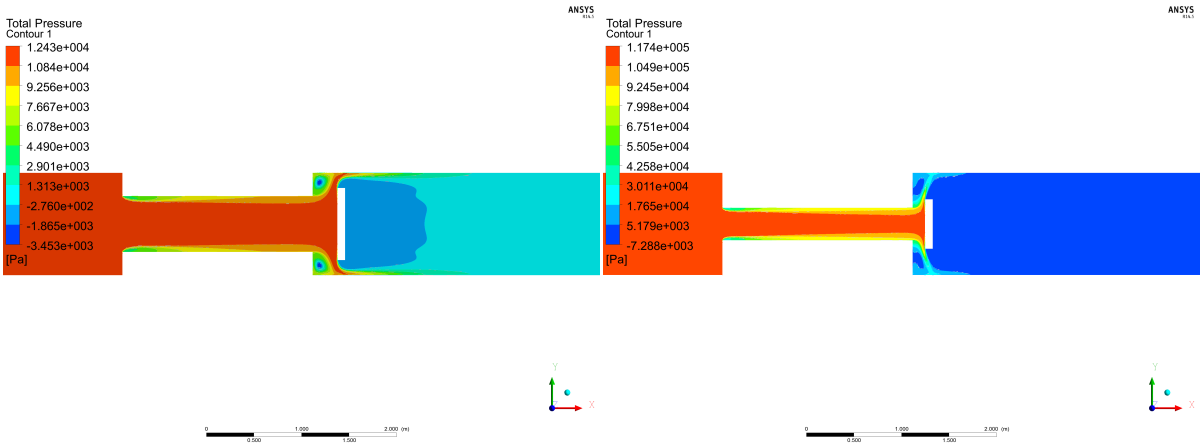

(a) Total pressure contour of complex bypass pig with 30 persents horizontal bypass area on the cross section plane

(b) Total pressure contour of complex bypass pig with 30 persents horizontal bypass area on the cross section plane

Figure 6.3: Total pressure contours on the cross section plane of the complex bypass pig

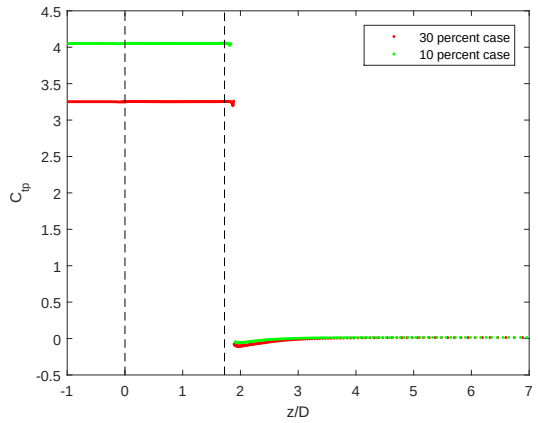

Figure 6.4: Total pressure coefficient distribution on the centreline of the complex bypass pig

pig, and the dimensionless parameter thickness of bypass adjusting holes H_i/H should be close to 1. Thus, in this study we mainly consider the influence of the dimensionless parameter opening fraction of the holes $\omega/45°$ on the flow behaviour around the complex bypass pig, especially the pressure loss coefficient (and overall pressure drop).

Four parameter studies for the disk pig have been presented in Section 5.3, and a correlation to calculate the pressure loss coefficient for the disk pig K_{dp} (Equation 5.1) was suggested and tested in this study. It is found that this correlation can predict K_{dp} accurately, if the flow around the disk pig behaves as the flow behaviour B. As discussed in Section 6.1, the flow around the complex bypass pig still behaves as the flow behaviour B.

Thus, in this section, two parameter studies for the complex bypass pig are carried out, for the dimensionless parameters:

- Horizontal bypass area: $(\frac{d}{D})^2$

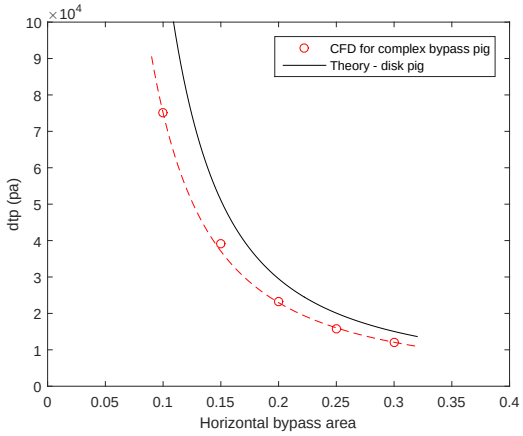

(a) Overall pressure drop as a function of the horizontal bypass area

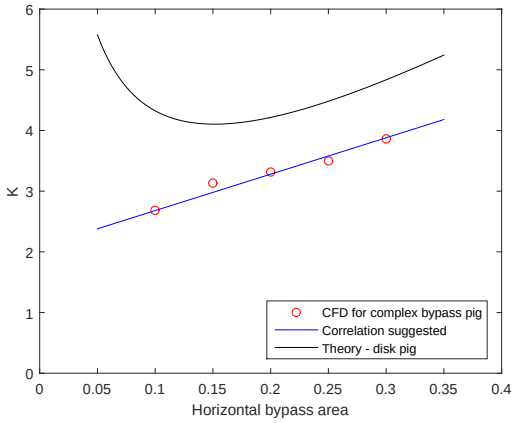

(b) Pressure loss coefficient as a function of the horizontal bypass area

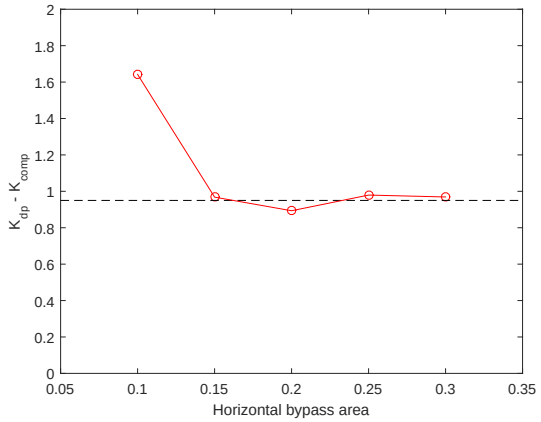

(c) Difference of pressure loss coefficient between the equivalent disk pig and the CFD results for complex bypass pigs

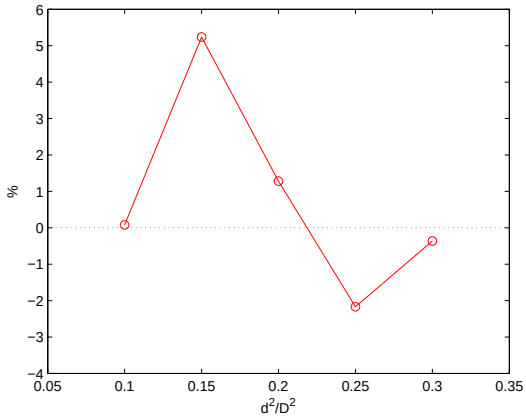

(d) Deviation of the suggested correlation from the CFD results

Figure 6.5: Results from parameter study: horizontal bypass area, for the complex bypass pig

- Opening fraction of the holes: $\frac{\omega}{45°}$

And the correlations to predict the pressure loss coefficient K (and overall pressure drop) for complex bypass pig will be introduced.

6.2.1. HORIZONTAL BYPASS AREA

The complex bypass pig geometry with 30% bypass areas (both horizontal bypass area and bypass adjusting holes' bypass area) are used in this parameter study for horizontal bypass area. We keep the other parameters fixed and decrease the parameter: bypass pig diameter d, in order to decrease the horizontal bypass area from 30% to 10%.

Figure 6.5 shows the results from the horizontal bypass area parameter study. The theoretical results calculated by Equation 5.1 for the equivalent disk pigs are also included in these figures, as the black solid line. The concept of equivalent disk pig will be introduced in Section 6.2.2.

Figure 6.5a shows the overall pressure drop as function of the horizontal bypass area, we find that the overall pressure drop increases if we decrease the horizontal bypass area as a regular curve. This is because we keep other parameters fixed, and when we decrease the diameter of the bypass area d, the pressure drop in the sudden contraction region and disk bypass region will increase. With same horizontal bypass area, the theoretical overall pressure drop of the equivalent disk pig is always higher than the complex bypass pig's overall pressure drop, but the lines have similar trend.

Figure 6.5b shows the pressure loss coefficient K as a function of the horizontal bypass area. The K is calculated by the velocity in the horizontal bypass area, as the bypass adjusting holes' bypass area is always equal to 30%, the maximum averaged velocity is always in the horizontal bypass region. Similar as Figure 6.5a for the overall pressure drop, with same horizontal bypass area, the complex bypass pig has smaller overall pressure loss coefficient K than the equivalent disk pig. However, the theoretical results for the equivalent disk pig (shown as the black solid line) has the similar trend as the CFD results for the complex bypass pig, especially when the horizontal bypass area is larger than 15%. Figure 6.5c shows the difference between the CFD results for complex bypass pig and the theoretical results for equivalent disk pig, when the horizontal bypass area is larger than 15%, the $K_{dp} - K_{comp}$ is always around a constant 0.95.

The results from complex bypass pig CFD simulations are locating on a straight line, thus a new correlation can be suggested, to representing the relationship between overall pressure loss coefficient in complex bypass pig and the horizontal bypass area:

$$K = 6(d^2/D^2) + 2.08 \tag{6.1}$$

Figure 6.5d shows that Equation 6.1 can calculate the overall pressure loss coefficient for complex bypass pig as a function of the horizontal bypass area accurately, as the maximum error is 5% and errors for most of the results are within 2%.

6.2.2. OPENING FRACTION OF THE HOLES

In this part, the complex bypass pig models with different angle of bypass adjusting holes ω are investigated. In reality, the bypass area is controlled by closing and opening of the bypass adjusting holes. However, in CFD simulations, we cannot decrease the opening holes' angle continuously. Thus, complex bypass pig models with typical angles of bypass adjusting holes: 11.25°, 22.5°, 37.75° and 45°, are studied to represent the bypass adjusting process. By changing the angle of the opening holes from 45° to 11.25°, the dimensionless parameter opening fraction of the holes $\omega/45°$ is changed from 1 to 0.25. The complex bypass pig models with the governing parameters which are summarized in Table 4.2 and 6.1 are both studied in this parameter study.

Figure 6.6 shows the general results from this parameter study. Two complex bypass pig models are both studied in this part, and it is found that the overall pressure drop of the complex bypass pig is strongly dependent on the parameter opening holes bypass area $Hh\omega/22.5D^2$, as shown in Figure 6.6a. The overall pressure drop increases if we decrease the bypass adjusting holes' bypass area. Also, for the two complex bypass pig models with different parameters, when they have the same opening holes' bypass area[2], the overall pressure drop in the 10% bypass areas model is much

[2]On Figure 6.6a, the two complex bypass pig models have same opening holes' bypass area 7.5%, when the 30% bypass

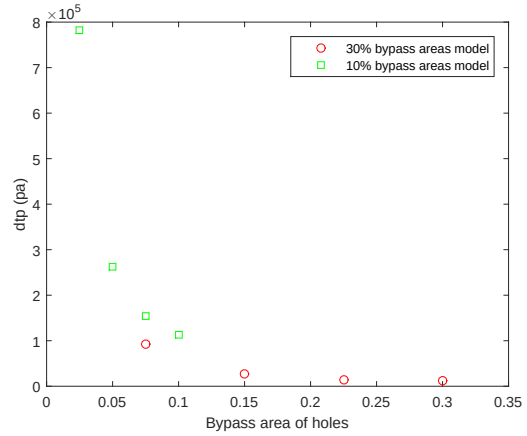

(a) Overall pressure drop as a function of the opening holes' bypass area

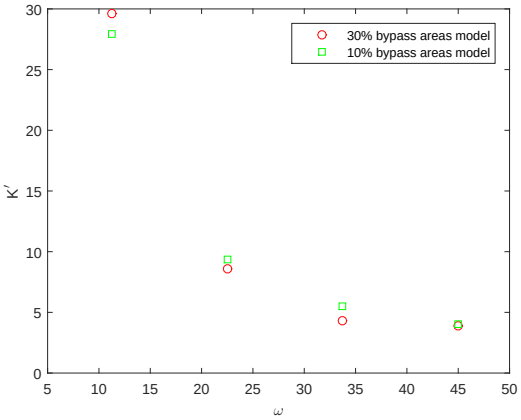

(b) Overall pressure loss coefficient K' as a function of angle of the bypass adjusting holes

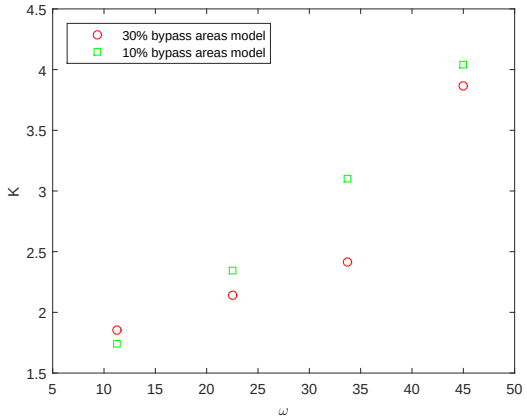

(c) Overall pressure loss coefficient K as a function of angle of the bypass adjusting holes

Figure 6.6: Results from parameter study: angle of the bypass adjusting holes, for the complex bypass pig

higher than the model with 30% initial bypass areas. This is because the 10% bypass areas complex bypass pig has much smaller horizontal bypass area, thus has larger pressure drop in the sudden contraction and disk region, as discussed in Section 6.2.1.

On the other hands, the pressure loss coefficient for complex bypass pig is strongly dependent on the angle of the bypass adjusting holes, as shown in Figure 6.6c and 6.6b. In this study, we calculate two pressure loss coefficient K' (as shown in Figure 6.6b) and K (as shown in Figure 6.6c) for the complex bypass pig. As discussed in Section 2.4.1, for the original equation to calculate the overall pressure loss coefficient K (Equation 2.22), the K is calculated by the maximum average velocity in different bypass regions, which is the average velocity in the opening holes in this case. On the other hand, similar as the correlation to calculate the overall pressure loss coefficient is disk valve (Equation 2.28) and the suggested equation for disk pig model (Equation 5.1) in Section 5.3, the coefficient K' is calculated by the average velocity in the horizontal bypass area. Thus the relationship

areas model's parameter $\omega = 11.25°$, and the 10% bypass areas model's parameter $\omega = 33.75°$

between the coefficient K and K' can be expressed as:

$$K = K'(\frac{{V_{horizontal}}^2}{{V_{holes}}^2}) \tag{6.2}$$

Where $V_{horizontal}$ and V_{holes} are the average velocities in the horizontal bypass region and opening holes, respectively. And the velocities in different bypass area are determined by the governing parameters of the complex bypass pig geometry.

It is found that the pressure loss coefficient for disk K'_{dp} is dependent on the disk bypass area[3]. Thus, in order to analyse the results from complex bypass pig study, the equivalent disk pig for complex bypass pig is introduced at here. The general idea behind this approach is: use a disk pig with similar parameters as the complex bypass pig, but change the parameter distance between the pig body and disk h, in order to make the disk bypass region equal to the bypass adjusting holes' bypass area of the complex bypass pig. Thus, for a complex bypass pig with certain angle of the opening holes, the adapted parameter: distance between the pig body and disk h_{dp-equ} for the equivalent disk pig can be expressed as:

$$h_{dp-equ} = h_{comp}(\frac{\omega}{90})\frac{H}{d} \tag{6.3}$$

The theoretical results calculated by Equation 5.1 for the equivalent disk pig are compared with the CFD results. The left figures (Figure 6.9a and 6.7c) show the results as the coefficient K', which is calculated by the velocity in the horizontal bypass region; and the right figures (Figure 6.9b and 6.7d) show the results as the coefficient K, which is calculated by the maximum average velocity in the complex bypass pig model (in this case in the opening holes region).

In general, the shape of the lines calculated by the suggested equation for equivalent disk pig for complex pig match the results from the CFD simulations for complex bypass pig, especially when the parameter ω is larger than 20 degrees. Furthermore, the theoretical results from equivalent disk pig match the CFD results from the 10% bypass areas complex bypass pig model much better than 30% bypass areas model. In fact, as discussed in the flow features of complex bypass pig part (Section 6.1), for the 30% bypass areas complex bypass pig model, the distance between the bypass adjusting holes and the pipe wall is much smaller than the model with 10% bypass areas. Thus, for the 30% bypass areas model, the pipe wall can have influence on the jets formed in the opening holes.

Based on the equivalent disk pig approach, the correlation for the complex bypass pig can be suggested:

$$K'_{comp} = K'_c + K'_{dv-equ} = 0.5(1-\frac{d^2}{D^2})^{3/4} + 2\frac{H}{d} + \frac{0.155d^2}{h^2_{dp-equ}} - 1.85 \tag{6.4}$$

and

$$K_{comp} = K'_{comp}(\frac{H_i \cdot h \cdot \omega}{22.5d^2})^2 \tag{6.5}$$

Where the parameter h_{dp-cor} is calculated by Equation 6.3.

[3]As discussed in Section 5.3, the pressure loss coefficient K'_{dp} is decreasing if we keep other parameters fixed and increase the parameter: distance between the pig body and disk, then the disk bypass area is also increased. Furthermore, the suggested Equation in order to calculate K'_{dp} (Equation 5.1) has already been tested in the disk bypass area parameter study for disk pig, see Figure 5.9

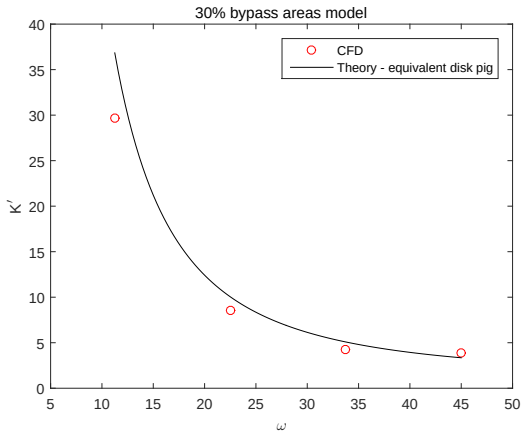

(a) K', 30 persents bypass areas complex bypass model

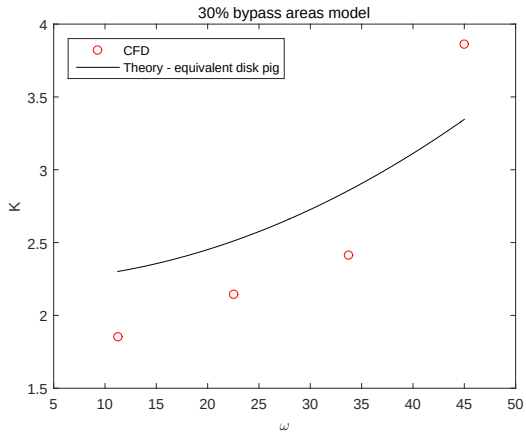

(b) K, 30 persents bypass areas complex bypass model

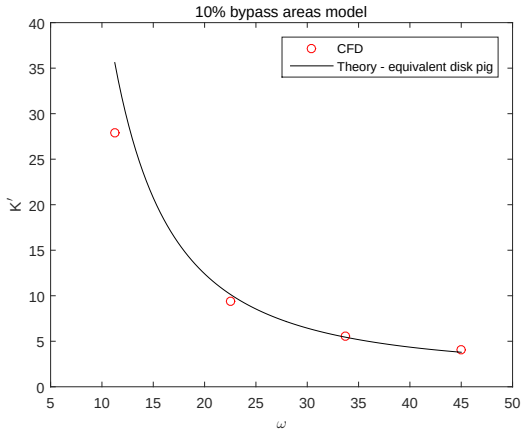

(c) K', 10 persents bypass areas complex bypass model

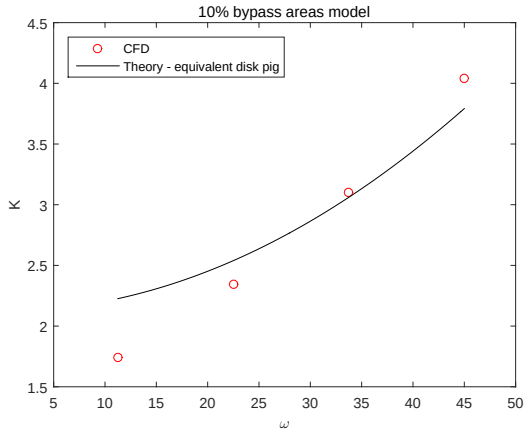

(d) K, 10 persents bypass areas complex bypass model

Figure 6.7: Results from complex bypass pig study compared with the theoretical results for the equivalent disk pig

Furthermore, it has already been tested that correlation combines the sudden contraction and disk valve can calculate the overall pressure loss coefficient for disk pig accurately, as the disk pig is formed by a sudden contraction and a disk valve. As discussed before, the complex bypass pig geometry is based on the disk pig, and the difference is the complex bypass pig has a bypass adjusting device between the pig body and the disk, and the condition when the flow pass through the bypass adjusting holes is similar as the flow pass through the sharp-edged orifice. Thus, another approach in order to investigate the pressure loss coefficient for complex bypass pig can be expressed as:

$$K_{comp} = K_c + K_{dv} + K_{holes} \tag{6.6}$$

Where the K_c, K_{dv} and K_{holes} represent the pressure loss coefficient for sudden contraction, disk valve and bypass adjusting holes, respectively.

The general idea of this approach is dividing the overall pressure drop in complex bypass pig into pressure drop in three parts: the sudden contraction, the disk valve and the bypass adjusting holes. For this investigation approach, we assume the additional pressure loss for complex bypass pig relative to the disk pig with same parameters is coming from the bypass adjusting holes, this

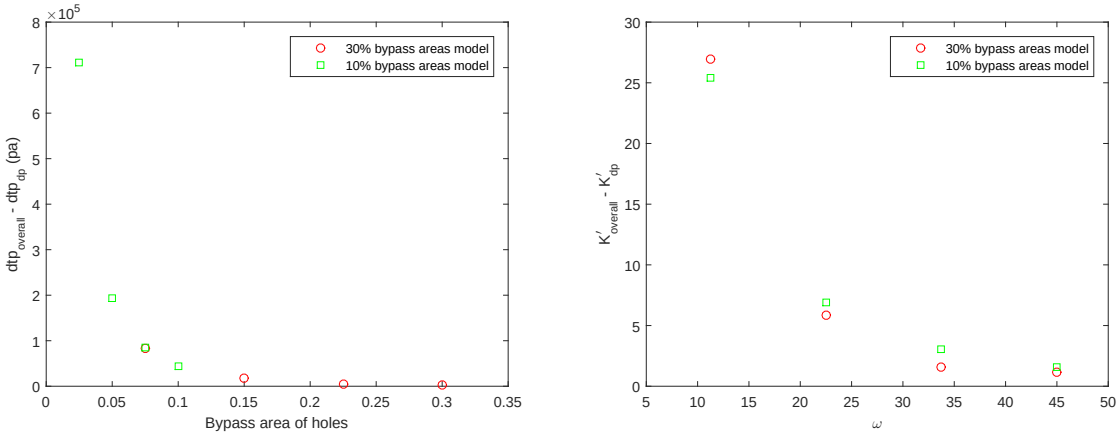

(a) Overall pressure drop as a function of the opening holes' bypass area

(b) Overall pressure loss coefficient K' as a function of angle of the opening holes

Figure 6.8: Pressure loss (coefficient) in the bypass adjusting holes of the complex bypass pig study

assumption can be expressed as:

$$\Delta p_{holes} = \Delta p_{comp} - \Delta p_{dp} \tag{6.7}$$

and

$$K'_{holes} = K'_{comp} - K'_{dp} \tag{6.8}$$

Where Δp_{dp} and K'_{dp} represents the overall pressure drop and pressure loss coefficient for a disk pig with the same parameters as the complex bypass pig[4].

Figure 6.8 shows the overall pressure drop and the pressure loss coefficient in the bypass adjusting holes calculated by Equation 6.7 and 6.8. We find that the overall pressure drop in the bypass adjusting holes is strongly dependent on the bypass area of opening holes, and the pressure loss coefficient is dependent on the parameter ω.

Furthermore, we use the Idelchik's correlation for the sharp-edged orifice (Equation 2.29) to calculate the pressure drop when the flow pass through the opening holes. From theory, the pressure drop in sharp-edged orifice is dependent on the cross section area of the orifice and pipe, F_0 and F_1 in Equation 2.29. And in our case, these two areas are calculated as:

$$F_0 = \pi H_i \cdot h(\frac{\omega}{90}) \tag{6.9}$$

and

$$F_1 = \pi H_i \cdot h \tag{6.10}$$

Then, Equation 2.29 in this case becomes as:

$$K_{holes} = (1 + 0.707\sqrt{1 - \frac{\omega}{90}} - \frac{\omega}{90})^2 \tag{6.11}$$

[4]Unlike the parameter h is adjusted for the equivalent disk pig approach, for this approach the disk pig's parameters are all same as the complex bypass pig, and without the parameters to governing the bypass adjusting device. These two disk pig models, one with 10% horizontal bypass area and another with 30% are introduced in Section 6.1, as shown in Figure 6.1a and 6.1b

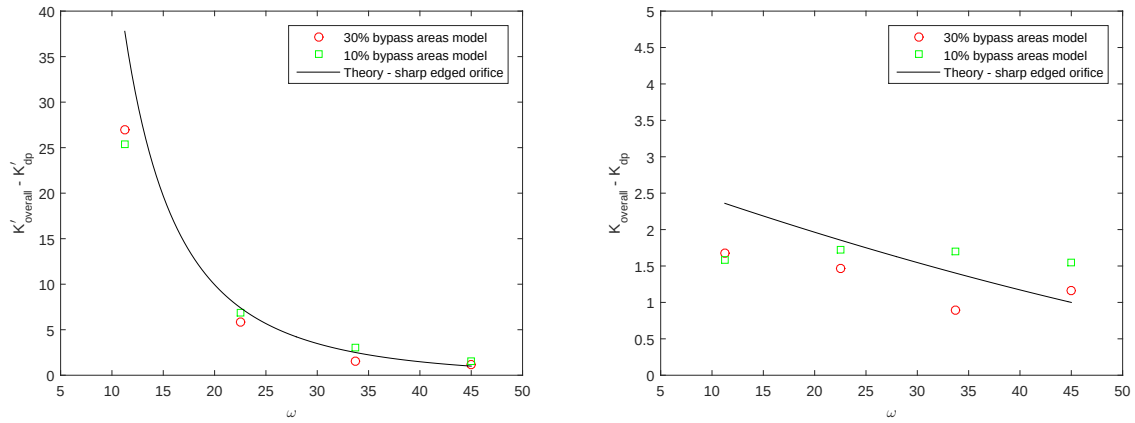

(a) K' calculated by the average velocity in the horizontal bypass area

(b) K calculated by the average velocity in the bypass adjusting holes (maximum average velocity in complex bypass pig)

Figure 6.9: Results from complex bypass pig study compared with the theoretical results for sharp-edged orifice

And the pressure loss coefficient is only as a function of the parameter ω.

Figure 6.9 compares the results from CFD simulations and the results calculated by the correlation for sharp-edged orifice. It is found that Equation 6.11 can calculate the pressure loss coefficient of the bypass adjusting holes accurately, when the angle of the opening holes is bigger than 20 degrees.

Based on this approach, another correlation for the complex bypass pig can be suggested:

$$K'_{comp} = K'_c + K'_{dv} + K'_{holes} = 0.5(1-\frac{d^2}{D^2})^{3/4} + 2\frac{H}{d} + \frac{0.155d^2}{h^2} - 1.85 + (1+0.707\sqrt{1-\frac{\omega}{90}} - \frac{\omega}{90})^2 \cdot (\frac{22.5d^2}{H_i \cdot h \cdot \omega})^2 \tag{6.12}$$

and

$$K_{comp} = K'_{comp}(\frac{H_i \cdot h \cdot \omega}{22.5d^2})^2 \tag{6.13}$$

In Equation 6.12, the first term represents the pressure drop due to sudden contraction, the second to fourth terms represent the pressure drop in disk valve and the last term represents the pressure drop in the bypass adjusting device.

6.3. TESTING OF THE SUGGESTED CORRELATIONS

In this section, the suggested correlations based on two approaches introduced in Section 6.2.2, which are used to investigate the overall pressure drop across the complex bypass pig:

- Equation 6.4, which is based on the first approach: using a equivalent disk pig for the complex bypass pig, to predict the pressure loss coefficient for it;
- Equation 6.12, which is based on second approach, in which we assume the pressure drop across the bypass adjusting holes can be calculated by the correlation for the sharp-edged orifice.

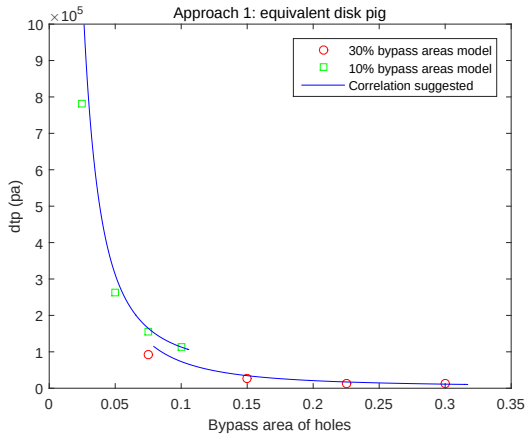

(a) Method 1: equivalent disk pig

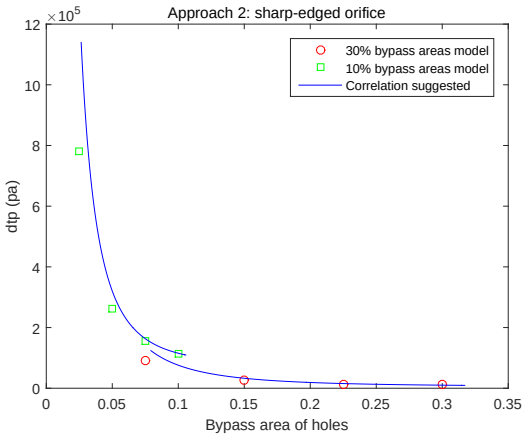

(b) Method 2: K_{comp}=K_c +K_{dv}+K_{holes}

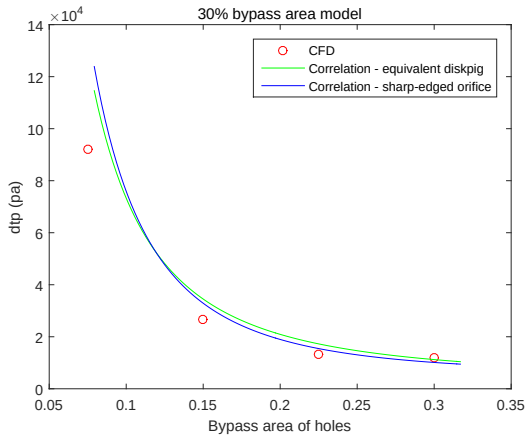

(c) 30% bypass areas model

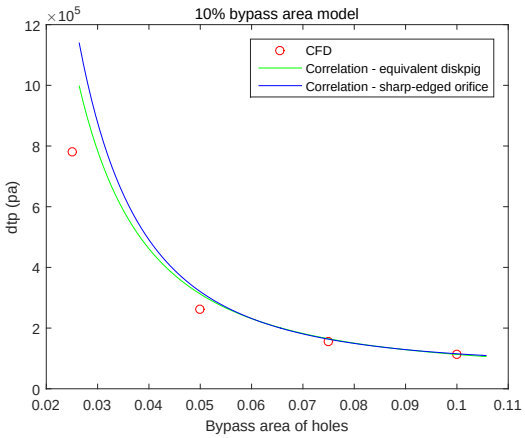

(d) 10% bypass areas model

Figure 6.10: Overall pressure drop as a function of the bypass area of the bypass adjusting area, testing of the correlations suggested

Are tested, by comparing the results calculated by Equations 6.4 and 6.12, with the CFD results.

Figure 6.10 shows the overall pressure drop as a function of the bypass area of the opening holes $Hh\omega/22.5D^2$, combines the results calculated by the correlations and the CFD results. As shown in Figure 6.10, both two methods can calculate the overall pressure drop in complex bypass pig accurately, when the angle of bypass adjusting holes is larger than 20 degrees.

Figure 6.10 shows the overall pressure drop as a function of the opening holes bypass area. In this figure, the results from the CFD simulations are compared with the results calculated by the two correlations suggested in Section 6.2.2. Figure 6.10a shows the correlation comes from the first approach: use the equivalent disk pig for the complex bypass pig to predict the overall pressure drop. Figure 6.10b shows the second approach: use the correlation for the sharp-edged orifice to predict the pressure drop across the bypass adjusting holes. It is found that both of the two correlations can predict the overall pressure drop across the complex bypass pig accurately, when the angle of the opening holes is larger than 20 degrees.

Figure 6.10c and 6.10d show the results for the complex bypass pig models with 30% bypass areas and 10% bypass areas, respectively. In general, the results calculated by the two correlations are

similar, in both cases. When the parameter $\omega = 11.25°$, the two correlations' results are larger than the CFD results, and the correlation comes from the equivalent disk pig approach is more accurate than the correlation based on the second approach. In this research, the flow around a sharp-edged orifice is investigated. This study is presented in Appendix A. In this study, it is found that when the sharp-edged orifice's bypass area is relatively small, the overall pressure drop predicted by the correlation for the sharp-edged orifice is much larger than the CFD results. This conclusion is similar as what we observe in this complex bypass study.

6.4. SUMMARY

In this chapter, the results from the complex bypass pig study are presented.

First of all, the flow features of the complex bypass pig are introduced. In general, the flow around the complex bypass pig is still similar as the disk pig. As the parameter distance between the pig body and the disk h is relatively large in the complex bypass pig study, the flow around the disk pig models behaves as the flow behaviour B. Due to the bypass adjusting holes, the flow behaviour after the horizontal bypass region is much more complex than the disk pig case.

Furthermore, different parameter studies are carried out. In order to get better understanding of the speed control process of the complex bypass pig, the bypass pig with different

Furthermore, different parameters studies are carried out, in order to achieve better understanding of the relationship between the pressure loss coefficient K for the complex bypass pig and its governing parameters. Most importantly, the complex bypass pig models with different parameter: angle of the bypass adjusting holes ω are studied, in order to represent the speed control (bypass adjusting) process of the complex bypass pig. Based on the disk pig study, two correlations based on two different approaches, which are introduced in Section 6.2.2, are introduced: Equation 6.4 and 6.12.

Finally, the correlations suggested in this study to predict the pressure loss coefficient for complex bypass pig, are tested, by comparing the results calculated by Equation 6.4 and 6.12 with the CFD results. It is found that these correlations can predict the overall pressure drop for the bypass pig models with various parameter angle of the opening holes ω, especially when $\omega > 20°$.

7

RESULTS OF MULTIPHASE STUDY

This chapter deals with the results from the multiphase study. First of all, the multiphase flow around a pig, which does not have bypass region, is investigated. In this case, as the pig is moving inside of the pipeline, the liquid slug will accumulate in the downstream pipe. One of the main purposes of this study is to investigate the relationship between the height of the liquid slug and the pig velocity. In practice, if the liquid slug can contacts the top of the pipe wall, the entire pipeline can be covered by the corrosion inhibitor, which is normally contained by the liquid phase flow. Furthermore, the multiphase flow around a (conventional) bypass pig is carried out, in order to investigate the multiphase flow behaviour in this condition.

7.1. PIG WITHOUT BYPASS REGION

The similar case studied by Kohda in 1988 [29] is investigated in this section. The case we consider here is: the no-bypass pig is moving inside of the pipeline, in which the fluids are in stratified flow condition. The pig is driven by the gas phase flow, with a velocity of 0.3 m/s. The liquid and gas phase are water and air, respectively, and the surface tension of the two phases is simulated as a constant: 0.07275 N/m. In the pig's reference frame, the velocities of the gas flow and the pig wall are 0, and the velocity of the pipe wall and the liquid flow are both -0.3 m/s. The liquid hold up in the pipeline is 10%. As the pig has no bypass region, the upstream pipe is not considered in the numerical model. The key parameters of this study are summarized in Table 7.1.

Figure 7.1 shows liquid volume fraction contours obtained by the numerical model. Figure 7.1a, 7.1b and 7.1c shows the volume fraction of liquid contour on the cross section plane at 1s, 4s and 6s, respectively. Figure 7.1d shows the volume fraction of liquid contour on a pipe section plane, and the shape of the liquid slug can be observed through this figure. It is found that with the pig velocity 0.3 m/s, the liquid slug in the downstream pipe does not contact the top of the pipe wall, and moves along the downstream pipe stably.

In this study, the influence of the pig velocity on the flow behaviour around the pig is investigated, by changing the pig velocity from 0.3 m/s to 1.8 m/s. In the pig's reference frame, the pig is stagnant, and the pipe wall and the liquid hold up is moving as the negative pig velocity.

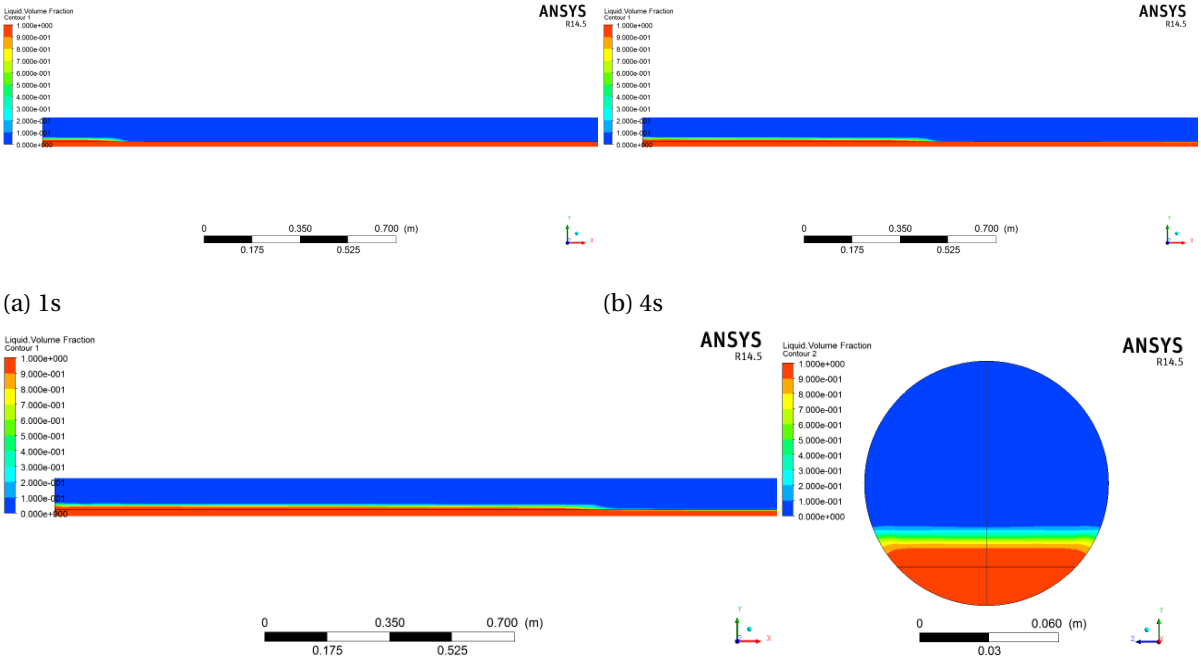

(a) 1s

(b) 4s

(c) 6s

(d) pipe-section

Figure 7.1: Liquid volume fraction contour

Figure 7.2 shows the liquid volume fraction contour for the models with different pig velocity. It is found that the liquid slug's height is increasing when we increase the pig velocity. When the pig velocity is relatively small, the liquid slug in the downstream pipe cannot contact the top of pipe wall, and the liquid slug is moving stably along the downstream pipe. Figure 7.2g and 7.2h shows the results when the pig velocity is 1.8 m/s, in this case, the liquid slug contacts the top of pipe wall directly, and make the flow behaviour in the downstream pipe more complex.

Parameter	Value
Gas velocity U_{gas}	0 m/s
Liquid velocity U_{liquid}	-0.3 m/s
Pipe wall velocity U_{wall}	-0.3 m/s
Pipe Diameter D	0.1053 m
Downstream pipe length	3 m
Location of the back of the pig	z=0
Density of gas ρ_{gas}	1.225 kg/m^3
Density of liquid ρ_{liquid}	998.2 kg/m^3
Viscosity of gas μ_{gas}	0.000018 kg/ms
Viscosity of liquid μ_{liquid}	0.001516 kg/ms
Surface tension	0.07275 N/m
Liquid hold up	10%

Table 7.1: Key Parameters govern the pig without bypass multiphase study

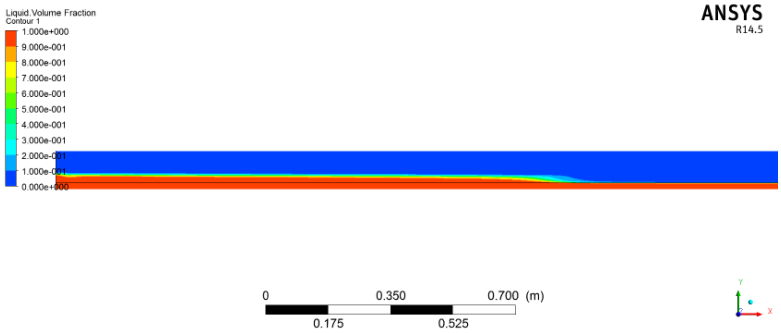

(a) 0.5 m/s

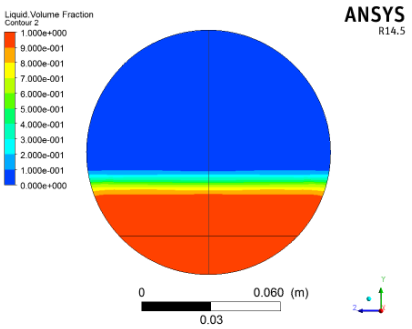

(b) 0.5 m/s

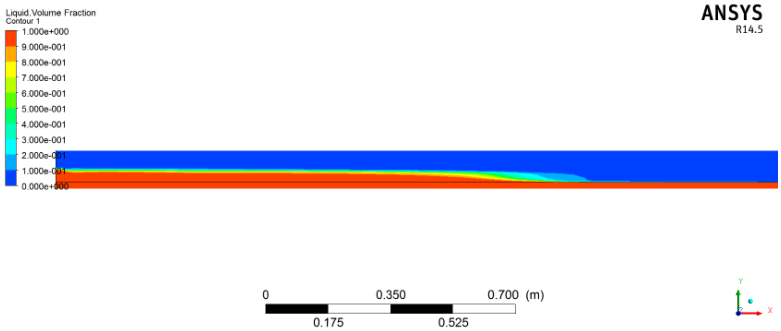

(c) 0.75 m/s

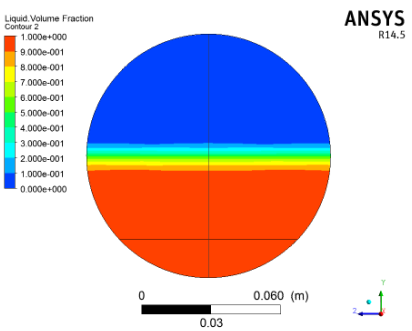

(d) 0.75 m/s

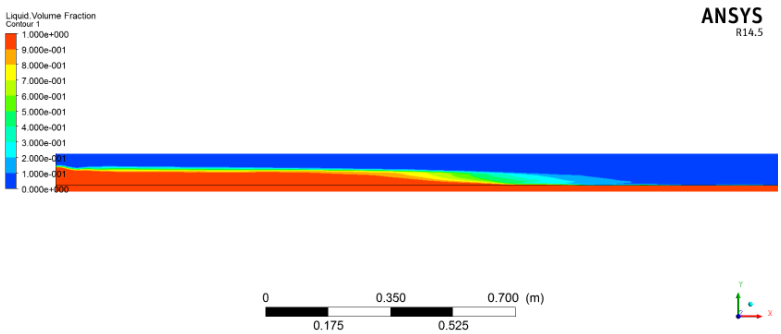

(e) 1 m/s

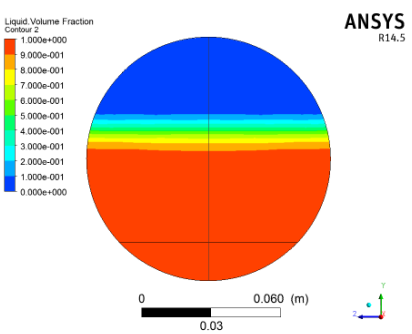

(f) 1 m/s

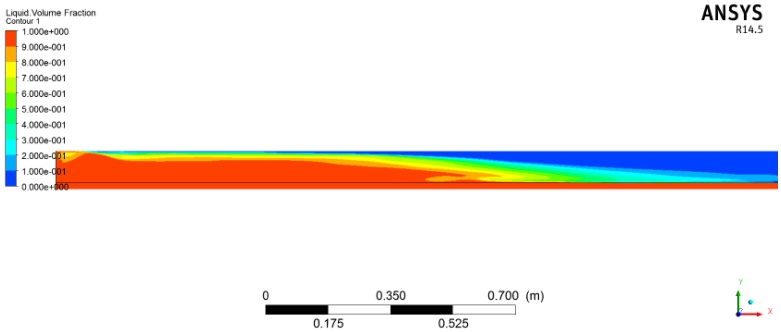

(g) 1.8 m/s

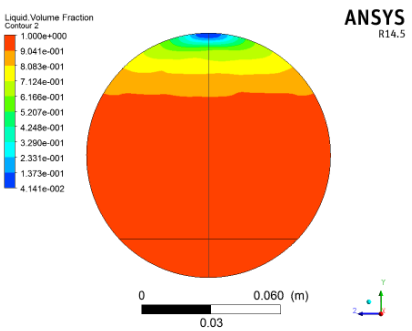

(h) 1.8 m/s

Figure 7.2: Liquid volume fraction contour with different pig velocity

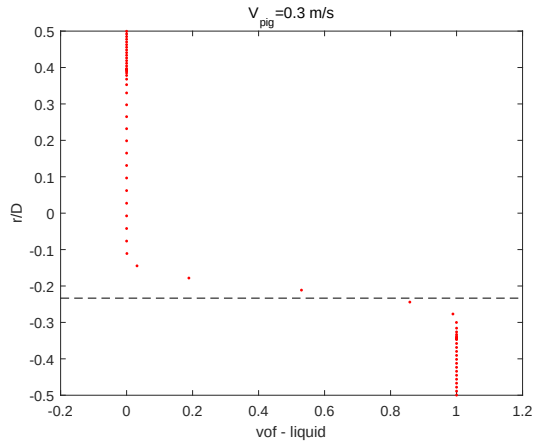

(a) Volume fraction of liquid

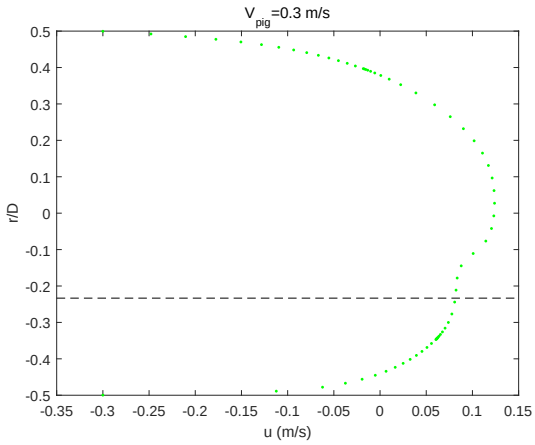

(b) Velocity of liquid slug front

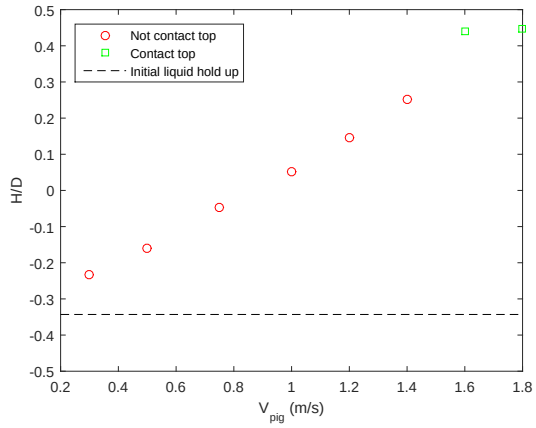

(c) Height of the liquid slug as a function of the pig velocity

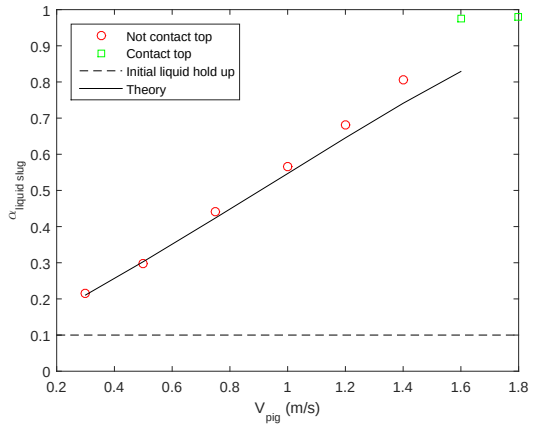

(d) Volume fraction of the liquid slug as a function of the pig velocity

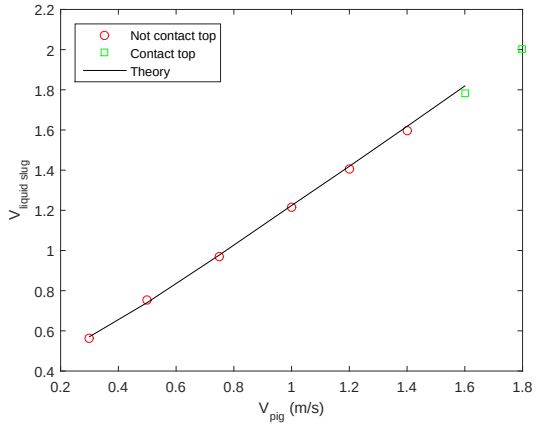

(e) Velocity of the liquid slug as a function of the pig velocity

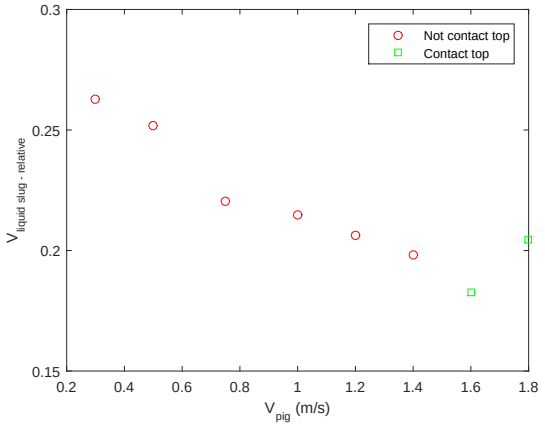

(f) Relative velocity of the liquid slug as a function of the pig velocity

Figure 7.3: Results of the pig velocity study for the no-bypass pig

Figure 7.3 shows the results of the pig models with various pig velocities study. Figure 7.3a and 7.3b shows the volume fraction of liquid and the x-velocity u's distribution in the y direction, for the

case $V_{pig} = 0.3m/s$. In these figures, the height of the liquid slug is shown as the dashed line.

Similar approach is applied to the models with various pig velocities. Figure 7.3c summarizes the height of the liquid slug as a function of the pig velocity. It is found that the slug height is increasing regularly if we increase the pig velocity, and when the pig velocity is larger than $1.6m/s$, the liquid slug contacts the top of the pipe wall, which are shown as the green points in this figure.

The volume fraction of the liquid slug is a function of the height of the liquid slug, which can be expressed as:

$$\alpha_{slug} = \frac{r^2 \arccos(-\frac{H}{r}) + H\sqrt{r^2 - H^2}}{F} \tag{7.1}$$

Where $F = \pi r^2$ is the cross section area of the pipe, and r represents the radius of the pipe.

For the models with various pig velocities, Figure 7.3d shows the volume fraction of the liquid slug, which is calculated by Equation 7.1, as a function of the pig velocity.

Then, the average velocity of the liquid slug can be calculated due to the mass conservation:

$$V_{front} = V_{pig} \cdot \frac{0.1}{\alpha_{slug} - 0.1} + V_{pig} \tag{7.2}$$

Figure 7.3e shows the real average velocity of the liquid slug, which is calculated by Equation 7.2, as a function of the pig velocity. Figure 7.3f shows the relative velocity of the liquid slug in the reference frame of the pig. The position of the liquid slug relative to the pig, as shown in Figure 7.2, is dependent on the relative velocity of the liquid slug.

7.1.1. THEORETICAL MODELLING OF THE LIQUID SLUG

In addition to the numerical results we now propose a theoretical model to describe V_{front} and α_{slug} which characterize the liquid slug. We apply a mass balance and a momentum balance across the slug front, which can be expressed as:

$$\alpha_{slug} F(V_{pig} - V_{front}) = \alpha F(-V_{front}) \tag{7.3}$$

And:

$$\alpha_{slug} F(V_{pig} - V_{front})^2 + HG_{slug} = \alpha F(-V_{front})^2 + HG \tag{7.4}$$

Where, the HG is the hydrostatic pressure, which can be calculated as[30]

$$HG_{slug} = g(\frac{1}{12} P_{lg}^3 - \alpha_{slug} F(r - H_{slug})) \tag{7.5}$$

And:

$$HG = g(\frac{1}{12} P_{lg}^3 - \alpha F(r - H)) \tag{7.6}$$

Where $P_{lg} = P_{lg}(\alpha)$ is the liquid interface which is a geometrical quantity which is a function of α.

The results calculated by solving Equation 7.3 and 7.4 are shown in Figure 7.3d and 7.3e as the black solid line. It is found that the CFD results match the results calculated by the theoretical equations.

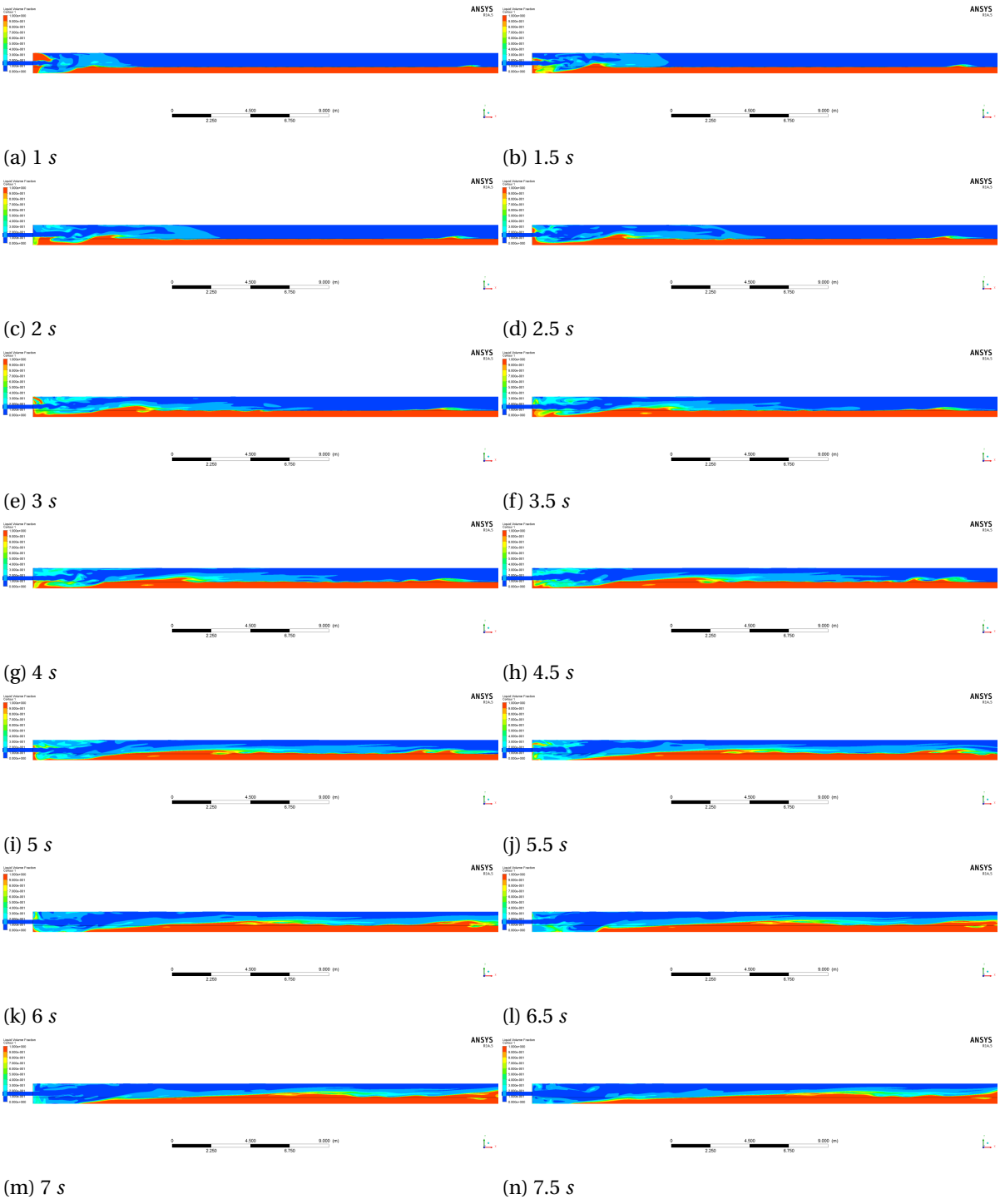

(a) 1 *s* (b) 1.5 *s*

(c) 2 *s* (d) 2.5 *s*

(e) 3 *s* (f) 3.5 *s*

(g) 4 *s* (h) 4.5 *s*

(i) 5 *s* (j) 5.5 *s*

(k) 6 *s* (l) 6.5 *s*

(m) 7 *s* (n) 7.5 *s*

Figure 7.4: Liquid volume fraction contour for the bypass pig multiphase study

7.2. PIG WITH BYPASS REGION

In this section, the multiphase flow around a pig with a (horizontal) bypass region is studied. The condition we considered in Section 4.2 is re-investigated in this study. The key parameters govern the bypass pig model are summarized in Table 4.3. In this study, the case we consider is: a conventional bypass pig with 4% horizontal bypass area is moving inside of the pipeline, the gas phase

flow is moving with 8 m/s, the liquid phase flow is moving with 2 m/s and the pig is driven by the mixture of gas and liquid, with a velocity 5 m/s. The initial liquid hold up is 30%, and in the initial CFD model, there is no liquid phase flow in the upstream pipe. This is because the pig is moving faster than the liquid phase flow, and slower than the gas phase flow, the gas can pass through the pig, thus the liquid in the downstream pipe cannot pass through the pig. The densities of the liquid phase flow and the gas phase flow are 750 kg/m^3 and 41.5 kg/m^3, and the viscosities of the liquid phase flow and the gas phase flow are 0.0005 kg/ms and 1.20E+5 kg/ms, respectively. The surface tension of the two phases is a constant: 0.0119 N/m[18].

Figure 7.4 shows the volume fraction of liquid contour on the cross section plane at various time. It is found that the flow behaviour in the downstream pipe is much more complex than the no-bypass pig study, which is presented in Section 7.1. In this study, the velocity of the gas phase flow is relatively large [1]. Thus, in the downstream pipe, it is found that the liquid slug is pushed by the bypassed gas flow, and moves along the downstream pipe.

[1] In the CFD model, the (relatively) velocity of the gas phase flow is 3 m/s, as the dimensionless parameter horizontal bypass region $(d/D)^2 = 0.04$, the velocity of the gas phase flow in the horizontal bypass region is around 75 m/s

8

CONCLUSIONS

8.1. SUMMARY AND RELEVANT CONCLUSIONS

In this research, the commercial CFD package ANSYS Fluent (version 14.5) has been applied to model the flow around bypass pigs which are moving inside a pipeline. If we consider the flow condition in the pipeline, this research can be divided into two parts: the single phase study and the multiphase study.

8.1.1. SINGLE PHASE STUDY

For the single phase study, the CFD approach is applied to model fully developed turbulent flow ($Re \approx 10^7$) around two types of bypass pigs: the disk pig and the complex bypass pig. We especially concentrate on the pressure loss coefficient K for various bypass pig geometries.

The disk pig has a fixed and relatively simple geometry (as shown in Figure 2.2), and it is based on the conventional bypass pig, by adding a deflector plate in front the pig body. For the conventional bypass pig, it has already been shown that the Idelchik's correlation for a thick orifice (Equation 2.30) can accurately predict the pressure loss coefficient K. In order to obtain the correlation, the conventional bypass pig geometry is treated as a linear combination of a sudden contraction and a sudden expansion. Similarly, for the disk pig, its geometry can also be treated as a linear combination of a sudden contraction and a disk valve. Thus, a correlation to predict the pressure loss coefficient K for the disk pig, based on the Idekchik's correlations for the sudden contraction (Equation 2.23) and the disk valve (Equation 2.28), is suggested: which is Equation 5.1.

The conclusions of the disk pig study are as follows:

- Two completely different flow behaviours (A and B, as shown in Figure 5.1), are observed around the disk pig. Most importantly, the pressure drop across the disk pig, which is the driving force of its motion, is strongly influenced by the flow behaviour around it. As shown in Figure 5.3, for the same disk pig geometry, flow behaviour B was found to cause a 30% overall pressure drop increase compared to flow behaviour A. During the disk pig study, it is found that:

- The two flow behaviours come from two different numerical solutions, while both solutions are in steady state, and the flow behaviour around the disk pig is dependent on the initial conditions of the CFD simulation. For the disk pig with certain parameters, the flow behaviour A will be observed, if the CFD model is initialized by the default initialization scheme of Fluent; on the other hand, flow behaviour B will be observed, if we run the CFD model as transient simulation for some time, and thereafter we run the solution from the transient simulation in steady state again.
- The flow behaviour around the disk pig is also dependent on the disk pig geometry. In general, the flow behaviour around the disk pig will change from behaviour A to B if we increase the diameter of the (horizontal) bypass region d. The same effect is observed if we decrease the diameter of the disk H or increase the parameter distance between the pig and the disk h.

Based on the parameter study for the dimensionless parameter D^*/D, the physics behind the flow behaviours around the disk pig become more clear. If the parameter D^*/D is relatively large, the flow around the disk pig behaves as the behaviour A. The shape of the jet and the recirculation zone between the jet and the pig body remains similar in various D^*/D cases. When the parameter D^*/D is relatively small, the distance between the disk and the downstream pipe is also relatively small. In this case, it is found that this distance is too short for the recirculation zone between the pig body and jet observed in flow behaviour A. Then, the recirculation zone can drive the jet towards the pipe wall directly, and the flow around the disk pig changes from behaviour A to B. In this case, the position of this recirculation zone changes to the corner of the pig body and the pipe wall.

For the disk pig model with certain governing parameters, two numerical steady state solutions can be achieved. This means that there exists a stable two solution region. In this research, the Navier-Stokes equations are modelled with a RANS approach, and the turbulence is modelled by a (realizable $k-\epsilon$) turbulence model. As the two solution region is a narrow region, the modelling choices could potentially have a large effect on the existence of the two solution region.

- Based on various parameters studies, it is found that the suggested correlation (Equation 5.1) can predict the pressure loss coefficient for the disk pig accurately, if the flow around the disk pig behaves as type B.

The complex bypass pig is a more advanced bypass pig model studied in this research. The complex bypass pig geometry is based on the disk pig, and opening holes are present between the horizontal bypass region and the disk, to generate the bypass area (as shown in Figure 2.3). In reality, the speed of the bypass pig is controlled by adjusting the bypass area. In this study we change the opening fraction of the bypass adjusting holes, to represent the bypass adjusting (speed control) operation of the complex bypass pig.

The conclusions of the complex bypass pig study are as follows:

- As the geometry of the complex bypass pig is based on the disk pig, the flow behaviour in certain regions is similar as the disk pig. As the parameter distance between the pig body and the

disk h is relatively large in this case, the flow around the complex bypass pig always behaves as type B, as introduced in the disk pig study. However, due to the bypass adjusting holes generated between the horizontal bypass region and the disk, the flow behaviour is much more complex in the complex bypass pig case, and the flow is not axisymmetric any more.

- To analyse the pressure drop coefficient (and overall pressure drop) of the complex bypass pig, two approaches are applied in the complex bypass study:
  - Equivalent disk pig approach: It is found that the overall pressure drop across the complex bypass pig is strongly dependent on the bypass area, thus, the concept of the equivalent disk pig is introduced first. The general idea behind this approach is: to use a disk pig, which has similar parameters as the complex bypass pig, and we change the parameter h in order to adjust the disk bypass area of the equivalent disk pig equal to the bypass area of the complex bypass pig. Then, a correlation based on this approach is suggested, which is Equation 6.4. This correlation has been tested in the disk pig study, and it can accurately predict the pressure loss coefficient for the disk pig, if the flow around the disk pig behaves as type B.
  - Sharp-edged orifice approach: in this approach, we assume that the flow around the bypass holes can be treated as a sharp-edged orifice. In this case, the complex bypass pig geometry is treated as a linear combination of a sudden contraction, a disk valve and sharp-edged orifices, to obtain a correlation to predict the pressure loss coefficient for the complex bypass pig, which is Equation 6.12. This correlation is based on the Idelchik's correlation for the sudden contraction, the disk valve and the sharp-edged orifice (Equation 2.29).

  During the complex bypass pig study, it is found that the suggested correlations accurately can predict the pressure loss coefficient for the complex bypass pig with bypass adjusting holes, especially when the dimensionless parameter opening fraction of the holes is relatively large.

Thus, in the single phase study of this research, the flow around the bypass pigs has been investigated in details. Moreover, correlations are suggested to predict the pressure loss coefficient for various bypass pigs. Finally, it is found that the bypass pig geometry can be treated as a linear combination of the components, that make up the geometry, to obtain the correlation to predict the pressure loss coefficient. Thus, this approach can be applied for the other bypass pigs.

If the correlations to predict the pressure loss coefficient K for the bypass pigs are known, the overall pressure across the bypass pigs can be calculated by Equation 1.2, as the velocities in the bypass regions are dependent on the governing parameters. Then, the motion of the pig in the pipeline can be described by Equation 1.1.

8.1.2. MULTIPHASE STUDY

The multiphase flow study was restricted to a stratified flow regime.

- First of all, the multiphase flow in front of a pig without bypass region is investigated. The fluids in the pipeline cannot pass through the pig, thus only the downstream pipe is take

into account in the numerical model. The influence of the pig velocity on the flow behaviour around the pig is investigated. It is found that when we increase the pig velocity, the height (and volume fraction) of the liquid slug in front of the pig is increasing. When the pig velocity is relatively small, the liquid slug cannot contact the top of the pipe wall, and it moves very stably along the downstream pipe. On the other hand, if the pig velocity is relatively large, the liquid slug contacts the top of the pipe wall, and in this condition the flow behaviour in the downstream pipe becomes much more complex. One of the practical purposes of this study is that we want to investigate under which condition the full pipeline gets wetted. This is important for the distribution of corrosion inhibitors.

In this study we describe the volume fraction and velocity of the liquid slug by applying a mass balance and a momentum balance across the slug front. It is found that the CFD results match the theoretical results.

- Secondly, the multiphase flow around a (conventional) bypass pig is investigated. The case that we consider in this study is such that the gas phase flow has a higher velocity than the liquid phase flow. Again, the equations are solved in a reference frame that moves with the pig. Thus, in the CFD model the liquid cannot pass through the bypass region and reach the upstream pipe. On the other hand, the gas can pass through the bypass region, and the bypassed gas makes the flow behaviour in the downstream pipe extremely complex. In this study, as the velocity of the gas phase flow is relatively large, it is found that the bypassed gas can push the liquid slug moving along the downstream pipe and sweep the liquid in front of the pig to the top of the pipeline.

8.2. RECOMMENDATIONS FOR FURTHER WORK

In this research, we obtained a better understanding of the flow behaviour around various types of bypass pigs. Most importantly, for both the disk pig and the complex bypass pig, correlations to predict the pressure loss coefficient are suggested based on CFD results. With the help of these correlations the motion of a pig in a pipeline can be described in a more accurate way. The following recommendations are suggested for further research:

- In the disk pig study, it is found that for a disk pig with certain parameters, two completely different numerical solutions can be achieved from the CFD simulations. Thus, the two-solution region of the disk pig could be investigated further, to achieve a better understanding of this special phenomena observed during this research.

- In this research, the suggested correlations to predict the pressure loss coefficient for various types of bypass pigs are based on the Idelchik's correlations for various components within the bypass pigs. However, it is found that these correlations have some limitations. For instance, for the suggested correlation for the disk pig, it is found that this correlation can only accurately predict the pressure loss coefficient, if the flow behaviour around the disk pig behaves as type B. Furthermore, it is found that the Idelchik's correlation for the sharp-edged orifice cannot predict the pressure loss coefficient accurately, when the bypass area is relatively small. In

future works, these correlations to predict the pressure loss coefficient for various geometries can be investigated, in order to obtain better understanding of the physics behind them.

- In the complex bypass pig study, two correlations are suggested based on different approaches, but both correlations are based on certain assumptions. Thus, it is recommended to find new theoretical correlations, which can be used to predict the pressure loss coefficient for the bypass adjusting device directly, in order to obtain a more universal correlation for the complex bypass pig. Furthermore, it is found that in order to obtain the correlations to predict the pressure loss coefficient for the conventional bypass pig, disk pig, and complex bypass pig, their geometries can be treated as a linear combination of the internal components. Thus, this suggests that a similar approach can be applied to obtain the correlations for other bypass pigs than the ones considered in this study.

- Based on the CFD results of the flow around a bypass pig, correlations to predict the pressure loss coefficient are suggested. It would be of interest to compare the CFD results with the results obtained from experiments, in order to investigate the accuracy of CFD modelling approach to predict the relevant flow quantities. Furthermore, for the flow around the disk pig, it would be of interest to investigate if a sudden change in pressure drop (due to the various flow behaviours around the disk pig in CFD modelling) can be also observed in the experiments, when we change the governing parameters of the disk pig continuously.

- As a three dimensional CFD model is required in the complex bypass pig study, only a few numerical simulations have been performed for the complex bypass pig. Thus, further parameter studies could be carried out, in order to achieve a better understanding of the relation between the pressure loss coefficient for the complex bypass pig and its governing parameters.

- For the multiphase study, we first investigated a relatively simple case: the multiphase flow in front of a pig without bypass region. We studied the influence of the pig velocity on the flow behaviour in the downstream pipe. Thus, further parameter studies, for instance for the initial liquid hold up, could be carried out. Furthermore, for the case in which the pig has a (horizontal) bypass region, due to the computational resources required by each simulation, only one simulation is carried out in this study. In future work, different parameter studies, for instance for the pig velocity, the horizontal bypass area or the initial liquid hold up, could be carried out, in order to investigate the influence of the other parameters on the multiphase flow behaviour around bypass pigs.

A

FURTHER VALIDATION

In this appendix, the further validation studies which are not included in Chapter 4 but relevant to this research are carried out. First of all, the mesh independent study for disk pig, which is not included in Section is introduced. Furthermore, the CFD study in order to valid the Idelchik's correlation for sharp-edged orifice is presented.

In this appendix, the further validation studies which are not included in Chapter 4 but relevant to this research, are carried out. First of all, the mesh independent study of the disk pig, which is not included in Section 4.1 is performed. Furthermore, in Chapter 6 we use the Idelchik's correlation for sharp-edged orifice (Equation 2.29) to calculate the pressure drop across the bypass adjusting holes, thus the correlation is validated in this chapter, by a sharp-edged orifice CFD study. In Chapter 5, we use the two dimensional axismmetric CFD models to study the flow around the disk pig, in this chapter, this assumption is validated.

A.1. MESH INDEPENDENCE STUDY FOR DISK PIG

The disk pig geometry is based on the conventional bypass pig, thus the mesh of disk pig model can be inspired by the validated conventional bypass pig mesh, as introduced in Section 4.1.1. The key parameters which govern the disk pig geometry used in this study are summarized in Table 4.4

Two meshes are generated for the disk pig model, with 7,126,808 and 11,199,543 cells, respectively. The first mesh which has around seven million cells is inspired by the validated mesh for the convention bypass pig, and another mesh with further refinement is generated, in order to investigate if the first mesh is fine enough to achieve solution which is mesh independent.

The distribution of the total pressure coefficient C_{tp} on the centreline is shown in Figure A.1. It is found the overall pressure drop predicted by two models with different mesh setting is similar. We further compare the flow behaviour in different regions obtained by the three dimensional CFD model, which has seven millions cells, with the validated two dimensional model. Figure A.2 shows the x-velocity profile in the different regions. Based on the parameters summarized in Table 4.4, we know that Figures A.2a, A.2b, A.2c and A.2d show the velocity profile in the upstream pipe, the horizontal bypass region, the disk bypass region and the downstream pipe, respectively. It is found that

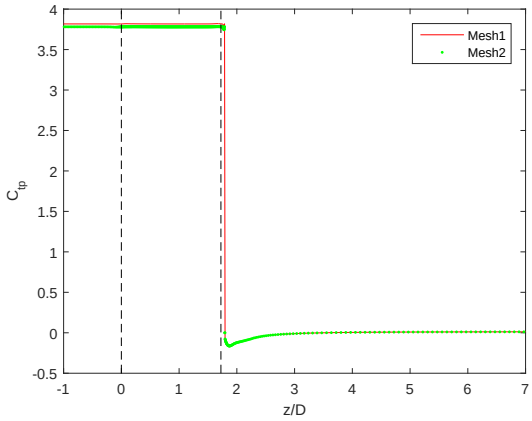

Figure A.1: Total pressure coefficient distribution on the centreline for the disk pig mesh independent study

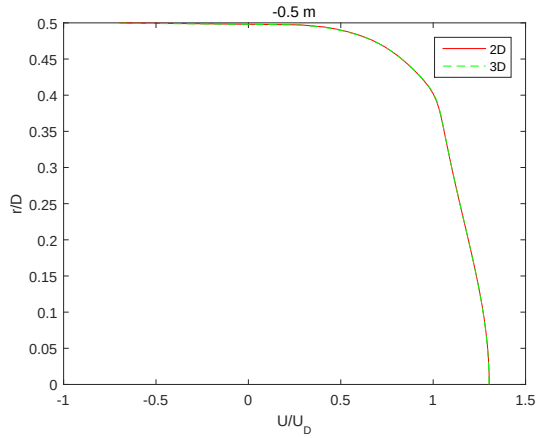

(a) x-velocity profile at -1m

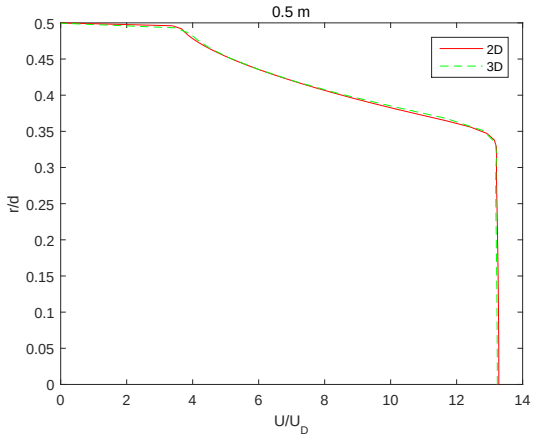

(b) x-velocity profile at 1m

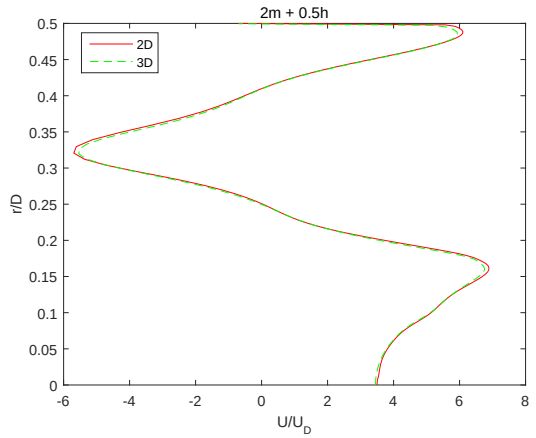

(c) x-velocity profile at $2m + 0.5h$

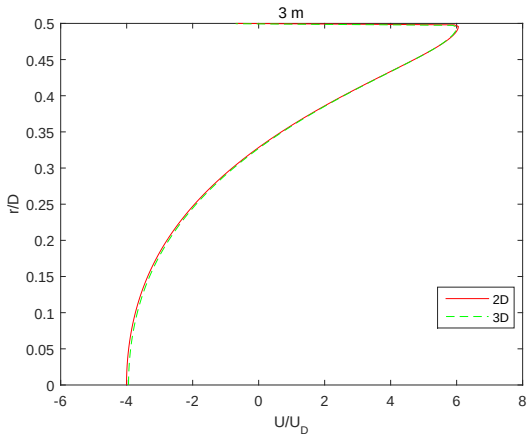

(d) x-velocity profile at 3m

Figure A.2: Velocity profiles for the disk pig mesh independent study

the flow behaviour in the three dimensional CFD model is similar to the validated two dimensional model.

Finally, Figure A.3 shows the y^+ value on the cells closest on the walls for the disk pig model. It

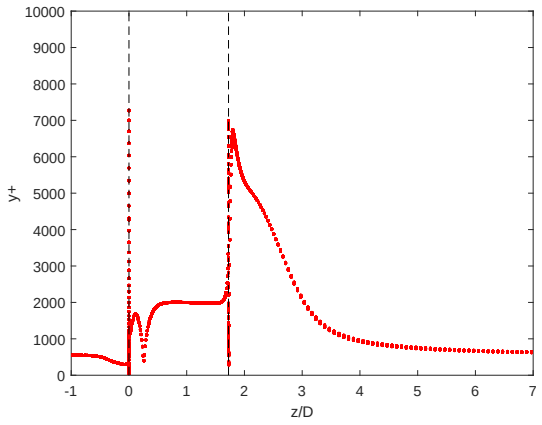

Figure A.3: y^+ value on the cells closest on the walls for the disk pig model

is found that all the y^+ values are in the acceptable region: $30 < y^+ < 20000$. Similar as the conventional bypass pig, the disk pig also has a axisymmetric geometry, and Figure A.3 shows that both of the mesh and the solution of the disk pig CFD model are axisymmetric.

In the disk pig study, which is presented in Chapter 5, two dimensional axisymmetric CFD model is used to study the flow around the disk pig, as the solution of the full three dimensional CFD is also axisymmetric. Furthermore, if we compare the flow behaviour obtained by the full three dimensional CFD model and the two dimensional axisymmetric CFD model, the results have no difference. Thus, it is concluded that the two dimensional axisymmetric CFD model can be applied to study the flow around the disk pig, and it can save a lot of computational resources and computing time than the three dimensional approach.

A.2. SHARP-EDGED ORIFICE VALIDATION

In this section, the correlation to calculate the pressure loss coefficient for sharp-edged orifice, as introduced in Section 2.4.5, is validated by using the wCFD model to simulate flow around the sharp-edged orifice, and comparing the CFD results with the results calculated by Equation 2.29. In this study, the CFD model of the sharp-edged orifice is based on the conventional bypass pig CFD model, which is validated in Section 4.1.1, and we decrease

In this section, the Idelchik's correlation to calculate the pressure loss coefficient for sharp-edged orifice (Equation 2.29) is validated, by comparing the CFD results with the results calculated by this correlation. Based on the CFD model of the conventional bypass pig study, which is validated in Section 4.1.1, the CFD model for the sharp-edged orifice study can be generated, by decreasing the parameter length of the bypass pig l.

Figure A.4a shows the streamlines of the flow around the sharp-edged orifice. It is found that, due to the length of the bypass region, the flow behaviour is completely different to the flow around the conventional bypass pig (thick orifice). After the fluid passes through the orifice, there is a main jet flow in the center of the downstream pipe, and recirculation zone is observed in the region between the main jet and the pipe wall.

Figure A.4b and A.4c show the total pressure drop and the pressure loss coefficient for the sharp-

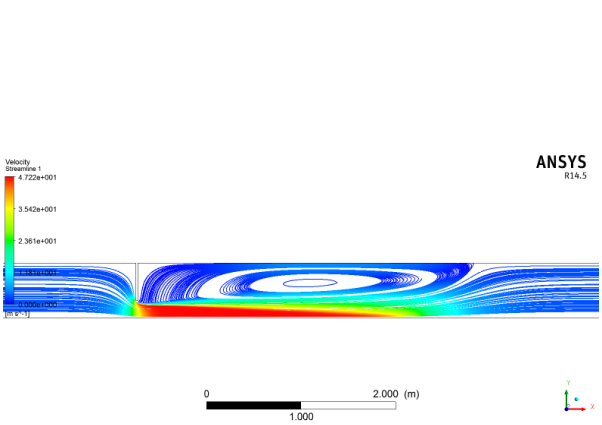

(a) Streamlines of the flow around the sharp-edged orifice

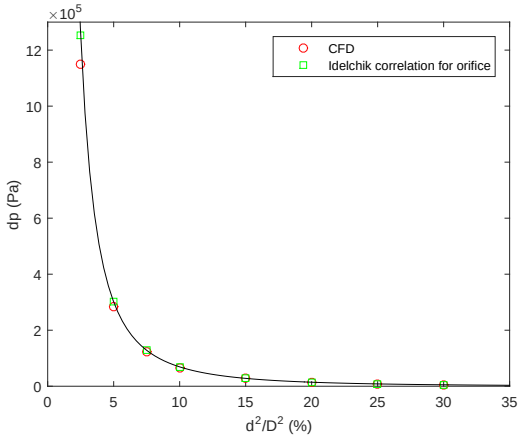

(b) Overall pressure drop as a function of the bypass area

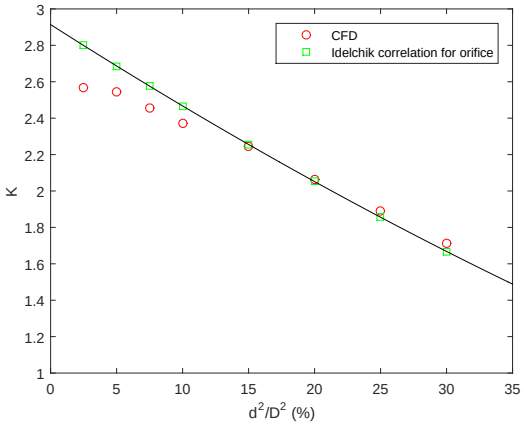

(c) Pressure loss coefficient as a function of the bypass area

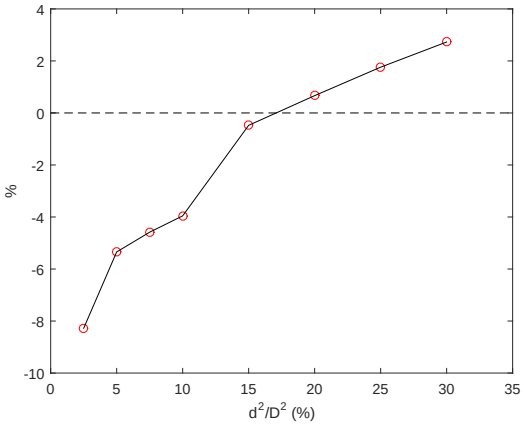

(d) Deviaion of the Idelchik's correlation for the sharp-edged orifice from the CFD results

Figure A.4: Results of the sharp-edged orifice study

edged orifice as a function of the orifice bypass area. In these figures, the theoretical results calculated by Equation 2.29 are showed as the black solid line. It is found that Equation 2.29 can predict the overall pressure drop accurately, especially when the orifice bypass area is larger than 15%. From Figure A.4d, it is found that the maximum error is around 8%, for the smallest orifice bypass area $d^2/D^2 = 2.5\%$, but still in the acceptable range; moreover, when the bypass area $d^2/D^2 > 15\%$, the errors are within 2%.

During this study, it is found that when the sharp edged orifice's bypass area is relatively small, the overall pressure drop calculated by the Idelchik's correlation is much larger than the CFD results, this is similar as what we find during the complex bypass pig study, which is introduced in Chapter 6.

BIBLIOGRAPHY

[1] F. M. White, *Fluid mechanics*, 7th ed. (McGraw-Hill, 2011).

[2] N. Money, D. Cockfield, S. Mayo, and G. Smith, *Dynamic speed control in high velocity pipelines,* Pipeline and Gas Journal **239(8)**, 30 (2012).

[3] H. S. Lee, D. Agustiawan, K. Jati, M. A. H. Aulia, S. A. Thomas, and S. P. Appleyard, *By-pass pigging operation experience and flow assurance study,* Offshore Technology Conference (2012).

[4] R. Bickerstaff, M. Vaughn, G. Stoker, M. Hassard, and M. Garrett, *Review of Sensor Technologies for In-line Inspection of Natural Gas Pipelines*, Tech. Rep. (Sandia National Laboratories, 2002).

[5] J. Tiratsoo, *Pipelind Pigging Technology*, 2nd ed. (Gulf Professional Publishing, 1992).

[6] L. F. A. Azevedo and A. M. Teixeira, *A critical review of the modeling of wax deposition mechanisms,* Petroleum Science and Technology **21(3-4)**, 393 (2003).

[7] Q. Wang, C. Sarica, and M. Yolk, *An experimental study on wax removal in pipes with oil flow,* Journal of Energy Resources Technology **130(4)**, 1 (2008).

[8] H. L. Wu and G. van Spronsen, *Slug reduction with high by-pass pigs - a mature technology,* 12th International Conference on Multiphase Production Technology, Barcelona (2005).

[9] G. L. Smith and J. S. Smart, *Pigging and chemical treatment for oil and gas pipe lines,* Pipe Line Industry (1991).

[10] A. M. Podgorbunskikh, *Devices for automated regulation of the velocity of in-tube pig flaw detectors (review),* Russian Journal of Nondestructive Testing (2012).

[11] T. T. Nguyen, H. R. Yoo, Y. W. Rho, and S. B. Kim, *Speed control of pig using bypass flow in natural gas pipeline,* IEEE International Symposium on Industrial Electronics **2**, 863 (2001).

[12] U. Thuenemann and J. Wegjan-Kuipers, *Control your speed,* Word Pipelines **3(3)**, 31 (2003).

[13] PPSA, *An Introduction to Pipeline Pigging*, 1st ed. (Pigging Products & Services Association, 1995).

[14] D. L. Atherton, *Stress-shadow magnetic inspection technique for far side anomalies in steel pipe,* NDT International **16(3)**, 145.

[15] J. Sullivan, *An anlysis of the motion of pigs through natural gas pipelines*, Master's thesis, Rice University, Unites States of Americia (1981).

[16] A. O. Nieckele, A. M. B. Braga, and L. F. A. Azevedo, *Transient pig motion through gas and liquid pipelines,* Journal of Energy Resources Technology **123(4)**, 260 (2001).

[17] D. Matko, G. Gerger, and W. Gregoritza, *Pipelines simulation techniques,* Mathematics and Computers in Simulations **52(3)**, 211 (2000).

[18] A. Singh and R. A. W. M. Henkes, *Cfd modelling of the flow around a by-pass pig,* 8th North American Conference on Multiphase Technology , 229 (2012).

[19] J. E. A. Korban, *CFD modelling of bypass pigs*, Master's thesis, Delft University of Technology, the Netherlands (2014).

[20] A. Erdal and H. I. Anderson, *Numerical aspects of flow computation through orifices,* Flow Measurement and Instrumentation **8(1)**, 27 (1997).

[21] J. Tu, G. H. Yoeh, and C. Liu, *Computational Fluid Dynamics: A Practical Approach*, 2nd ed. (Butterworth-Heinemann, 2012).

[22] I. E. Idelchik, *Handbook of Hydraulic Resistance*, 2nd ed. (Hemisphere Publishing Corporation, 1987).

[23] P. K. Kundu, L. M. Cohen, and D. R. Dowling, *Fluid mechanics*, 5th ed. (Academic Press, 2012).

[24] *Fluent Theory Guide,* Ansys Inc., 14th ed.

[25] T. hsing Shih, W. W.Liou, A. Shabbir, Z. Yang, and J. Zhu, *A new $k-\epsilon$ eddy viscousity model for high reynolds number turbulence flows,* Computers Fluids **24**, 227 (1995).

[26] P. L. Davis, A. T. Rinehimer, and M. Uddin, *A comparison of rans-based turbulence modeling for flow over a wall-mounted square cylinder,* 20th Annual Conference of the CFD Society of Canada (2012).

[27] A. Bakker, *Meshing - Applied Computational Fluid Dynamics,* Tech. Rep.

[28] S. B. Pope, *Turbulent Flows*, 1st ed. (Cambridge University Press, 2000) an optional note.

[29] K. Kohda, Y. Suzukawa, and H. Furukawa, *New method for analyzing transient flow after pigging scores well,* Oil Gas Journal **9**, 40 (1988).

[30] *Efficient simulation of one-dimensional two-phase flow with a new high-order Discontinuous Galerkin method* (2015).